LEVEL SPECTROSCOPY OF A QUANTUM DOT

A DISSERTATION
SUBMITTED TO THE DEPARTMENT OF APPLIED PHYSICS
AND THE COMMITTEE ON GRADUATE STUDIES
OF STANFORD UNIVERSITY
IN PARTIAL FULFILLMENT OF THE REQUIREMENTS
FOR THE DEGREE OF
DOCTOR OF PHILOSOPHY

By
Duncan R. Stewart
March 1999

I certify that I have read this dissertation and that in my opinion it is fully adequate, in scope and quality, as a dissertation for the degree of Doctor of Philosophy.

James S. Harris, Jr.
(Principal Adviser)

I certify that I have read this dissertation and that in my opinion it is fully adequate, in scope and quality, as a dissertation for the degree of Doctor of Philosophy.

Charles M. Marcus

I certify that I have read this dissertation and that in my opinion it is fully adequate, in scope and quality, as a dissertation for the degree of Doctor of Philosophy.

Yoshihisa Yamamoto

Approved for the University Committee on Graduate Studies:

Abstract

We present an experimental investigation of the ground and excited state spectra of disordered, multi-electron GaAs/AlGaAs semiconductor quantum dots, for successive numbers of electron occupancy $N, N+1 \ldots N+8$. Electron tunneling spectroscopy is used to probe the quantum dot ground and excited states. Linear and nonlinear magnetoconductance measurements allow identification of individual quantum levels. Successive ground states show matched anticrossings where wavefunction characteristics are exchanged between adjacent levels. Successive excitation spectra are found to be very strongly correlated. A further direct correlation is observed between the m^{th} excited state of the N-electron system and the ground state of the $(N+m)$-electron system for m up to 4. These results are surprisingly consistent with a non-interacting picture in which a fixed spectrum of energy levels is successively filled. The most notable departures from this single-particle model are the absence of spin degeneracy in the measured spectra and the broadened linewidths of higher energy excited states. Further departures are also seen in deviations from exact ground/excited correlations, particularly for $m > 4$. The basic features of these results agree with theory describing different energy regimes of quasiparticle decay and associated single-particle character for excitations of a finite Fermionic system. Other data remain unexplained, and suggest new directions for both experiment and theory in understanding the dependence of these strong correlations on the disorder and size of these mesoscopic quantum dot systems.

Acknowledgements

I would like to express my sincere appreciation to Dr. Y. Yamamoto for serving on my dissertation reading committee; Dr. C. Marcus for providing the world class laboratory in which this work was done, for offering excellent theoretical support to the work both personally and through collaboration with others, and for teaching and maintaining only the highest scientific standards in all the laboratory efforts; and Dr. J. S. Harris for showing absolutely unshakeable confidence and support during my six years of work on this thesis.

I would also like to thank all colleagues in both the Marcus and Harris groups for creating an environment that was both very warm personally and very stimulating scientifically.

I am indebted to the staff of the Physics Department, the Applied Physics Department, Ginzton Laboratory and the Center for Integrated Systems for their substantial contributions to both the scientific investigation presented here and my personal well-being at Stanford.

Most importantly, I am deeply grateful for the friendship, care and love that has been offered unceasingly by good friends and family.

Contents

List of Tables

List of Figures

Chapter 1

Statement of the Problem

1.1 Artificial Atoms

Quantum dots (QDs) are small electrically conducting regions, typically 1um or less in size, containing from one to a few thousand electrons [Kouwenhoven97;Meirav95]. Because of the small volume the allowed electron energies within the dot are quantized, forming a discrete spectrum of quantum states not unlike the energy levels of an atom. Indeed the simplest model of a quantum dot is perhaps a large and controllable "artificial atom". However in contrast to the ordered shell structure of atomic spectra – a consequence of the spherically symmetric potential that binds the electrons – the generic energy spectrum of a QD (lacking any special symmetry) shows no shell structure but instead has universal statistical properties associated with the underlying universality of quantum chaos [Altshuler95;Beenakker97].

Disordered or irregularly shaped QDs are examples of so-called mesoscopic systems – small electronic structures intermediate in size between atoms and macroscopic (classical) objects that have universal spectral and transport properties independent of material, shape or disorder. In the past few years, a remarkable set of connections between mesoscopic systems, complex quantum systems such as heavy nuclei (where the statistical approach to spectra was first developed), quantum systems whose classical analogs are chaotic and random matrix theory has emerged, providing deep theoretical insight into the generic properties of quantum systems [Altshuler95; Beenakker97; Marcus97; Gutzwiller90]. These connections are based principally on noninteracting, single-particle spectral properties; only recently has attention been focused on mesoscopic systems in which interactions between

particles and quantum interference play equally important roles. In this context it is therefore essential to better understand the strength of the electron-electron interactions and their impact on the generic spectral properties of multi-electron QDs. An important goal is to understand the limitations of the single-particle based theories which have to date provided the basis for understanding most spectral features of quantum dots.

The electron-electron interactions also possess strong intrinsic interest in this mesoscopic system. The many-body theory of electrons in solids assumes an infinite electron gas system with a continuous energy spectrum and a well defined Fermi surface [Pines89;Mahan90]. Interactions are treated with the goal of determining averaged physical properties such as the momentum distribution, paramagnetic susceptibility or mean free path. However both the crystalline solid characteristics and the electron interactions may affect any measured physical property. The influence of each in a measured property is often difficult to determine, and interaction theory predictions are thus difficult to confirm. The many-body theory of atoms, in contrast, is anchored within a discrete spectrum framework; interactions affect individual state energies and wavefunctions of the 1/r Coulomb potential. Interaction theory predictions can be tested more easily but do not necessarily extend to the solid-state systems. The mesoscopic system of a QD lies between these two extremes. It is a small electron gas, existing within the periodic crystal potential yet possessing a discrete and experimentally resolvable spectrum. Level spectroscopy of the QD offers a new and powerful access to the electron-electron interactions in a solid-state system.

1.2 Single-particle or many-body spectrum ?

The spectrum of quantum levels for a single particle in any given potential is an exactly solvable problem. Schrodinger's equation describes the behavior of the particle within the confining system potential walls, and yields a set of allowed eigenenergies and eigenfunctions. For a particle with a deBroglie wavelength comparable to the size of the system, this set of energies forms a discrete ladder with well separated rungs. The isolated single particle can exist only at one of the energies on this ladder, physically distributed in the corresponding spatial wavefunction. Figure 1.1 illustrates this discrete ladder of states for the case of a 1/r hydrogen atom potential and for the artificial atom infinite 1D square well. In each case, a single-electron placed in the potential will occupy one of the discrete energy levels.

The addition of a second electron to the confining potential complicates the problem

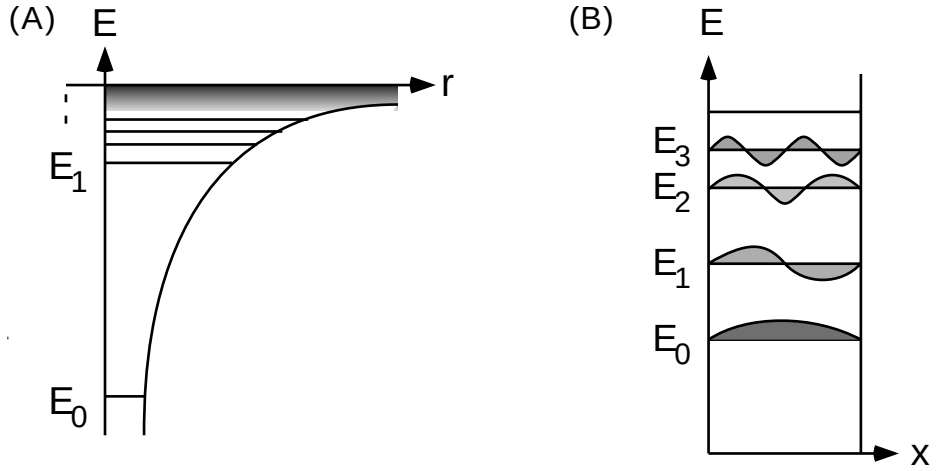

Figure 1.1: (A) The energy spectrum of the 1/r hydrogen atom Coulomb potential (B) The energy spectrum (eigenvalues and eigenfunctions) of a 1D particle in a box.

considerably, for the two-particle Schrodinger equation is not exactly solvable. Many approximation methods have been developed to treat the effect of interaction between the two particles, but when compared to experiment they have had variable success and often remained dependent on the precise problem formulation. The spectrum of allowed energies for the two-electron system is thus not generally known, and in principle may be completely different from the single-electron spectrum.

The observed spectrum of helium is indeed very different from that of hydrogen. For larger atoms, the hydrogenic alkali elements Li,Na,K,Rb and Cs are an interesting example of the possible effect of electron interactions. Each atom has a single weakly-bound valence electron outside a set of filled electron shells. The spectrum of transitions available to this electron might be assumed identical to the single-electron hydrogen spectrum. At very high energies when the valence electron is far from the atom in higher d or f orbitals this description is essentially correct, however at lower excitations when the valence electron wavefunction penetrates the existing closed shells to interact with those shell electrons, the levels are strongly perturbed. All s and p orbitals of the valence electron are at a lower energy than expected from the hydrogen solution; since they penetrate the closed shells the valence electron feels less screening of the nuclear charge, or equivalently is bound more strongly to the core by the Coulomb repulsion of those shell electrons at larger radius.

Returning to the two electron case, if the interaction between the electrons is ignored

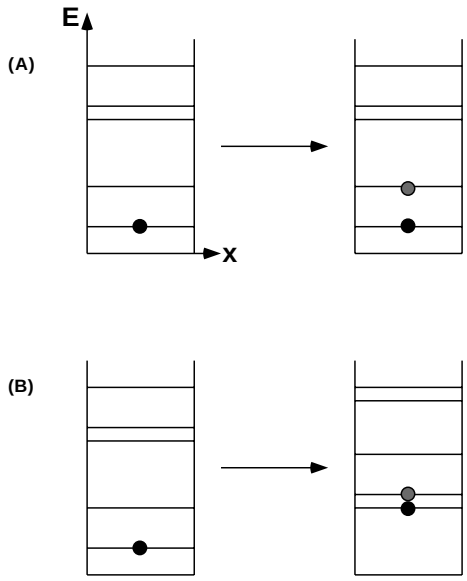

Figure 1.2: (A) The addition of a particle to the system in the non-interacting, single-particle approximation; the spectrum is unchanged (B) The addition of a particle to the system in the strongly-interacting case "scrambles" the existing energy level spectrum

they can simply be treated as two independent electrons that occupy the states of the single-electron energy ladder. Adherance to the Pauli exclusion principle then yields a single-particle picture in which a fixed spectrum of quantum levels is successively filled as electrons are added one by one to the system. Figure 1.2 is a cartoon depicting these dichotic behaviors: in the single-particle model addition of an electron leaves the spectrum unchanged, whereas in the strong interaction many-body model the addition of an electron completely "scrambles" the level spectrum.

This change in the quantum level spectrum upon addition of a particle is the basic question we attempt to address. In reality the scale is not dichotomous, but continuous from weak interactions and a slightly changed spectrum to strong interactions and a completely scrambled spectrum. The strength and impact of the interactions will be assessed by identifying which spectral properties change and how much they change upon addition of an electron to the system. Theoretical descriptions of both metals and large atoms show the Coulomb interaction energy between electrons is comparable to the electron kinetic energy (metals) or the nucleus binding energy (atoms), indicating that many properties of these systems may well be affected by the electron-electron interactions. In atomic spectra, the

many-body repulsion between electrons is essential in calculating any level spacings beyond the one electron hydrogen atom. The qualitative shell structure however, is consistent with the hydrogen solution even for large atoms. In metals, many transport properties can be well explained by a single particle moving in the periodic lattice potential yet other properties including magnetism require particle interactions. Our quantum dot is both a small piece of metal and a large atom, and we expect many properties of it's energy spectrum to also be determined by electron interactions.

1.3 This Work

This work is an experimental investigation into the quantum level spectra of mesoscopic quantum dots. We attempt to identify the impact of electron-electron interactions on the QD spectral properties by comparing the N electron QD spectrum to the $N+1$ electron spectrum. Using this comparison method we characterize those spectral properties that are well described by a single-particle theory and those that require more complex interacting many-body theories, and we attempt to understand the boundary between these behaviors.

In Chapter Two we outline some of the previous theoretical and experimental work relevant to our problem. Chapter Three is a discussion of the different energy scales significant to the quantum dot and their impact on the tunneling spectroscopy that we use to measure the QD energy spectrum. In Chapter Four the raw materials of the experiment are detailed: the device fabrication, the experimental setup, experimental methods and the basic quantum dot characteristics. The real data begins with spectroscopic measurements of the QD ground states reported in Chapter Five. Chapter Six is the heart of the investigation, containing all measurements of the QD excited state spectra and analysis of the remarkable correlations between them. Chapter Seven brings together the ground and excited state measurements in a powerful correlation analysis illustrating the basic findings of the investigation. In Chapter Eight we attempt to reconcile the single-particle /emphand many-body spectral properties observed by appealing to recent theoretical work that appears to unite the traditionally different solid-state and atomic approaches to the many-body problem. We hope you enjoy the tour!

Chapter 2

Previous Theory and Experiment

2.1 Introduction

Fermionic systems have long been studied theoretically and experimentally in both atomic physics and solid-state physics. The investigation of particle interactions remains perhaps the most difficult issue to treat theoretically, and has consequently provided real surprises experimentally including superfluidity and the quantum hall effect. In an electronic system one of the most significant parameters characterizing the particle interactions is the ratio of interaction (potential) energy to kinetic particle energy. A high ratio means a system dominated by interactions; a low ratio indicates that interactions may be only a perturbation to the kinetic particle motion. For the quantum electron liquid this ratio is the Coulomb repulsion energy at the average inter-electron spacing divided by the free electron Fermi energy:

$$\frac{E_P}{E_K} = \frac{e^2 m r^2}{r\hbar^2} = \frac{r}{a_{Bohr}} = r_s \tag{2.1}$$

where r_s is exactly the average inter-electron spacing in units of the Bohr radius aBohr. A high density electron gas has an excess of kinetic energy and $r_s \ll 1$. In this limit the interaction is a perturbation to the kinetic motion, and the microscopic random phase approximation (RPA) theory describes the system properties very well. A low density electron system has low kinetic energy and $r_s \gg 1$, and in this limit the electrons tend towards a solid lattice or 'Wigner crystal" in an effort to minimize the total Coulomb interaction energy[Andrei97]. This solid phase is also well described theoretically. At intermediate densities, $1 < r_s < 10$, the particle kinetic and potential energies are comparable and neither

can be treated as a perturbation to the other. This is unfortunately the regime of conduction electrons in most metals $1 < r_s < 6$, as well as the two-dimensional semiconductor electron gas of our own experiment where we again have $r_s \approx 1$! It is this equal footing of the kinetic and potential energies that makes this the most difficult regime to treat theoretically. Experimental studies of electron interactions in this regime are an opportunity to offer new evidence guiding this interesting and difficult theoretical development.

In this chapter we outline the general single-particle and many-body theoretical approaches to discrete electronic systems. We then describe the relevant previous theoretical and experimental work directly related to the mesoscopic quantum dot system.

2.2 Theoretical background

2.2.1 Single-particle theory

The single-particle Schrodinger equation of quantum mechanics has unlocked many secrets of the atomic and condensed matter worlds. The time-independent non-relativistic Schrodinger equation yields the single-particle eigenvalues and eigenfunctions of the artifical atom potential defining the quantum dot:

$$\left[\frac{-\hbar^2}{2m}\nabla^2 + V(r)\right]\psi = E\psi \tag{2.2}$$

where the first term yields the kinetic energy of the particle, the second term is the potential energy of the confinement potential, $\psi(r)$ is the eigenfunction and E is the corresponding eigenvalue. This equation can be solved exactly for any potential $V(r)$ to find the set of bounded one-particle energies and spatial wavefunctions. The relatively shallow QD potentials will not require any relativistic corrections.

The simplicity of the solution enables powerful calculations of the single-particle spectral properties. One property essential to our study will be the continuous evolution of both wavefunctions and eigenenergies as a function of a QD environment parameter. The confinement potential shape and the magnetic field B both perturb the QD spectrum parametrically. Both parametric changes are entirely reversible. A uniform magnetic field

oriented along the z axis of amplitude B_z is added to the Schrodinger equation as:

$$\left[\frac{-\hbar^2}{2m}\nabla^2 + V(r) + \frac{\mu_B B_z}{\hbar}(L_z + 2S_z)\right]\psi = E\psi \tag{2.3}$$

where L_z is the z component of the orbital angular momentum, S_z is the z component of the intrinsic electron spin moment and μ_B is the Bohr magneton. The magnetic field perturbation to the eigenvalues and eigenfunctions is symmetric about $B = 0$ for positive and negative field vectors. Individual levels evolve smoothly as a function of B, some ascending in energy and some descending in energy. For a symmetric confining potential this yields a large number of crossings between states with different velocities dE/dB – at each crossing the states are degenerate in energy, a direct consequence of the symmetric potential and the resulting symmetric spatial wavefunctions. A shell structure similar to that of atoms exists. In a disordered or irregularly shaped quantum dot the spectrum of energy levels appears random, due to the underlying quantum chaotic nature. No shell structure exists to impose special energy degeneracies, and the wavefunctions themselves lack any spatial symmetry, instead extending over the entire confinement volume in a random pattern of nodes and antinodes (Figure 2.1A). As a result, the spectrum response to a parametric magnetic field perturbation also appears random. Figure 2.1B displays eigenvalues of a calculated 2D cavity spectrum parametrically perturbed [Simmel95]; the "spaghetti" forms as successive wavefunctions respond differently to the perturbation and subsequently cross or anti-cross with the neighboring wavefunctions. The unique spectral response to a given parametric perturbation thus provides a characterization of that particular spectrum. We will use this method to identify individual spectral features and enable most of our spectral analysis.

A different approach pursued very fruitfully has been the statistical characterization of generic spectral properties. The average values and statistical distributions of many properties are well defined within the single-particle framework, and can be calculated using a set of theoretical tools. Random matrix theory (RMT) [Mehta91] in particular has yielded many valuable statistical results including the distributions of tunneling amplitudes [Jalabert92], level spacings [Mehta91;Vallejos98] and avoided crossing measures [Takami92;Wilkinson89;Zakrzewski91] as well as parametric correlation functions for the tunneling amplitudes [Alhassid96;Bruus95], spacings and level velocities and curvatures [Simmel95]. In each case the generic quantum properties are different at zero and finite

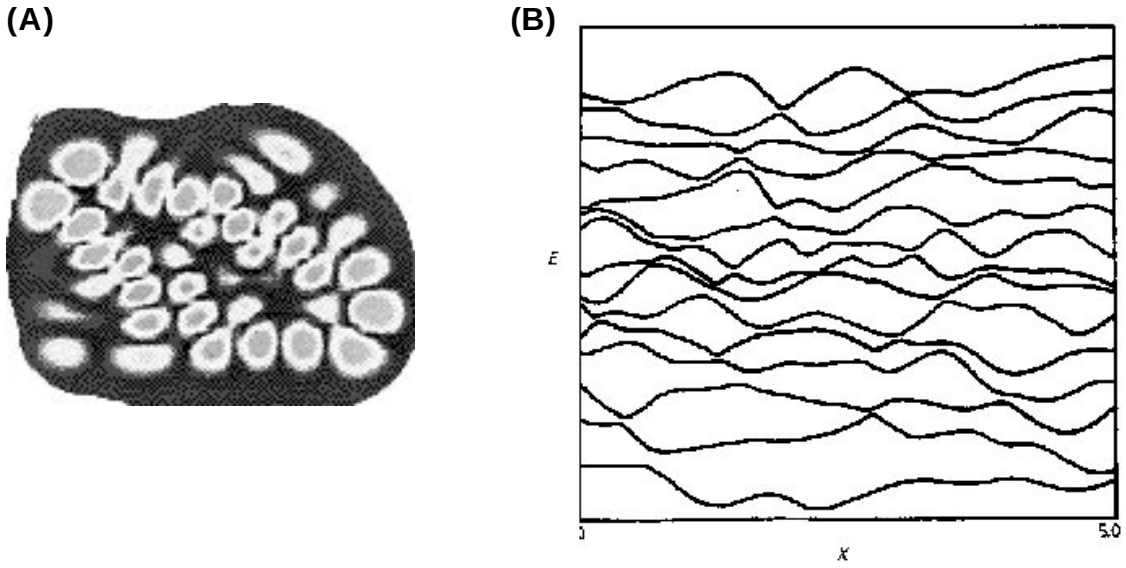

Figure 2.1: (A) Calculated wavefunction probability density for a non-symmetric confining potential [from Stopa97] (B) Calculated energy spectrum of a chaotic system evolving parametrically with perturbation x [from Wilkinson89].

magnetic field, and RMT provides both results. Many of these results have been tested by experiment, as discussed in Section 2.3.1.

2.2.2 Exact many-body theory

The many-body Schrodinger equation is generally intractable, even for only two particles. In the case of interacting electrons, a $1/r$ Coulomb term must be added to the potential energy that expresses the mutual Coulomb repulsion between all pairs of electrons. The Schrodinger equation for N electrons is now written as

$$\left[\frac{-\hbar^2}{2m}\sum_i \nabla_i^2 + \sum_i V(r_i) + \frac{1}{2}\sum_{i,j}\frac{e^2}{|r_i - r_j|}\right]\Psi(r_1, r_2 \ldots r_N) = E\Psi(r_1, r_2 \ldots r_N) \qquad (2.4)$$

where the 1/r Coulomb term is a function of *all N particle coordinates*. This linking of the particle coordinates makes the equation inseparable into N individual single-particle equations of the form Eqn 2.2 above. The single equation with N coordinates cannot be solved, and various approximation methods must generally be used to move beyond the

single-particle solutions.

One numerical method that can approach an exact solution for very small particle numbers and low energy states is the so-called exact diagonalization method [Johnson95]. A set of the m lowest single-particle eigenstates is selected and *assumed* to be a sufficient basis for the Hilbert space of many-body eigenstates. A complete basis would require inclusion of an infinite number of single-particle states; the limited set is of course not exact, but if the basis set chosen extends much higher in energy than any occupied many-body states it can be an excellent approximation. The exact Hamiltonian (Eqn 2.4) is then diagonalized numerically in the restricted configuration space of all combinations of the N particles in the m basis orbitals. The intensive numerical calculation limits this method to low electron numbers $N < 10$, however it has the advantage of including all interaction effects, including the correlations omitted by Hartree-Fock theory (Section 2.2.3).

Using the exact diagonalization method for a harmonic confining potential and $N \leq 3$, the many-body eigenvalue spectrum shows dramatic change upon the addition of a particle. Figure 2.2 shows these calculated spectra [Pfannkuche95; Ulloa94]. The $N = 1$ spectrum is the periodic energy ladder expected in a harmonic potential. The $N = 2$ spectrum shows a significant increase in excited state level density compared to the $N = 1$ ladder, although groupings of excited levels appear with the same periodicity as the $N = 1$ harmonic spacing. In the $N = 3$ spectrum, even this resemblance has disappeared due to the rapid increase in level density at higher energies. However, tunneling spectroscopy may not access all levels of this dense spectrum. Pfannkuche and Ulloa argue that center-of-mass excitation modes spaced with the original $N = 1$ harmonic periodicity may dominate the tunneling density-of-states.

Exact diagonalization has also been applied to the magnetic field dependence of the low energy harmonic potential spectrum. Ground states from $N = 1$ to N=8 and the first and second excited states for $N = 1$ to $N = 5$ have been calculated using the basis set of the lowest fifteen single-particle states [Eto97a; Eto97b]. In the interaction regime chosen where the 1/r term is comparable to the single-particle level spacing, the numerical results detail significant deviations from single-particle behavior in the magnetic field spectral dependence. The explicitly correlated nature of the Landau level ground states has also been studied [Palacios94]. These low electron number exact calculations have shown good agreement with ground state experimental measurements in circularly symmetric "vertical" QDs [Tarucha96; Ashoori94]. The few experimental excited state measurements in these systems

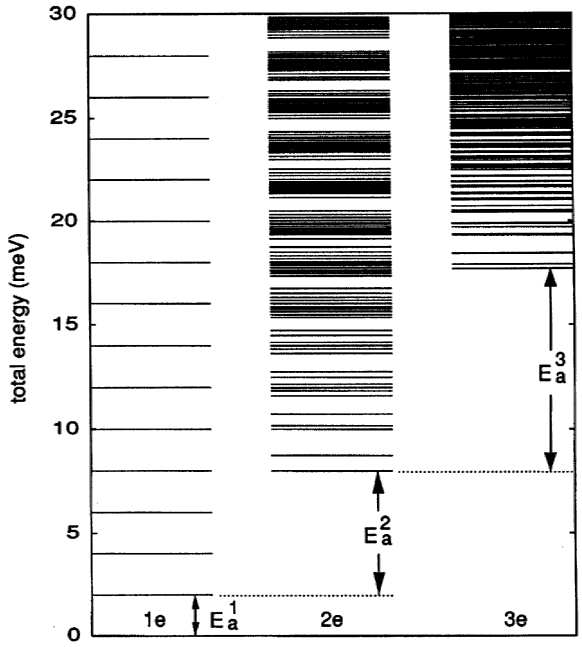

Figure 2.2: The calculated quantum dot spectrum for N=1,2,3 electrons in a symmetric harmonic oscillator potential well [from Pfannkuche95].

also show agreement [Kouwenhoven97].

In other work exact diagonalization has elucidated the role of spin and spatial selection rules in the tunneling spectroscopic transitions between the N and $N+1$ many-body eigenstates. Again, for few ($N \leq 6$) electrons, a tunneling Hamiltonian and rate equation approach have been added to calculate tunneling current through the QD levels, for transport through both ground and excited states [Pfaff94; Jauregui96; Weinmann95]. The selection rules were shown to generally reduce the number of many-body states contributing to the tunneling current, and in particular when mapped onto the experimental Coulomb diamond picture of Section 3.4.3 yielded both complex level interactions and negative differential conductance. Both these experimentally observed features are discussed further in Section 3.4.3 and Section 6.5 .

Finally, a different exact solution is possible in the classical regime of discrete electron charges. An electron gas will condense into a solid Wigner crystal when the Coulomb repulsion energy becomes much greater than the particle kinetic energy, given at this low classical

density regime by the temperature $E_k = 3/2k_BT$, where k_B is Boltzmann's constant. For a 2D electron film this transition occurs near $E_{pot}/E_{kin} = r_s = 130$ [Grimes79;Andrei97]. Packing the electron charges into a restricted geometry causes distortion of the lowest energy triangular lattice, and calculations can yield the cost of a particle addition and the energy spectrum for each case N and $N+1$ [Koulakov98; Koulakov97; Sivan96]. The application of these results to the QD case is controversial since in the 2D electron gas of most QD experiments the ratio of potential to kinetic energy is $r_s \sim 1$ and electron localization and Wigner crystallization appear unlikely.

2.2.3 Many-body approximations

Approximation methods for quantum many-body problems form a very large area of theoretical physics. Here we only outline the problem before citing several approaches that have been applied to the quantum dot system.

The many-electron Schrodinger equation is not tractable because of the inseparable particle coordinates found in the 1/r Coulomb term. All approximation methods rely on treatment of this term in a manner that allows separation into N single-particle equations that can be individually, or at least self-consistently, solved. The N-particle wavefunction is then described as a product of N independent one-particle wavefunctions. For very small numbers of electrons in an atomic problem, the 1/r term can be eliminated and then reintroduced using standard perturbation theory techniques and variational calculations [Bransden83]. For larger particle numbers or any solid-state problem, the 1/r term must be replaced with a mean-field potential $V(r)$ – the average potential seen by a single-electron due to repulsion by all the other electrons. This newly tractable many-body equation is written as:

$$\left[\frac{-\hbar^2}{2m}\sum_i \nabla_i^2 + \sum_i V(r_i) + \sum_i v(r_i)\right]\prod_i \psi(r_i) = E\prod_i \psi(r_i) \tag{2.5}$$

Many different methods and approximations can be used to formulate the mean field potential, $V(r)$, including the Thomas-Fermi approximation, the self-consistent Hartree-Fock (HF) approximation, the random phase approximation (RPA) and the density functional (DF) method. Extensions and modifications to these basic approaches form an enormous literature, but here we focus on the Hartree-Fock and density functional theories as applied to QD calculations.

Hartree-Fock approximates the N-electron wavefunction as a Slater determinant, the antisymmetric product of individual electron spin-orbitals. The optimum Slater determinant is obtained by a variational calculation to minimize the total energy and thereby determine the individual orbitals. The interaction term then appears in two components, the direct interaction V^d and the exchange interaction V^{ex}. Explicitly,

$$\left[-\frac{1}{2}{\nabla_{r_i}}^2 + V(r) + \sum_\mu V_\mu^d(r_i) - \sum_\mu V_\mu^{ex}(q_i)\right] u_\lambda(q_i) = E_\lambda u_\lambda(q_i) \tag{2.6}$$

$$V_\mu^d(r_i) = \int u_\mu^*(r_j)\frac{1}{r_{ij}}u_\mu(r_j)dr_j \tag{2.7}$$

$$V_\mu^{ex}(q_i)u_\lambda(q_i) = \left[\int u_\mu^*(q_j)\frac{1}{r_{ij}}u_\lambda(q_j)dq_j\right] u_\mu(q_i) \tag{2.8}$$

where $u_\lambda(q_j)$ is a one-electron spin orbital, containing the spatial and spin dependence of a single-electron eigenfunction. The direct Coulomb term or Hartree term is simply the repulsion between each electron pair integrated over their average spatial distributions. The exchange or Fock term results from the antisymmetrization requirement, and accounts for the Pauli exclusion induced tendancy of spin aligned electrons to avoid each other spatially. This spatial avoidance translates into a lowering of the system energy, hence the exchange term is negative. The many-body wavefunction is constructed as a Slater determinant of the spin orbitals $u_\lambda(q_j)$:

$$\Psi(q_1, q_2 \ldots q_N) = \frac{1}{\sqrt{N!}}\begin{bmatrix} u_\alpha(q_1) & u_\beta(q_1) & \ldots & u_\nu(q_1) \\ u_\alpha(q_2) & u_\beta(q_2) & \ldots & u_\nu(q_2) \\ \vdots & & & \\ u_\alpha(q_N) & u_\beta(q_N) & \ldots & u_\nu(q_N) \end{bmatrix} \tag{2.9}$$

Solution of the Hartree-Fock equations proceeds by iteration, starting from an initial estimate of the orbitals $u_\lambda(q_j)$. An approximate HF potential $V_{HF}(r) = \sum_\mu V_\mu^d(r_i) - \sum_\mu V_\mu^{ex}(q_i)$ can be calculated from the initial orbitals. This $V_{HF}(r)$ can then be used to produce a more accurate set of orbitals, which allow recalculation of the HF potential. Iteration is continued to the desired accuracy. The difference between the self-consistent HF solution and the exact solution has been labeled the correlation energy E^{corr}. This reflects the fact that the largest error in the HF method arises from the ignored correlated motion of the electrons,

particularly those spin anti-aligned that are not treated by the exchange energy correction.

Hartree and Hartree-Fock methods have been applied to the calculation of QD spectra. Pure Hartree calculations neglect the antisymmetrization requirement and consequently the exchange term (Eqn 2.8) disappears. These calculations are less intensive numerically and have been combined self-consistently with the Poisson equation to determine realistic electrostatic QD confinement potentials [Kumar90; Stopa93]. At high magnetic fields, Hartree results have described the transfer of charge between different Landau bands within a 35 electron QD and the resulting ground state energy evolution with field [Oaknin94]. Hartree-Fock has also been used in this high field regime [Palacios94], yielding good qualitative agreement with experiment [Ashoori94, McEuen91]. Statistical properties of the QD level spacings have been extracted from HF results to investigate the effect of e-e interactions on the level spacing distribution [Cohen98; Tamura97]. Although most of these HF results focus on ground state properties, nonlinear transport through excited states has also been investigated. Agam et al. employ HF to consider non-equilibrium effects on the measured QD excitation spectrum [Agam97], and Tanaka et al use HF and a master equation approach to calculate I-V characteristics of small $N < 4$ quantum dots [Tanaka96]. Hartree-Fock with a random phase approximation of the screened potential has also been applied to determine the fluctuations of ground state energy spacings [Blanter97].

Density functional theory is a second approach to solving the many-body Eqn 2.4, utilizing the basic theorem that for an interacting many-body system in an external potential $V(r)$, the ground state density $n(r)$ is uniquely related to the external potential $V(r)$ [Hohenberg64; Joubert98]. Given the external potential $V(r)$, all properties of the system including energy can then be shown to be functionals of the ground state density $n(r)$. In particular, if the form of the energy functional $F[n(r)]$ is known then minimization of the ground state energy with respect to $n(r)$ yields the exact ground state energy and density. The Hohenberg-Kohn variational principle yields the Kohn-Sham self-consistent equations [Kohn65]. Approximation is involved in specifying how the exchange and correlation energies E^{xc} enter the functional $F[n(r)]$. The local density approximation (LDA) is perhaps the simplest specification of E^{xc} and is based on the well characterized exchange-correlation energy of electrons in a uniform electron gas. This approximation is more precise in high density metallic regimes than the low density 2D electron gas of our QDs, yet has been applied successfully to a wide range of atomic, molecular and solid-state systems. The potential inclusion of correlation effects is an attractive feature of DF theory not offered in

HF.

In quantum dot electronic structure calculations, both density functional theory and spin-density functional theory have been used to calculate QD ground states for $N = 50-150$ electrons. The statistics of successive ground state level spacings have been extracted and for a disordered QD potential appear to agree with RMT distributions [Stopa96]. Remnants of periodic classical orbits, or "scars" in the quantum wavefunctions modified this spacing distribution by producing anomalously large ground state gaps. Particularly relevant to our own experimental results, spin-density functional calculations have predicted that the QD is usually spin polarized with several aligned and uncompensated electron spins [Hirose98; Stopa97]. This spin splitting of quantum levels and resultant QD spin polarization results from the electron interaction terms.

The accuracy of these approximate many-body methods can be difficult to evaluate. In the low N regime however, the HF solutions can be directly compared to exact diagonalization results. For the case of $N = 2$ in a harmonic QD potential, Pfannkuche et al report that the HF and exact ground state energies agree closely for the spin triplet state, and are both $\sim 25\%$ lower in energy than the Hartree result [Pfannkuche93a; Pfannkuche93b]. For the spin singlet ground state however, the exact result is another $\sim 10\%$ lower than the HF energy. This is explicitly shown to be due to the correlation effect; the exact and HF pair-correlation functions for the triplet state are very similar but for the singlet state the HF pair correlation shows the two electrons with much greater spatial overlap than in the exact pair correlation. The HF approximation neglects this correlated electron motion, also shown to be important specifying wavefunctions and tunneling amplitudes in the high magnetic field Landau level regime [Palacios94]. Tanaka et al compare HF and exact calculations of transport through excited states and argue that correlations are less significant in this case [Tanaka96]. Although density functional theory using the LDA is expected to be inaccurate for low electron density and number, spin density functional calculations have reproduced exact results even in the limit of $N \sim 5$ [Steffens97]. General accuracy trends have also been studied using an analytically solvable harmonic coulomb interaction, where the Hartree and Hartree-Fock ground state energies are shown to decrease in accuracy for increasing electron number N, decreasing magnetic field strength B and stronger electron-electron interactions. Experimentally we will work at relatively large $N \sim 50 - 100$, low $B = 0 - 1T$ and intermediate interactions $r_s \approx 1$, suggesting that the Hartree-Fock method may yield poor predictions of the QD behavior.

A very different many-body treatment is found in the Landau theory of Fermi liquids [Pines89]. This macroscopic theory of interacting quantum particles successfully describes many system properties by analyzing the elementary excitations of the many-body system. At low temperature only a few excitations are present, they are long lived and interact only weakly with one another. The system response can then be understood by the behavior of these elementary excitations, "quasiparticles" in the Landu theory language. The conduction electrons in metals are an interacting Fermi liquid and are indeed well described by the Landau theory in most cases. However this macroscopic theory does not explain microscopic behavior nor is it applicable to a finite system. Nevertheless, the quasiparticle concept has been extended to the system of a quantum dot recently, and we follow this valuable idea in Section 8.

Finally we return to our initial statement of the problem. In Section 1 this was distilled in simplest form into the question: How does the spectrum of a large, disordered quantum dot change upon addition of a single-electron ? We have indicated that even numerically an exact solution of the Schrodinger equation is not possible for $N > 10$. The Hartree-Fock approximation method is of varying accuracy when compared to low N exact calculations and it is suggested that it becomes less accurate at high N. The validity of the local density approximation required in density functional calculations is similarly unverifiable. Within the mean field of Hartree-Fock and DF theory through the LDA the level spectrum of a large QD will change only slowly as electrons are added. One electron added to fifty or a hundred will weakly perturb the average electron potential. However, this picture discounts the effect of correlations in the electron motion. A strongly correlated wavefunction, as discussed in the exact solutions of small N dots, may be strongly perturbed by the addition of a single electron. Our question therefore focuses on determining the strength and impact of the electron interactions and particularly correlations on the electronic spectrum.

2.3 Experimental background

2.3.1 Ground state spectra

A growing body of experimental literature describes the tunneling spectroscopy of quantum dot ground states. A major result of the first investigations was the quantitative understanding of the basic coulomb blockade periodicity through the constant interaction model [Kulik75]. This model describes the fixed classical charging cost associated with adding an

electron to a small isolated metal island. Refinement of this constant charging energy model allowed consideration of islands with a discrete quantum confinement spectrum, added as a fixed single particle spectrum [Beenakker91a]. These theories were successful in predicting CB peak periodicity [Meirav95], lineshapes [Foxman93a; Klein96] and magnetic field features [McEuen91].

The discrete single particle spectrum added to the constant interaction model allowed the theoretical framework of random matrix theory to predict statistical properties of the measured ground state spectrum, described above in Section 2.2.1 . Experimental testing and confirmation of the predicted CB peak height distributions [Chang96; Folk96] and parametric correlation functions [Patel97] followed. These experiments appeared to offer strong support for consideration of the QD ground states as rungs of a fixed single particle ladder.

However, further experiments showed distinct deviations from this single particle spectrum. At high magnetic fields the charging of Landau levels is well explained by a self-consistent model that explicitly predicts varying interaction strength between electrons residing in and tunneling into different Landau levels [McEuen92]. The measured ground state spectrum in small vertical QDs shows level crossings that are not predicted in a single particle model. At low electron numbers $N = 1 - 8$, an observed Hund's rule filling of orbitals could only be explained by consideration of the exchange interaction (see Section 2.2.3) [Tarucha96]. For $N = 2$ the exchange interaction causes a singlet-triplet transition at intermediate magnetic fields that is similarly not expected in a single particle spectrum yet has been observed in two different experiments [Ashoori94, Kouwenhoven97]. Random matrix theory also predicts distributions for the energy spacing between subsequent levels; unlike the experimentally confirmed peak height statistics, the peak spacing distributions measured are very different than predicted [Sivan96; Simmel97; Patel98a]. More detailed examination of the peak height correlations as a function of added electron number also show deviation from the RMT predictions [Patel98b]. This last investigation by Patel et al. is the only ground state spectroscopy that directly addresses the issue of changes to the spectrum caused by addition of electrons. The authors used temperature dependence of the deviation from the single particle RMT correlation function as evidence that the spectrum indeed appeared modified by the addition of several electrons to the quantum dot.

2.3.2 Excited state spectra

The extensive ground state experiments reported above were made with infinitesimal source-drain bias applied across the QD, usually at the lowest accessible mK temperatures. The excited QD states are available for tunneling only at finite bias (or higher temperature), and relatively few experiments have investigated this more complex regime of behavior. The first experiments to probe the excitation spectrum established the validity of the finite bias techniques, and proposed a simple extension of the single particle, constant interaction model to account for the results [Johnson92; van der Vaart93]. Excited states of the QD showed as conductance resonances with increasing source-drain bias, and were interpreted as alignment of higher single particle states with source or drain Fermi levels. This finite bias transport model (see also Section 3.4.4) counted available single particle states to determine the tunnel current into and out of the QD. A quantitative version of this model successfully described many of the finite bias features observed [Foxman93a; McEuen93]. Evidence supporting the single particle model also showed in the first detailed Coulomb diamond measurements characterizing the excitation resonances as a function of both source-drain voltage and plunger gate voltage (see also Section 3.4.3) [Weis93 ;Weis94a; Weis94b]. These experiments mapped out a spectrum that was unexpectedly sparse – single particle like instead of the dense spectrum of the interacting system predicted by exact QD calculations [Pfannkuche 95].

The first explicit signs of many-body interaction within a quantum dot excitation spectrum were detected in tunneling spectroscopy of aluminium nanoparticles, individual 10nm Al metal grains. Here the measured spectrum showed small clusters of resonances separated by larger inter-cluster energy spacings [Ralph95; Ralph96; Ralph97]. The inter-cluster spacing matched the expected single particle level spacing, but spacing between resonances inside of one cluster was much smaller. A model of non-equilibrium transport incorporating fluctuations in tunneling level energy due to many-body interactions appeared to match the experimental results [Agam97]. Tunneling spectroscopy through a vertical double quantum dot structure was also argued to demonstrate increasing resonance width at higher energies above E_F [Sivan94a]. These two experiments are the only reported investigations into the dependence of excited state width on energy above the Fermi level. In Section 6.6 we report direct measurements of excited state widths, and in Chapter 8 we describe some of the very active theoretical work in this area. Other vertical dot data has elegantly confirmed the role of the exchange interaction lowering the $N = 2$ first excited state until it crosses the

$N = 2$ ground state in the singlet-triplet transition described above [Kouwenhoven97].

The experimental investigation of the quantum dot spectra has thus concentrated on the ground state properties, and only recently has investigation been pursued into excited state behavior. The work described in this thesis is significant as the first spectroscopic investigation of the correlations between ground and excited states for successive electron numbers in the QD.

Chapter 3

Coulomb Blockade and Tunneling Spectra

3.1 Introduction

The energy spectrum of an isolated 0D system is determined by the interplay of two energy scales: the capacitive charging energy, Ec, due to the discrete and countable number of electrons in the system, and the quantum mechanical confinement energy, delta, due to spatial localization of the electrons within the system boundaries. The capacitive charging Coulomb blockade phenomenon strongly affects our measurements of the 0D energy spectrum, complicating what might have been the simple spectroscopy of sequential states in the quantum confinement energy ladder. However with the method of spectroscopy chosen, electron tunneling spectroscopy, the complicating effect of Coulomb blockade is *exactly what enables* our comparison of the N electron spectrum to the $N+1$ electron spectrum. Indeed it is the ratio of Coulomb charging energy to quantum confinement energy that determines how much of the energy spectrum we can access spectroscopically. This chapter attempts to provide an understanding of the capacitive and confinement energy scales, and in particular how they affect the measured tunneling spectrum of an isolated quantum dot.

3.2 Capacitive Charging Energy

The simplest physical description of the quantum dot is as a small isolated metal island. Experimentally we have three terminals near the island, a source and drain connected by

large resistors and a capacitively coupled gate (Figure 3.1A). Consider the isolated island as one electrode of this very small capacitor and the nearby gate as the second electrode. Classically the charge on a capacitor is a continuous function of the voltage across the capacitor $Q = CV$. This is a good approximation for very large numbers of electrons and holes on each electrode, or for open systems where fractional equivalent charge can be achieved by partial displacement of the discrete electrons, as in a metal. The linear $QvsV$ relation is however a poor description when the total charge consists of a countable number of discrete electrons in an isolated system. In this case, corresponding to our small isolated island, the number of electrons must be either N or $N + 1$, nothing in between. Figure 3.1B & C illustrate how the linear classical relation becomes a staircase when we look more closely and consider the discrete charge case.

The electron number is thus precisely determined for all voltages except at the vertical steps in the staircase – at each of these points the charge on the island can fluctuate by one, from N to $N + 1$ and back to N. These charge degeneracy points are equally spaced in the gate voltage, with a periodicity of $\Delta V_g = e/C$. In the island energy, this is $\Delta E_{island} = E_C = e^2/C$ where ΔE_{island} is given the name "charging energy" E_C. For the isolated island the mechanism of charge fluctuation is electron tunneling onto and off of the island from the nearby source or drain terminals. If an infinitesimal bias is applied between the source and drain, current will flow only when tunneling is allowed at the degeneracy points. The transmitted current will then form a set of evenly spaced peaks at the periodic degeneracy points in gate voltage (Figure 3.1D). The regime where suppression of current occurs between the peaks is known as Coulomb blockade.

In reality the island is connected capacitively to other parts of the environment in addition to the gate. Figure 3.2 shows an equivalent circuit with the quantum dot island capacitively coupled to the gate and the source and drain. In this case the charging energy $E_C = e^2/C_\Sigma$, where $C_\Sigma = C_g + C_{sd} + C_{dd}$. The period of Coulomb blockade current peaks will be:

$$\Delta V_g = \frac{e}{C_g} = \frac{1}{\alpha}\frac{E_C}{e} \tag{3.1}$$

$$\alpha = \frac{C_g}{C_\Sigma} \tag{3.2}$$

where alpha is the "lever arm" conversion between the applied gate voltage and the actual change in island energy.

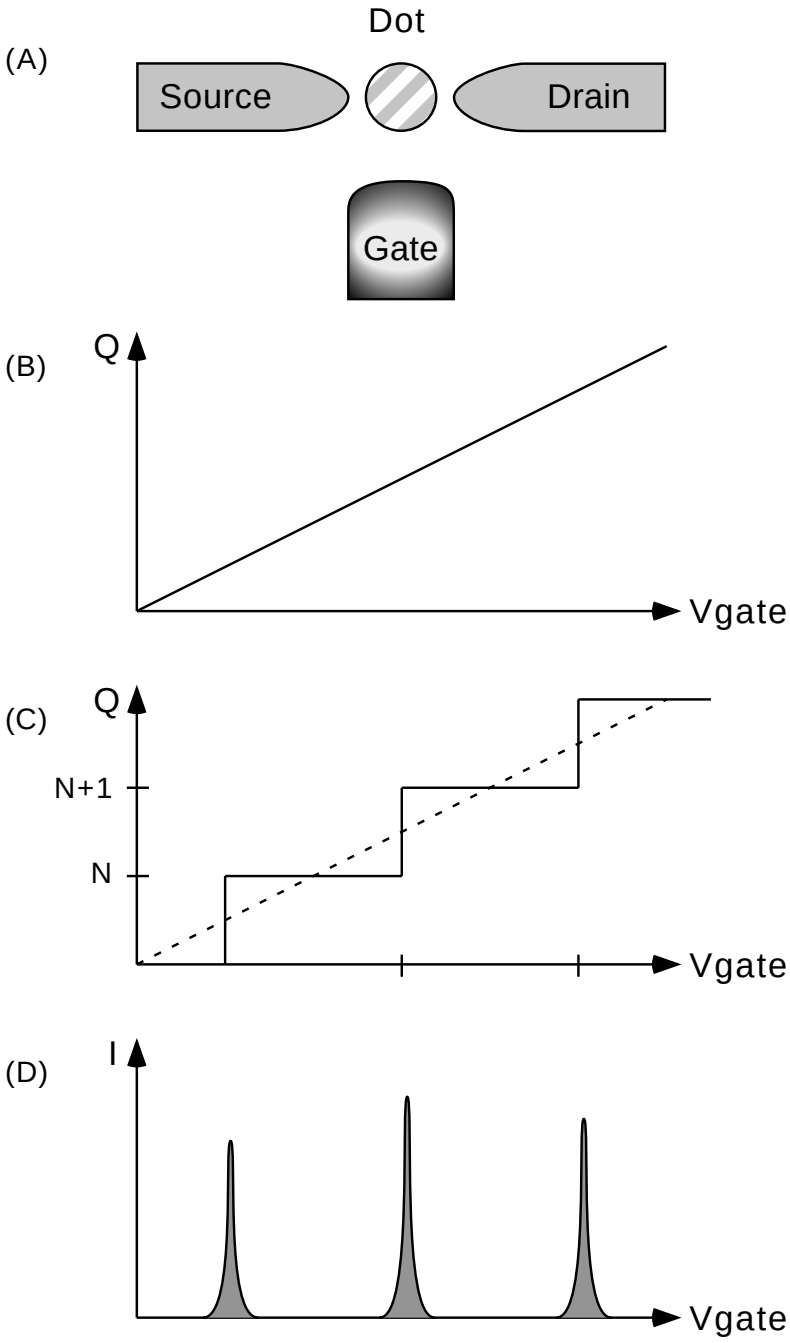

Figure 3.1: (A) Schematic of the quantum dot system (B) The linear Q=CV relation for a macroscopic capacitor (C) The staircase Q=CV relation for very small capacitances (D) At the electron number degeneracy points current can flow through the source-dot-drain system.

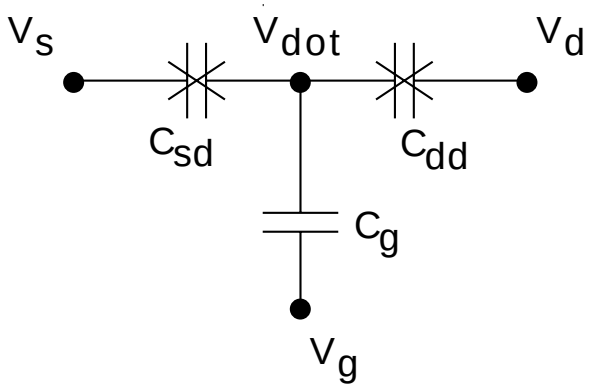

Figure 3.2: An equivalent circuit for the QD system. A capacitor with an X indicates that electron tunneling through the capacitor is possible.

Observation of this charging energy effect requires that the island charge truly be discrete, or equivalently that the island be sufficiently isolated from the rest of the environment. The isolation is sufficient to spatially localize electrons on the island when the tunnel resistances R_T to the source and drain are both larger than the quantum of resistance R_Q , $R_T \gg R_Q = h/e^2 = 25813\Omega$. Additionally, blockade of the tunneling also requires that the charging energy gap be larger than the thermal electron energy in the source and drain. Even for the femto-Farad capacitances of our quantum dot system, this requires system temperatures below 1K.

3.3 Quantum Confinement Energy

A particle confined in any finite system exists only at discrete eigenenergies and in unique spatial eigenfunctions. These eigenenergies and functions are solutions to the Schrodinger equation (Eqn 2.2) for the particular confining potential. Our quantum dot is effectively a very small 2D system. The density of states (DOS) of any 2D system is constant as a function of energy, with an average energy spacing between spin-degenerate levels of

$$\Delta = \frac{\partial E}{\partial n} = \frac{2\pi\hbar^2}{m^* l^2} \tag{3.3}$$

where m^* is the electron effective mass and $A = l^2$ is the 2D area of the device.

3.4 Quantum Dot Tunneling Spectra

3.4.1 Coulomb blockade in a quantum dot

Electrons in the quantum dots studied here are physically confined to a 2D disc of radius $l \sim 300nm$. We can use this length to estimate both the capacitive charging energy and the quantum confinement energy scales. The dot can be crudely modeled as a parallel plate capacitor with the area $A = 0.1\mu m^2$, distance to the second electrode (the ionized doping layer) of $40nm$, and dielectric constant of AlGaAs ~ 13. This yields a capacitance of $C \approx 260aF$ and a charging energy $E_C \approx 0.6meV$. The quantum confinement energy can be estimated using the 2D level density of Eqn 3.3, from which we find the single particle level spacing $\Delta \approx 36\mu eV$. Spectroscopic resolution of the charging energy ladder requires that the $\sim 3.5kT$ thermal smearing of the Fermi surface is less than the spectral gap of $0.6meV$. This corresponds to an electron temperature $T_e < 2K$. Resolution of the single particle spacings is more difficult, and requires $T_e < 100mK$ (Table 4.1 lists these relevant GaAs and QD parameters).

For our quantum dot system, the charging energy is 10-20 times larger than the quantum confinement discretization. We will see below that this ratio of E_C/Δ also determines how many of the single particle quantum levels can be accessed in the transport spectroscopy measurements. Using finite source-drain bias to tunnel into excited quantum dot states, we are able to access an energy window of width $2E_C$ centered at the QD Fermi energy, while still tunneling only one electron at a time. The spectroscopic measurements reported here therefore characterize the quantum levels immediately above and below the QD Fermi level.

3.4.2 Ground states tunneling spectra

At zero temperature and at infitesimal source-drain bias, all electron tunneling occurs into and out of a single quantum level in the QD. Continuous perturbations to the quantum dot such as confinement shape or magnetic field changes cause parametric variations of this quantum level energy and eigenfunction. This quantum level is the $N + 1$ ground state; current flows as the QD oscillates back and forth between the N and $N + 1$ ground states. In this "zero bias" regime the injected electron tunnels into the lowest available quantum level only when it's Fermi energy E_F is equal to the charging energy plus the additional quantum energy spacing beween the highest occupied and lowest unoccupied 0D

states, $E_F = E_C + \Delta_{N+1}$. Figure 3.3A illustrates this oscillation between the $N = 4$ and $N = 5$ ground states, which occurs when the gate voltage is tuned exactly to the $N = 4, 5$ degeneracy point. Figure 3.3B shows the same QD after the gate voltage is tuned slightly off resonance, and the device is back in the Coulomb blockaded mode.

The current and conductance through the QD is now quasi-periodic in the gate voltage. The perfect periodicity of the constant interaction charging energy ladder is modified by the additional quantum confinement spacing term. Variations in the separation between successive peaks reflect the distribution of the quantum level spacings. We note that in a simple single particle model the spin degeneracy of each level would yield an even-odd structure in the CB peak spacings. At even N one would expect all QD levels including the highest occupied level to be doubly filled, whereas at odd N the highest occupied level would be only half filled. Even N to odd $N+1$ transitions would therefore show an energy spacing of $E_C + \Delta$, and odd $N+1$ to even $N+2$ would show an energy spacing of E_C only.

In this zero bias regime the conductance of a CB peak is well described by first order resonant tunneling processes. Beenakker et al. have calculated this conductance in the limit of minimum intrinsic level broadening $\Gamma \to 0$ for both low temperature $\Gamma < kT < \Delta < E_C$ where tunneling occurs through a single level [Beenakker91a],

$$G = \pi \frac{e^2}{h} \frac{\Gamma_L \Gamma_R}{\Gamma} \frac{kT}{2} \cosh^{-2} \left[\frac{E_0 - \alpha e V_g}{2kT} \right] \tag{3.4}$$

where Γ_L, Γ_R are the source-dot and dot-drain couplings, E_0 is the resonant level energy and α is the gate voltage lever arm from Eqn 3.2. For finite temperature $\Gamma < \Delta < kT < E_C$ when tunneling occurs via all quantum levels within the smeared Fermi surface energy window,

$$G \simeq \frac{1}{4\Delta} \frac{e^2}{h} \frac{\Gamma_L \Gamma_R}{\Gamma} \frac{kT}{2} \cosh^{-2} \left[\frac{\mu_0 - \alpha e V_g}{2.5kT} \right] \tag{3.5}$$

Although the lineshapes are identical, their widths differ in that the $FWHM = 3.5kT$ for the single level case and the $FWHM = 4.35kT$ for the multi-level case. These exact descriptions of the tunnelling line shape and energy width will be used to calibrate the lever arm conversion between capacitively coupled gate voltages and true QD energy.

More significantly, in the low temperature limit the amplitude of a single CB peak is simply modeled as proportional to the overlap of the wavefunction in the dot with the wavefunctions in the source and drain. Fluctuations of CB peak heights thus indicate tunneling through different unique QD spatial wavefunctions.

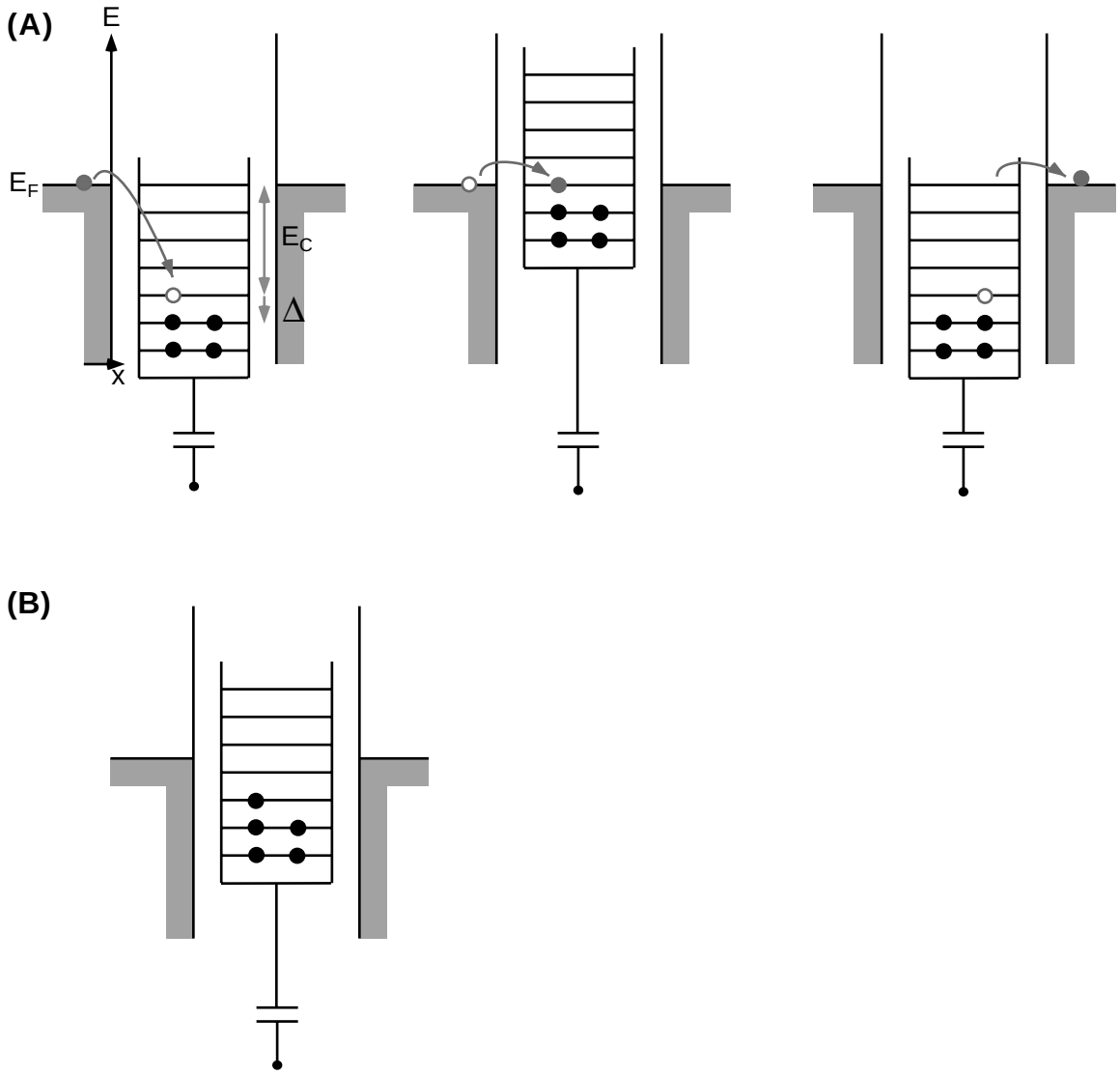

Figure 3.3: (A) The sequence of electron tunneling events when the gate voltage V_g is biased to the N=4,5 charge degeneracy point. The lowest unoccupied QD level is exactly E_C below the source Fermi energy. The cycle repeats to yield a continuous current flow. (B) Coloumb blockade is enforced when the gate voltage is tuned only slightly more positive and the charge becomes fixed at N=5.

In the Coulomb blockade area between resonant peaks the current and conductance due to first order tunneling processes are effectively zero. Second order processes are then the dominant contribution to the tunnel current, processes by which one electron tunnels directly from source to drain via a virtual QD state, or by which one electron tunnels onto the QD while simultaneously a second electron tunnels off the QD. Known as "electron cotunneling" or "macroscopic quantum tunneling", these second order processes have been characterized both theoretically and experimentally [Maurer98; Cronenwett97]. In this work we focus exclusively on the first order CB tunneling peaks, and use perturbation by a magentic field to investigate parametric behavior of the ground state energies and eigenfunctions.

3.4.3 Excited states tunneling spectra

At finite source-drain bias, $V_{DS} > \Delta$, multiple quantum states in the QD are available for electron tunneling. Electrons in the source with energies between E_F and $E_F - V_{DS}$ can tunnel into any aligned and unoccupied QD state, including both the $N+1$ ground state and any available $N+1$ excited states. The tunneling density of states will therefore show signatures of transport through both the ground and excited QD states.

For a well isolated QD, low dc current levels and/or fast energy relaxation within the dot, the QD will always begin each tunneling transition in it's ground state. An electron tunneling from the source onto the QD will cause a transition from the N ground state to an $N+1$ ground or excited state. The dot will then relax to the $N+1$ ground state before tunneling out to the drain occurs, which will then be a transition between the $N+1$ ground state and an N ground or excited state. Again, fast relaxation or long tunneling times will ensure that the dot relaxes to the N ground state before another electron enters and the cycle repeats. If correct, this description simplifies the measured spectrum considerably and limits the visible resonances to two distinct sets of transitions: N ground to $N+1$ ground or excited, and $N+1$ ground to N ground or excited. If complete relaxation does not occur then energies corresponding to transitions between excited N and excited $N+1$ states will appear in the spectrum, increasing the difficulty of interpretation. In most of our discussion and analysis we use the complete relaxation assumption. We justify this with data presented in Section 6.3, but add that some of the data in Section 6.5 contradicts this assumption and indeed shows that complete relaxation within the QD does not always occur. We note that the QD isolation is continuously tunable using the quantum point

contact (QPC) gate voltages that define the source-dot and dot-drain barriers, and thus we expect to be able to access both regimes of complete relaxation (inelastic tunneling) and no energy relaxation (elastic tunneling) by tuning the QPCs.

If the QD conductance is measured via application of a small ac signal to the source-drain voltage, the differential current is due to peaks in the QD DOS aligning with the source Fermi level or drain Fermi level only. In a single particle picture of the QD quantum spectrum these DOS peaks are simply *successive single particle states*. A dc current will flow through all of the states lying between the source and drain Fermi energies, but the small signal conductance $g = \partial I/\partial V_{DS}$ will show a peak only when an individual level aligns with the source or drain E_F. Instead of the single, sharp zero bias CB peak, the finite bias QD conductance displays a cluster of resonances as the gate voltage is swept past the $N, N+1$ charge degeneracy point. This difference between zero bias and finite bias conductance is illustrated qualitatively in Figure 3.4.

The change from a single peak to multiple resonances is a continuous function of the applied source-drain bias. Figure 3.5 is a gray scale image of experimental conductance data as a function of gate voltage V_g and drain-source voltage V_{DS}. At $V_{DS} = 0$ the familiar sharp CB peaks can be seen, roughly equally spaced in V_g. Increasing V_{DS} results in broadening of the CB peaks to form multiple peak structures enclosing the so-called "Coulomb diamonds". The central areas of the Coulomb diamonds (white in Fig. 3.5) correspond to the blockade regime of zero conductance and fixed electron number. Dark stripes parallel to the Coulomb diamond edges are peaks in the differential conductance; each stripe represents the transmission resonance of a single QD level aligned with the source or drain Fermi levels. For positive V_{DS} we identify the resonances parallel to the negative slope Coulomb diamond edge as unoccupied QD levels in resonance with the source; namely, such peaks correspond to electrons tunneling into successive unoccupied states of the QD.

Single-electron tunneling will occur as long as the $N+1$ ground state lies within the source-drain energy window. If we examine only the QD levels in resonance with the source Fermi level, tuning the gate voltage more positive will sweep successive $N+1$ excited states into alignment with E_F source and yield the peaks in conductance. The first conductance peak will correspond to the $(N)_{ground}$ / $(N+1)_{ground}$ transition. Subsequent peaks will correspond to the $(N)_{ground}$ / $(N+1)_{1^{st}excited}$, then $(N)_{ground}$ / $(N+1)_{2^{nd}excited}$ etc. transitions. In this way the signature of transport through each level in the spectrum of the $N+1$ QD can be measured individually. We will see in the data of Section 6.3 that

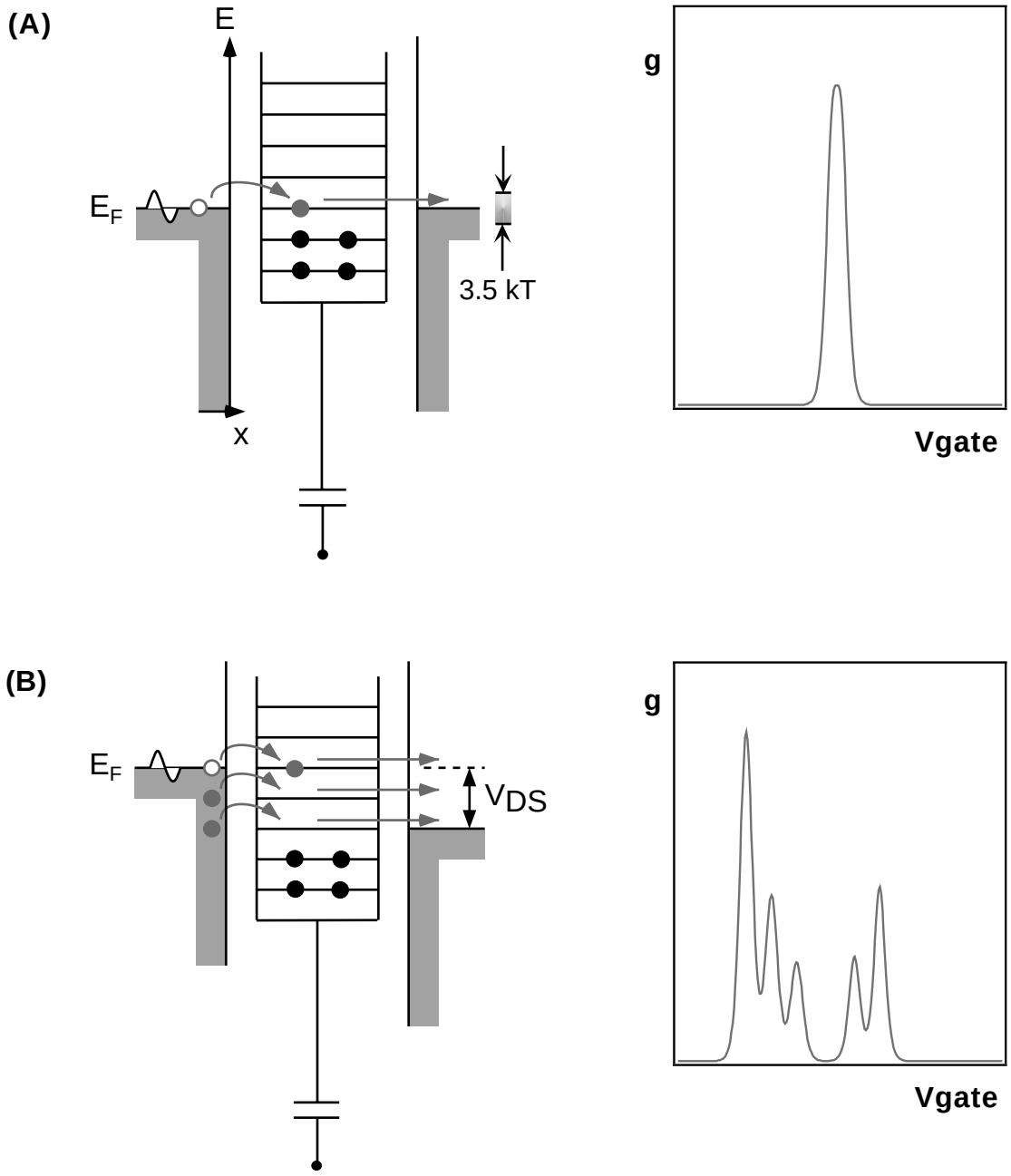

Figure 3.4: (A) Small signal "zero bias" case. Tunneling is through the single lowest unoccupied QD state, corresponding to the N+1 ground state. The conductance shows a single sharp peak. (B) Finite bias case. Multiple QD levels are available for tunneling, corresponding to N+1 excited states. The conductance shows a set of resonance peaks.

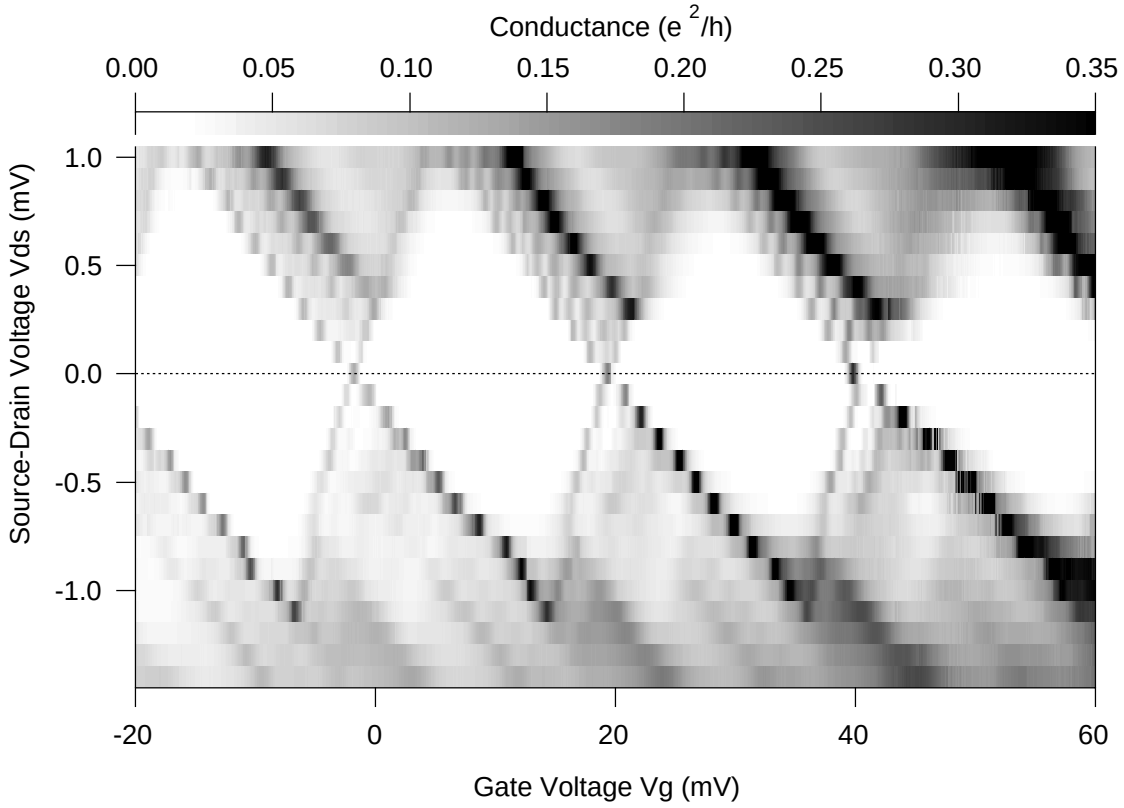

Figure 3.5: Experimental QD conductance as a function of source-drain voltage and gate voltage. White diamond areas are Coulomb blockade regions of zero current and zero conductance. Black stripes parallel to diamond edges are successive transmission resonances.

these conductance peaks, and in particular their parametric dependence on magnetic field, can be used to uniquly identify each quantum state of the QD.

Tuning the source-drain bias controls the energy width of the transport window between source and drain Fermi levels. Resonances due to successive quantum levels will be separated in gate voltage by approximately the single particle energy spacing Δ. The number of individual quantum states accessible at a given V_{DS} is then simply V_{DS}/Δ. Note also that for $V_{DS} > E_C$, the Coulomb blockade suppression of tunneling is lifted. Single-electron tunneling is allowed regardless of gate voltage tuning and the Coulomb blockade restriction now constrains only the simultaneous tunneling of a second electron. The opportunity for simultaneous two electron tunneling makes transitions between N, $N+1$ *and* $N+2$ states possible and further complicates the measured spectrum. For this reason, the ratio of

E_C/Δ determines the maximum number of experimentally resolvable and interpretable QD quantum states. In the experimental results we focus on the E_C/Δ states above the QD Fermi energy, by measuring the tunneling behavior due to these levels aligning resonantly with the source Fermi level.

3.5 Model of quantum dot electron tunneling

An improved understanding of the Coulomb diamond conductance pattern is achieved using a numeric model to simulate tunnel current through the QD. We base the model on a fixed single particle spectrum filled with N electrons, and add the charging energy requirement as a constant energy cost per electron. By assuming a single particle spectrum, we are ignoring all possible interaction effects on the electronic spectrum. For simplicity, we also ignore the spin degeneracy of each quantum level. Nevertheless, the model yields considerable insight into the Coulomb diamond patterns.

The basic model result of Figure 3.6 is the reproduction of the parallel stripes in the Coulomb diamond experimental measurement. These stripes are peaks in the differential conductance, arising from resonant alignment of a QD DOS peak with the source or drain Fermi levels. In our model the QD DOS is simply a ladder of δ-functions, representing the discrete quantum spectrum of the QD. Adjacent parallel stripes in the diamond then correspond directly to the successive states of the discrete single particle spectrum. If we examine the N, $N+1$ CB oscillation, filling all levels up to the $N+1$ level yields the "$N+1$ ground state" of the QD. Tunneling into and out of the $N+1$ level yields the zero-bias CB peak. As the source-drain bias is increased, the single CB peak broadens into a wide "hand" with multiple individual resonance peaks. Each peak forms a stripe parallel to one of the two diamond edges. Stripes parallel to each of the two edges are successive QD levels aligned with the source or drain, as indicated in Figure 3.7. The first and last of these individual peaks correspond to the alignment of the $N+1$ "ground state" level with the source and drain respectively. Counting inward from either edge the stripes correspond to tunneling through the successive QD levels above and below the $N+1$ level, as labeled. Note that the pattern of level resonance labeling is symmetric with respect to reflection in the $V_{DS} = 0$ line.

Two further assumptions were employed to achieve the result of Figure 3.6. The first is the assumption of total relaxation within the QD before each tunneling event, ie. the QD

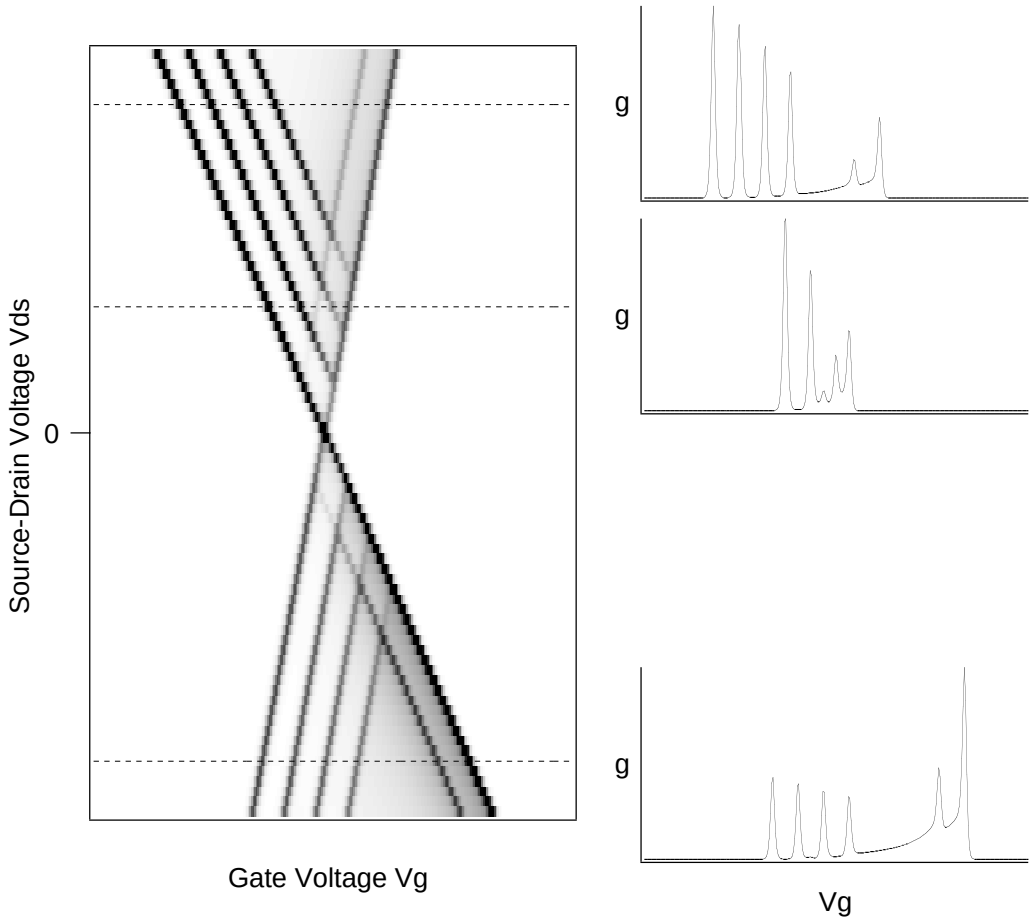

Figure 3.6: (Left) The calculated QD conductance for a single CB peak as a function of source-drain bias and gate voltage. Compare to Figure 3.5. (Right) Select cross-sections of the conductance plot at left, indicated by adjacent dashed lines.

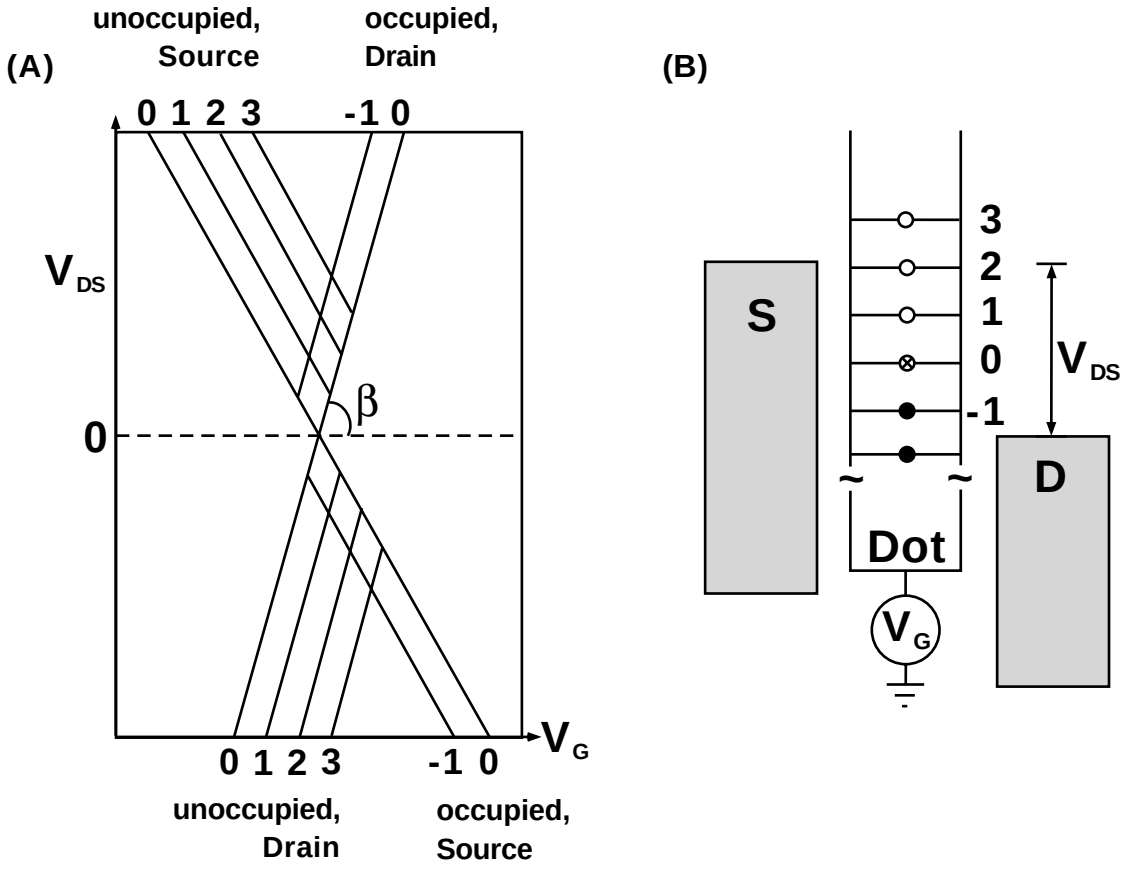

Figure 3.7: (A) Schematic diagram of the Coulomb diamond resonance lines, labelled to indicate how occupied/unoccupied QD levels align resonantly with the source or drain Fermi levels. Numbering of resonance lines corresponds to the labeled levels of (B).

begins each tunneling transition in its ground state, either N or $N+1$ in this case. The validity of this assumption was discussed in Section 3.4.3, with the principal requirements being very good QD isolation, low dc current levels and low temperature $kT < \Delta$. The practical impact of this assumption is to simplify calculation of the current through the QD. The computer code used to perform the calculations is included in Appendix A. Accepted as inputs to the model are the relative magnitudes of the intrinsic level broadening Γ_N, ac bias applied V_{ac}, system temperature kT, single particle level spacing Δ and charging energy E_C. For the model results of Figure 3.6, $\Gamma_i = \delta(E_i)$ and $V_{ac} < kT < \Delta \ll E_C$. This is the low temperature, well quantized regime that we are attempting to study experimentally, however within the model all five of these parameters can be varied in order to simulate other regimes. In particular, experimentally $\Delta \sim 2kT - 8kT$. The results of Figure 3.6 used an artificially low temperature $kT = \Delta/20$ to increase visibility of the resonance stripes.

A brief description of the model calculations will clarify their validity limits. The ac current through the QD is calculated by numerically differentiating the calculated dc current. The dc current through the device was taken as the inverse of a single-electron transit time, where the total transit time was the sum of the time to tunnel in and the time required to tunnel out. Each tunnel time was found from the inverse of the corresponding tunnel rate. Each tunnel rate was assumed proportional to the sum of rates into or out of any available channels ie QD quantum levels, where the rate of a single channel was determined from it's integrated width with respect to that lead (Γ_L or Γ_R) multiplied by the Fermi-Dirac distribution of occupied/unoccupied states in that lead. Quantitatively this is

$$I_{dc} = \frac{1}{\tau_{transit}} \tag{3.6}$$

$$\tau_{transit} = \frac{1}{\gamma_{in}} + \frac{1}{\gamma_{out}} \tag{3.7}$$

$$\gamma_{in} = \sum_{i=N+1}^{\infty} \Gamma_i \left[\frac{1}{1 + e^{\frac{E_i - \mu}{kT}}} \right] \tag{3.8}$$

$$\gamma_{out} = \sum_{i=-\infty}^{N+1} \Gamma_i \left[1 - \frac{1}{1 + e^{\frac{E_i - \mu}{kT}}} \right] \tag{3.9}$$

The rate sums over the specified levels above or below the $N+1$ level make explicit the complete relaxation assumption and the assumption of low temperature $kT < \Delta$ within the QD.

We can use the model output to understand many of the Coulomb diamond features. Here we describe the parameters and effects controlling the angle of the diamond edges, the relative heights of the finite bias resonance peaks, the relative widths of the finite bias peaks and the appearance of negative differential conductance.

The angle of the Coulomb diamond edges is determined from the relative resistances and capacitances between the source-dot and dot-drain. The question being asked is straightforward: how much of the source-drain voltage drops across each source-dot and dot-drain barrier ? This is solved using the equivalent circuit of Figure 3.2, where each barrier is represented by a capacitor that can be tunneled through. The dc solution would normally consider the capacitors as open circuits and derive the dot voltage using any series resistors. However in our case, $R_T > R_Q$ and the resistors are effectively infinite; the dot voltage is then determined from the capacitor network. Equal capacitances mean that half of the applied voltage drops on each barrier and the Coulomb diamond angles are symmetric for positive and negative bias. Unequal capacitances determined by lithographic QD design are the normal experimental case, and mean that the voltage drops unequally and the angles of the diamonds are symmetric only under a 180^o rotation about the $V_{DS} = 0$, $V_g = (N, N+1)$ degeneracy point. The angle β of Figure 3.7, for equally scaled energy axes V_g and V_{DS}, is then:

$$\beta = \arctan(\frac{C_d + C_s}{C_s}) \tag{3.10}$$

For equal capacitances this angle is $\beta = 63^o$; for the asymmetric extremes it has a minimum value of 45^o and a maximum of 90^o. This angle also affects the relative intensity of source and drain conductance resonances. Conductance is measured by differentiating the dc current in the vertical V_{DS} axis. The more oblique the angle between the Coulomb diamond edge and the vertical V_{DS} axis, the weaker the conductance resonance. This is exactly analagous to steepness of slope seen by a skier climbing perpendicularly or obliquely to the contour lines of a hillside. Asymmetry in the capacitances thus enhances the source resonances and suppresses the drain resonances for one polarity of applied bias and then reverses this enhancement for the opposite bias polarity.

One trend in the relative heights of the finite bias resonances can also be understood within this model. Experimentally, the finite bias resonances are frequently highest near the diamond edge and decrease in amplitude towards the middle of the finite bias cluster. Using the model, if we assume that all levels have equal and normalized coupling to the left and right leads, ie $\Gamma_L = \Gamma_R = 1$, then the zero bias CB peaks are all the same height. In finite

bias however, subsequent resonances counting inward from either edge of the diamond do indeed decrease in height. This is visible in the intensities and cross-sections of Figure 3.6 and can be understood when the detailed description of current flow is considered (Eqn 3.7). Increasing the bias opens more channels for transport through the QD. Consider the case when an increase in the source Fermi level includes a second unoccupied QD level, and we examine the differential conductance peak due to this new level. At low temperature $kT \ll \Delta$, the subsequent increase in dc current is discrete. The addition of the second unoccupied level will double the tunnel rate *into* the QD; the tunnel rate out however will remain the same. The addition of the two rates in the denominator of Eqn 3.6 effectively "dilutes" a fractional change in either individual rate. In our case the total transit time decreases from $\tau_{transit} = 1 + 1 = 2$ to $\tau_{transit} = 0.5 + 1 = 1.5$, so the dc current increases from 0.5 to 0.66. If we repeat this analysis for the case when the third unoccupied level is resonant with the source, the tunnel rate into the QD will increase from 2 to 3 channels, the total transit time decreases from $\tau_{transit} = 0.5 + 1 = 1.5$ to $\tau_{transit} = 0.33 + 1 = 1.33$ and the dc current increases from 0.66 to 0.75. This is a smaller absolute change than the 0.5 to 0.66 transition, and hence yields a smaller differential conductance peak. Inclusion of subsequent levels yields progressively smaller changes to the total current. Thus even for identical level couplings in the QD spectrum, finite bias resonance heights should decrease from the edge of the Coulomb diamond towards the center of the cluster as Figure 3.6 shows. Experimentally, fluctuations of finite bias resonance heights around this decreasing trend can be attributed to the random couplings of true successive QD eigenstates.

The relative widths of finite bias peaks can also be studied within the constraints of the model. At finite temperature $0 < kT < \Delta$, the width of each resonance is simply the thermal width of the Fermi surface in the lead. This width is constant for all resonances in the cluster, and obeys Eqn 3.4 . There are thus no broadening effects intrinsic to the transport through multiple channels as described by Eqn 3.6 ; any level broadening that appears in the experiment will be significant and attributable to electron-electron interaction effects.

Another effect that will appear in the data should be discussed here – negative differential conductance (NDC) within the finite bias resonance cluster. This effect does not appear in the complete relaxation model, but by simple extension of the model one possible mechanism for NDC can be proposed. If the dot always relaxes between transitions, then inclusion of an additional channel at the source or drain, no matter how small the Γ_L or Γ_R, will

always increase the total current and thus yield a positive conductance peak. However, at the other extreme of zero relaxation, each electron will tunnel into and out of the same quantum level. A level with weak couplings would then allow an electron to tunnel into the QD and effectively trap it for some time before it tunneled out. The total current would be proportional to the *average coupling* over all available transport channels, and the addition of a level with below average coupling would decrease the dc current. The finite bias cluster would then show a negative differential conductance peak instead of a positive peak. The experimental appearance of these NDC peaks is discussed in Section 6.5, and will be interpreted as evidence that complete inelastic relaxation does not always occur during transport through the QD.

Finally we discuss the effect of unequal QPC resistances on the finite bias conductance peaks. The angle of the Coulomb diamonds in the limit of large tunnel resistances is set by the capacitances of Figure 3.2, and has a direct impact on the relative intensity of the source and drain resonances, as described above. Asymmetry in the QPC tunnel resistance also affects the relative source and drain resonance amplitudes. This is accomplished by closing the source QPC and opening the drain QPC, effectively increasing the source-dot barrier and resistance and decreasing the dot-drain barrier and resistance. In this configuration it is difficult to tunnel into the QD, and easy to tunnel out. The rate of tunneling out is always high, and hence the second term in the denominator of Eqn 3.6 always small. New additional channels out to the drain cause little fractional change in the dc current. The current is limited by the source-dot tunnel process, and additional channels in from the source now cause a large fractional change, and produce a large amplitude conductance resonance. This is a trade off; the conductance resonances of the drain are suppressed. Figure 3.8 compares the balanced QPC current and conductance curves to the closed source QPC, open drain QPC current and conductance results. Experimentally we use this effect to selectively highlight the source resonances, allowing better resolution measurements of the $N + 1$ excitation spectrum.

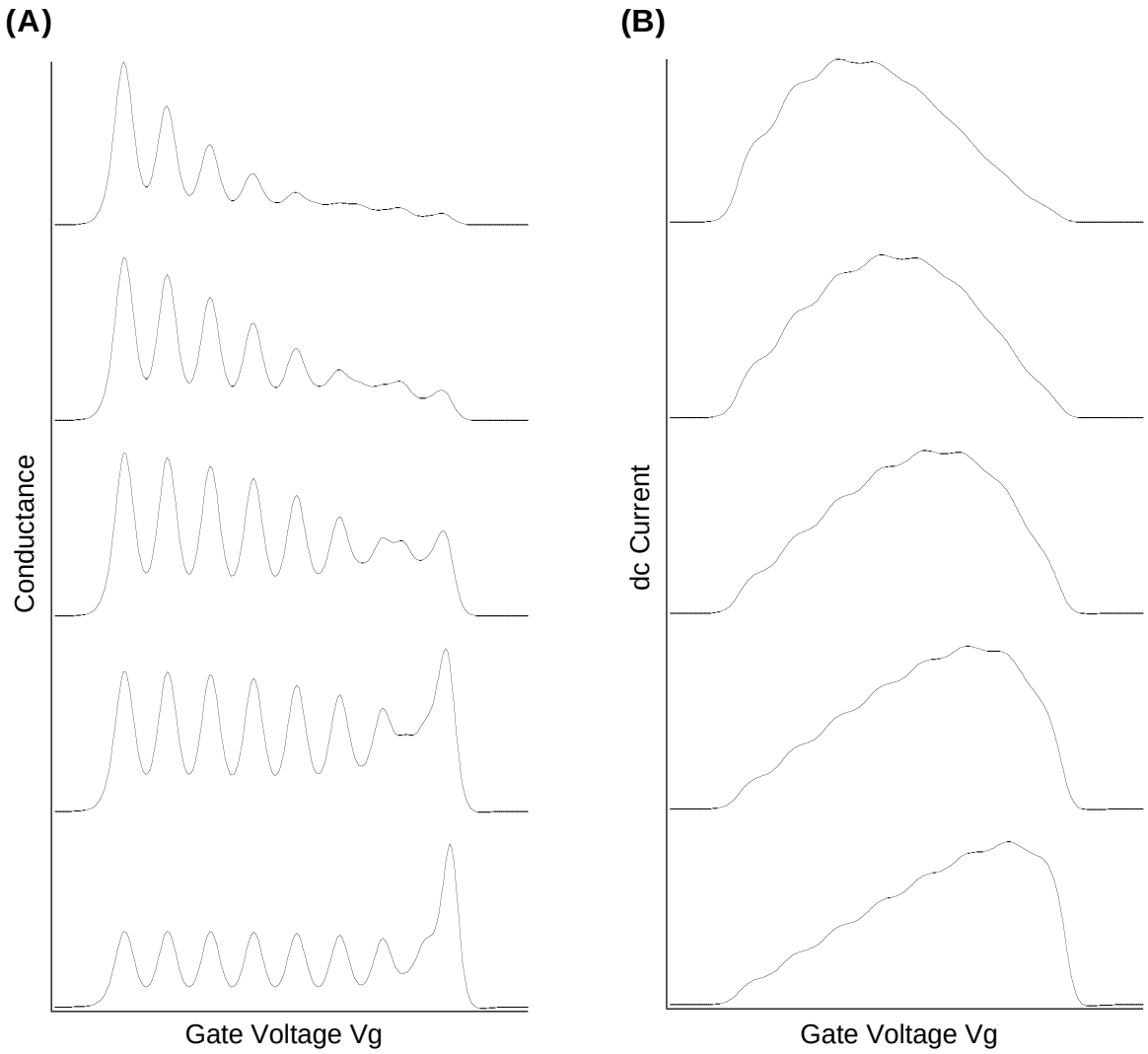

Figure 3.8: (A) The calculated conductance at fixed source-drain bias, with $\beta = 70^o$, for successive asymmetrically tuned quantum point contacts. The top curve is for an open source / closed drain, the middle curve for balanced QPCs and the bottom curve for a closed source / open drain. (B) The calculated dc current for the same tunings of the QPCs.

Chapter 4

Experimental system

4.1 Introduction

The construction of tiny "artificial atom" quantum dots requires confinement of electrons in all three dimensions on a sub-micron scale. Two basic methods exist for achieving this confinement: self-assembly of a 3D island composed of one material of small electronic bandgap within a second host material of larger bandgap, or lithographic patterning and electrostatic confinement of a previously created 2D electron system. Both methods can be applied to many different metal and semiconductor materials systems. The well characterized and experimentally powerful system of a GaAs/AlGaAs two-dimensional electron gas (2DEG) with surface electrostatic split-gates deposited and patterned lithographically was used to construct all the quantum dot devices described in this work [Beenakker91b].

The architecture and parameters of the Molecular Beam Epitaxy (MBE) grown heterostructure will be described in Section 4.2. Section 4.3 outlines the process of lithographically patterning this substrate to create the 2D electrostatic confinement of the quantum dot. Section 4.4 describes the apparatus and measurement configurations used to aquire all experimental data.

4.2 Molecular Beam Epitaxy 2DEG substrate

The epitaxial structure of the GaAs/AlGaAs semiconductor substrate used in this work is illustrated in Figure 4.1A. The energy band diagram of this "modulation doped" structure is shown in Figure 4.1B. At low temperatures, electrons exist only where the conduction

band dips below the Fermi energy, within the narrow triangular well formed at the AlGaAs/GaAs interface. For normal 2DEG electron densities only the first sub-band of this triangular well is occupied, localizing the electrons in the z direction to within $100\dot{A}$ of the material interface. The second z sub-band is $\sim 150meV$ above the first. Since this energy is much greater than the typical Fermi energy $E_F \sim 10meV$, the measurement temperature $T < 1K = 86\mu eV$ and the source-drian bias $V_{DS} < 1mV$, the second sub-band remains unoccupied and the electron gas is dynamically two-dimensional. Spatial separation of the ionized silicon donor atoms from the 2DEG electrons by the undoped $40nm$ spacer layer reduces electron scattering, yielding very high electron mobilities and mean free paths in the buried 2DEG. When used in a commercial transistor, this buried conduction layer heterostructure is usually known as a high electron mobility transistor (HEMT) or a modulation doped field effect transistor (MODFET).

Typical electronic properties for 2DEG electrons of a GaAs/AlGaAs heterostructure are listed in Table 4.1. The 2DEG wafer used in these experiments was measured at $4.2K$ to have a mobility of $2\text{x}10^5 cm^2/Vs$ and a density of $2\text{x}10^{11} cm^{-2}$. This mobility yields a mean free path of approximately $1\mu m$, meaning that transport across the $0.3\mu m$ quantum dot structures studied was ballistic. This also implies that 0D quantum states inside the isolated QD are well defined wavefunctions coherent across the area of the QD. Electrons in 2D at this density occupy an average circular area of radius $130\dot{A} = 0.7a_{Bohr}$, when the Bohr radius a_{Bohr} is corrected for the GaAs dielectric constant and effective mass. This is referred to as the gas parameter r_s of this "free electron gas". Recall that r_s is also the ratio of potential interaction energy to kinetic electron energy (see Eqn 2.1), and $r_s \sim 1$ implies that interactions are not negligible, and may indeed modify the system behavior significantly.

4.3 Device fabrication

Fabrication of the quantum dot devices required both electron-beam (e-beam) and optical lithography processes. The grown wafer was cleaved into samples $7mm$ x $7mm$ square. Four lithographic steps were required: 1) optical mesas, 2) optical ohmics, 3) e-beam gates and 4) optical gates in that order. $800\mu m$ x $800\mu m$ isolation mesas were defined by a $1:8:240$ $H_2SO_4 : H_2O_2 : H_2O$ wet chemical etch. Each mesa next had four ohmic contacts deposited by thermal evaporation and liftoff of $250\dot{A}/150\dot{A}/2500\dot{A}$ of AuGe(eutectic)/Ni/Au. This

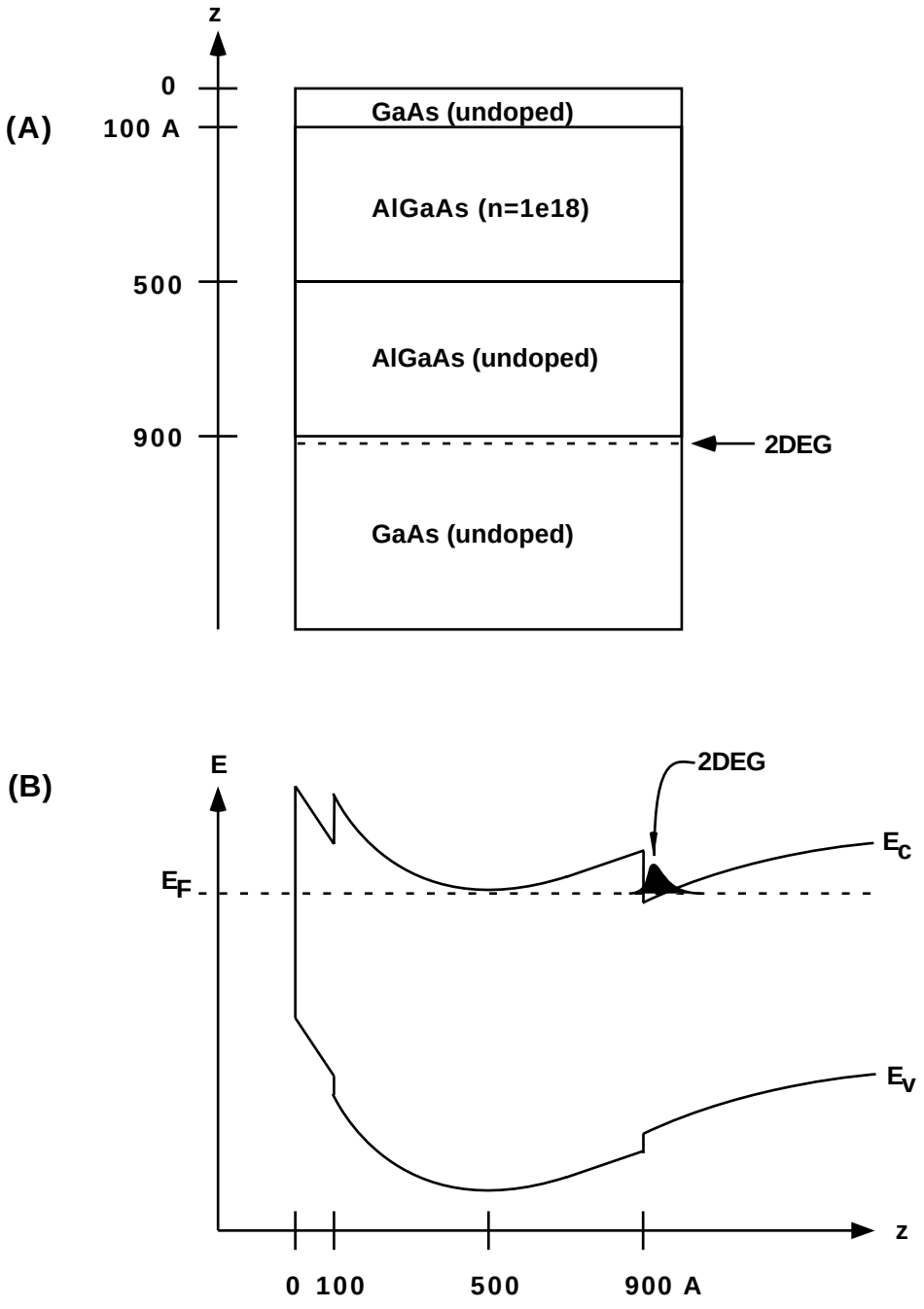

Figure 4.1: (A) A vertical growth profile of the top epitaxial heterostructure layers. (B) Energy band plot illustrating the triangular quantum well formed at the buried GaAs/AlGaAs heterojunction, and the single z-confined quantum state that falls below the Fermi level.

2DEG Property	Symbol	Value	Units
Effective mass	m^*	0.067	$m_e = 9.1\text{x}10^{-31} kg$
Spin degeneracy	g_s	2	
Valley degeneracy	g_v	1	
Dielectric constant	ε	13.1	$\varepsilon_0 = 8.9\text{x}10^{-12} Fm^{-1}$
Effective Lande factor	g_L^*	0.4	
Density of states	$\rho(E) = g_s g_v (m^*/2\pi\hbar^2)$	$2.8\text{x}10^{10}$	$cm^{-2}meV^{-1}$
Level spacing	$1/\rho(E)$	3.57	$\mu eV \mu m^2$
		41	$mK\mu m^2$
Fermi energy	$E_F = (\hbar k)^2/2m^*$	7.0	meV
		81	K
Fermi wave vector	$k_F = (4\pi n_s/g_s g_v)^{1/2}$	$1.1\text{x}10^6$	cm^{-1}
Fermi wavelength	$\lambda_F = 2\pi/k_F$	56	nm
Fermi velocity	$v_F = \hbar k_F/m^*$	$1.9\text{x}10^7$	cm/s
Scattering time	$\tau = m^*\mu_e/e$	4	ps
Mean free path	$l = v_F\tau$	$1\text{x}10^3$	nm
Resistivity	$\rho = 1/n_s e\mu_e$	300	$\Omega/$
Diffusion constant	$D = v_F^2\tau/2$	$7\text{x}10^3$	cm^2/s
Thermal diffusion length	$l_T = (\hbar D/kT)^{1/2}$	$1.6\text{x}10^3$	$nm/\sqrt{T}$
Cyclotron energy	$\hbar\omega_c$	1.73	meV/B
		20	T/B
Cyclotron radius	$l_c = \hbar k_F/eB$	70	$nm/\sqrt{B}$
Magnetic length	$l_m = (\hbar/eB)^{1/2}$	26	$nm\sqrt{B}$
Zeeman energy	$g_L^*\mu_B B$	23.2	$\mu eV/B$
		270	mK/B

Table 4.1: Properties of the 2D electron gas. When appropriate, values were calculated assuming a 2DEG density $n_s = 2\text{x}10^{11} cm^{-2}$ and mobility $\mu_e = 1\text{x}10^5 cm^2/Vs$. The units for B are in Tesla and for T are in Kelvin [Adapted from Foxman93b].

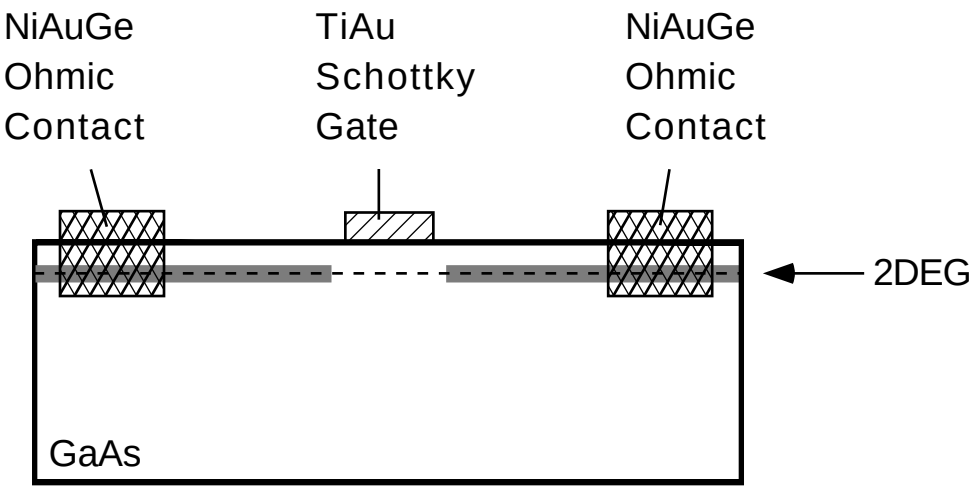

Figure 4.2: Cross-section through fabricated structure, indicating buried 2DEG layer, annealed ohmic contacts and surface Schottky gate.

deposited ohmic metal was annealed into the substrate at 440^oC for $60s$. E-beam patterning of a 4% 950K PMMA / 4% 495K PMMA bilayer was followed by thermal evaporation and liftoff of $50\dot{A}/250\dot{A}$ Cr/Au to form the smallest surface gate features. Larger surface gate bond pads were defined optically and deposited by thermal evaporation and liftoff of $250\dot{A}/2500\dot{A}$ Cr/Au. A cross-section schematic of the processed device structure is shown in Figure 4.2. Figure 4.3 is a scanning electron micrograph (SEM) perspective of a completed device.

A high magnification SEM of one of the devices measured is shown as the inset to Figure 4.3. A negative voltage ($\sim -0.5V$) applied to the five surface metal Schottky gates serves to deplete the 2DEG directly beneath each metal gate. More negative voltages extend the lateral depletion regions under each gate until the 2DEG is divided into three electrically isolated areas; a macroscopic "source", a small $0.3\mu m$ x $0.3\mu m$ quantum dot and a macroscopic "drain", connected by two "quantum point contacts". Physically, the electrons in the quantum dot are then confined to a thin disk of radius $r \sim 300nm$ and thickness $t \sim 10nm$. Electrical current flowing from source to drain is forced to transit through the isolated quantum dot island. Gate voltages can be tuned to independently control the point contact tunnel barriers, the dot areal size and the dot shape.

All devices fabricated had a nominally nonsymmetric 2D shape. This was a deliberate attempt to construct a dynamically chaotic cavity, one that might allow generalization of

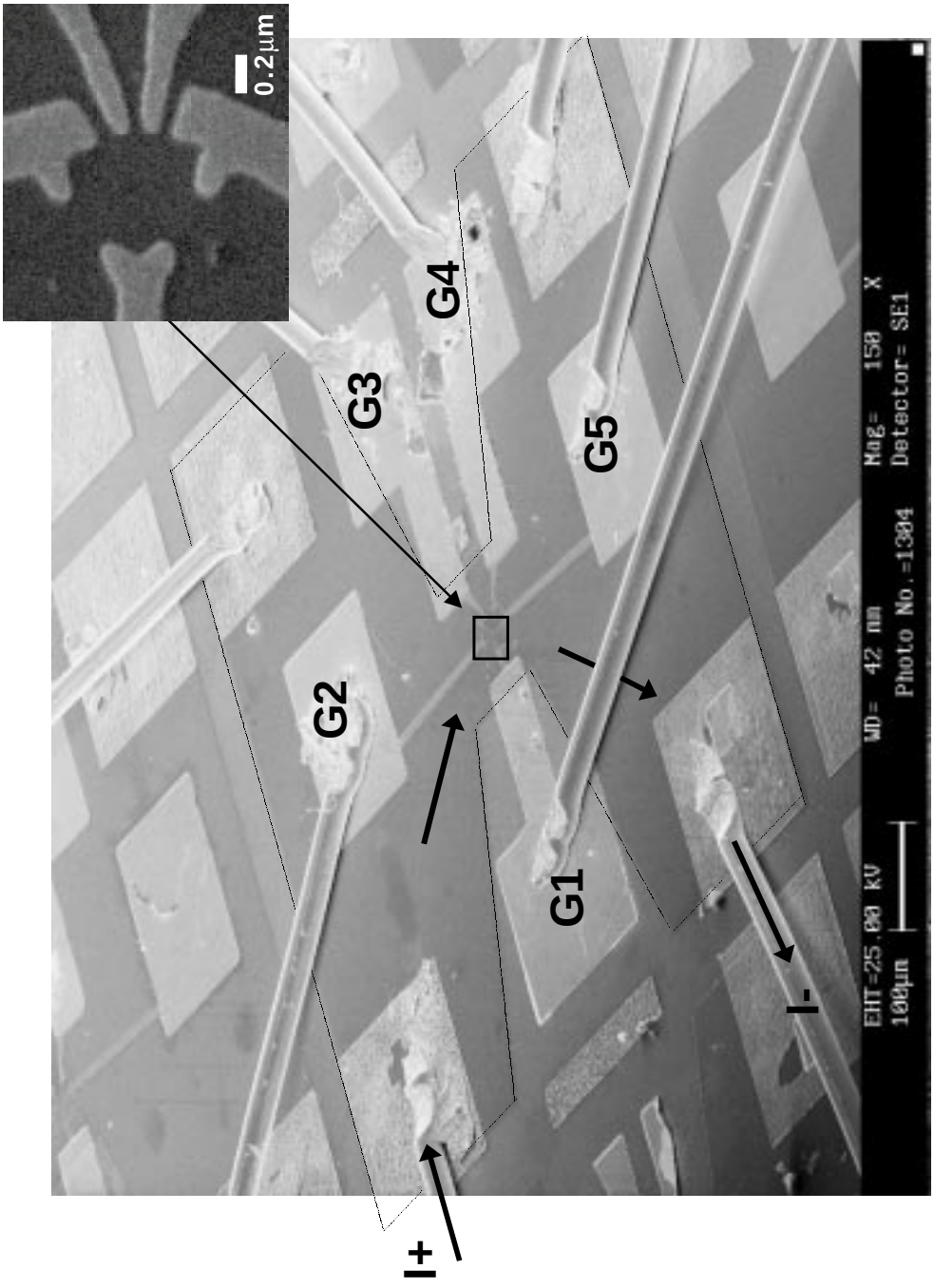

Figure 4.3: Scanning electron micrograph (SEM) of the fabricated device structure. Four ohmics are positioned at corners of the hourglass shaped etched mesa. Five surface gate pads (G1 through G5) extend fingers in to the center of the mesa where the quantum dot is defined. (Inset) A magnified plan-view SEM of the central quantum dot device. The five surface gates form the QD boundary.

the measured spectral behavior to the wider class of "generic" quantum chaotic systems. Also included was a deliberate effort to reduce or eliminate the effects of straight through trajectories and QPC focusing [Beenakker91b] by "aiming" the QPCs toward opposite triangular corners.

4.4 Measurement configuration

4.4.1 Apparatus

Experimental resolution of individual peaks in the tunneling density of states requires a temperature, and hence a smearing of the Fermi surface, that is smaller than the lowest energy scale separating adjacent peaks. The two relevant energy scales in the quantum dot spectrum are the charging energy and the confinement energy, $E_C \sim 2K$ and $\Delta \sim 100mK$ respectively. All electrical measurements were therefore done at $T \sim 50mK$ using a He^3/He^4 dilution refrigerator to allow resolution of the individual 0D quantum states.

Two ohmic contacts to each of the source and drain 2DEG reservoirs allowed both 2-wire and 4-wire electrical measurements. In the Coulomb blockade tunneling regime the small signal electrical resistance of the device is $R \geq 100k\Omega$ on a CB tunneling peak and $R > 10G\Omega$ between CB peaks. The average contact resistance was $0 - 1k\Omega$. Combined, these made a 2-wire voltage bias configuration the normal measurement mode. Figure 4.4 shows a schematic of the measurement configuration.

Small signal conductance $g = \partial I/\partial V_{DS}$ was measured directly using ac lock-in techniques. The ac signal at 13 Hz was generated by a PAR 124 lock-in amplifier. The dc source-drain signal was generated by a National Instruments AO6 A/D computer board. Ac and dc signals were voltage divided to $1 - 2\mu V$ ac and $0 - 1mV$ dc and added passively (see schematic Appendix A). The two-wire current of $0 - 10nA$ was amplified through an Ithaco 1011 current preamplifier, the ac signal returned to the lock-in amplifier input and the dc signal fed directly to a HP 34401A voltmeter. The lock-in output was also measured with a HP 34401A voltmeter. Data from both voltmeters were collected via the instrument GPIB computer interfaces.

Surface gate voltages were applied from the independent channels of a potentiometer controlled battery box. In series with selected battery box channels was an additional dc signal generated by the National Instruments AO6 A/D computer board. Each of six analog output channels had 12 bits of resolution within an independently addressable voltage range.

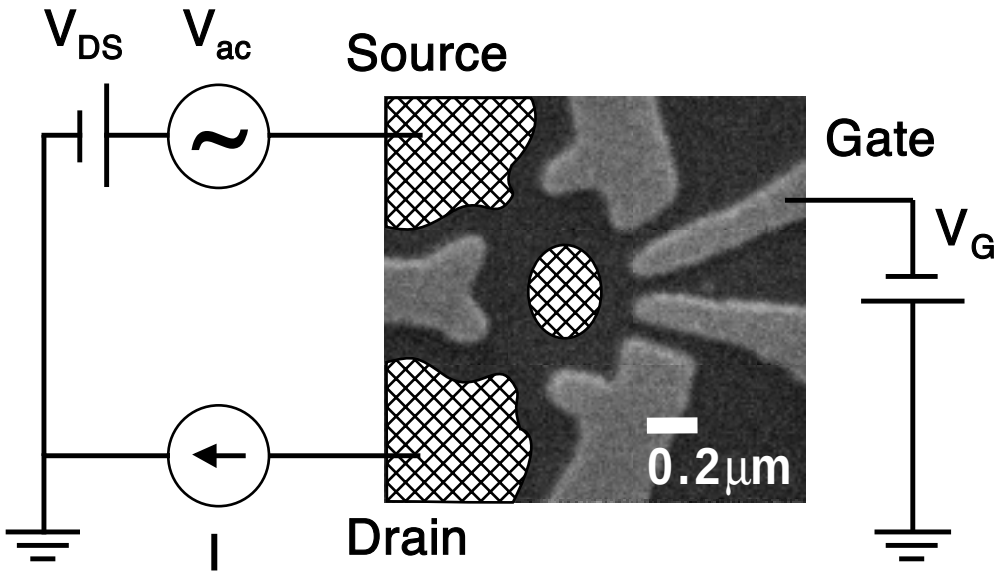

Figure 4.4: A measurement circuit schematic. Both ac and dc currents are passed through the source-dot-drain path. A negative voltage is applied to all surface gates to define the QD boundary, but only one gate (labeled V_g) is varied to continuously perturb the QD size and shape.

A further option allowed two AO6 channels to be stacked in series to provide the sum of two 12 bit signals with independent limits.

A 0-8 Tesla superconducting magnet provided a continuously tunable magnetic field perpendicular to the sample 2DEG plane. The magnet was driven with either a voltage controlled Kepco BOP or a voltage controlled Oxford 21 High Current Source. Both were supplied with a GPIB controlled Keithley 214 voltage source.

The source-drain bias, all AO6 connected gate voltages and the magnetic field were thus computer controlled, using the IGOR [©Wavemetrics Inc] software package. Arbitrarily complex control algorithms could be executed. The HP 34401A voltmeter data was recorded automatically.

4.4.2 Methods

Preparing the sample for measurement first involved cooling from $300K$ to the dilution refrigerator base temperature of $30mK$. It was found empirically that a slow cooling process lasting $\sim$ 24 hrs yielded lower noise device behavior than a fast $\sim$ 3 hr cooling process.

Although almost accepted as conventional wisdom, this conclusion has not been quantitatively documented within this work nor within the literature. Further, a positive voltage was frequently applied to the surface gates to forward bias them during the cooling process. This procedure also appeared to yield a lower noise device behavior, and is also not quantitatively documented in the literature. Telegraph noise at all frequencies corrupted many of the experimental measurements. We speculate that the slow cooling and positive bias allowed the silicon donor atoms to establish a lower energy equilibrium state, with lower inter-donor charge mobility due to higher total ionization fraction or spatial charge ordering. Application of positive bias during cooling may freeze more donors in a 2- DX configuration thus increasing the effective ionization fraction and decreasing charge mobility in the donor layer. The very low noise behavior of the particular devices measured was essential to the success of the experiment.

Once at low temperature, the surface gates that electrostatically defined the quantum dot were tuned to place the device in the Coulomb blockade regime. A negative voltage of $\sim 0.5V$ depleted the 2DEG beneath the surface gates, and pinched closed the two QPCs between the dot and source and the dot and drain. The properties of quantum point contacts have been studied in some detail [Beenakker91b]. For our measurements, the electrostatic barriers between the source/dot and dot/drain were tuned above the 2DEG Fermi level, and all transport through the dot therefore occurred via electron tunneling. The tuning of these two point contacts is most easily achieved by plotting device conductance as a function of the votage on the two gates controlling each QPC. A typical grey-scale plot of sample conductance for this measurement is shown in Figure 4.5. The Coulomb blockade regime is found in the lower left corner of the V_{qpc1}/V_{qpc2} space, where the tunnel resistance of each QPC is approximately equal and greater than $h/e^2 = 26k\Omega$ and thus discrete CB conductance peaks are clearly visible. At more negative gate voltages the QPC barriers are too high and prevent any measureable tunnel current; at more positive gate voltages the QPC barriers are too low and charge on the island is no longer quantized and the CB tunneling oscillations disappear.

Discrete zero-bias CB conductance peaks with lineshapes that closely fit Eqn 3.4 were generally found for those peaks whose maxima $g_{max} < 0.1e^2/h$. Deviations from the $\cosh^{-2}$ lineshape towards a lorentzian lineshape indicated the QPC tunnel resistances were too low. Asymmetries in the CB lineshape indicated unequal QPC tunnel resistances. Both effects were used to guide tuning of the surface QPC gate voltages to optimize the device

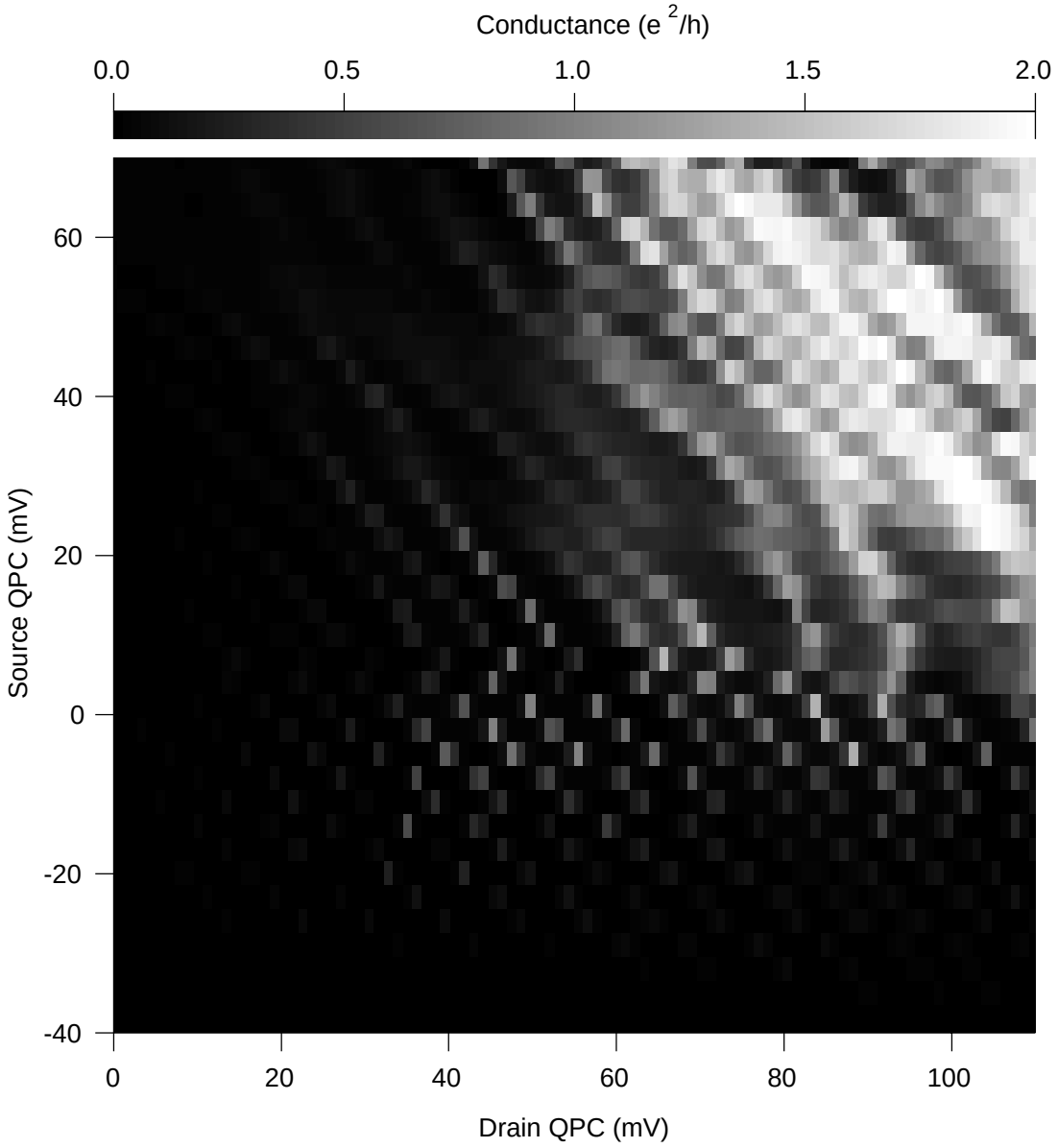

Figure 4.5: Experimental conductance at zero bias as a function of voltage on the source QPC and the drain QPC. Making either QPC more negative closes the QPC and pinches off the current. A corner exists in the source QPC / drain QPC space where the QD is well isolated from both source and drain but still shows measureable tunnel current at the Coulomb blockade degeneracy points. These are the discrete points at lower left.

measurement regime.

One or both of the plunger gates were used to smoothly change the size and confined electron number of the quantum dot. Capacitive coupling between the active plunger gate and any adjacent surface QPC gate unfortunately led to unwanted modulation of the QPC barrier by the plunger gate voltage. Reducing the dot size with a plunger gate tended to pinch off one or both QPCs until no measureable tunnel current remained. Increasing the dot size with a plunger gate opened the QPC channels until CB peaks had broadened beyond the minimum thermal FWHM. In the smallest $0.1\mu m^2$ devices, this limited the number of consecutive well resolved CB peaks to < 5. This unwanted capacitive coupling was partially corrected by actively controlling the QPC gate voltages to maintain a fixed tunnel barrier despite changes to the plunger gate voltages. With active QPC control, the number of optimally resolved CB peaks in the smallest devices increased to ~ 10, enabling measurements of the QD spectrum for N, $N+1$... $N+10$ confined electrons (compare Figure 4.6A & B). Active control was simply implemented by aquiring a V_{qpc1}/V_{qpc2} conductance scan similar to Figure 4.5 at each endpoint of the plunger gate range, choosing optimal QPC gate voltages at each endpoint and linearly interpolating control values for all intermediate plunger gate voltages.

At finite source-drain bias the tunneling DOS shows peaks that are due to both transitions from the $N \rightarrow N+1$ and from the $N+1 \rightarrow N$ electron systems. The complexity of the Coulomb diamond pattern formed by the overlapping tunneling peaks can obscure both transition spectra. As discussed in Section 3.3, asymmetric tuning of the source and drain QPCs changes the respective tunnel rates into and out of the QD. Tuning of the source slightly closed and the drain slightly open serves to increase the relative amplitude of the $N \rightarrow N+1$ transitions with respect to the $N+1 \rightarrow N$ transitions, simplifying the Coulomb diamond resonance pattern. Inspection of the dc current vs gate voltage curves provided the feedback for the QPC tuning. (Figure 4.7). Almost all finite bias measurements reported were made in this slightly asymmetric configuration.

The 2DEG electron temperature can be extracted from the zero-bias Coulomb blockade peak widths using Eqn 3.4, and is plotted for decreasing dilution unit temperature in Figure 4.8. Cooling saturation of the 2DEG temperature at $\sim 50 - 100mK$ is widely observed, and is attributed to the steady-state heating of the 2DEG by radio-frequency radiation transmitted down the wire leads to the device. Construction of an in-line distributed low-pass RC filter on each of the 24 wire sample leads successfully reduced this

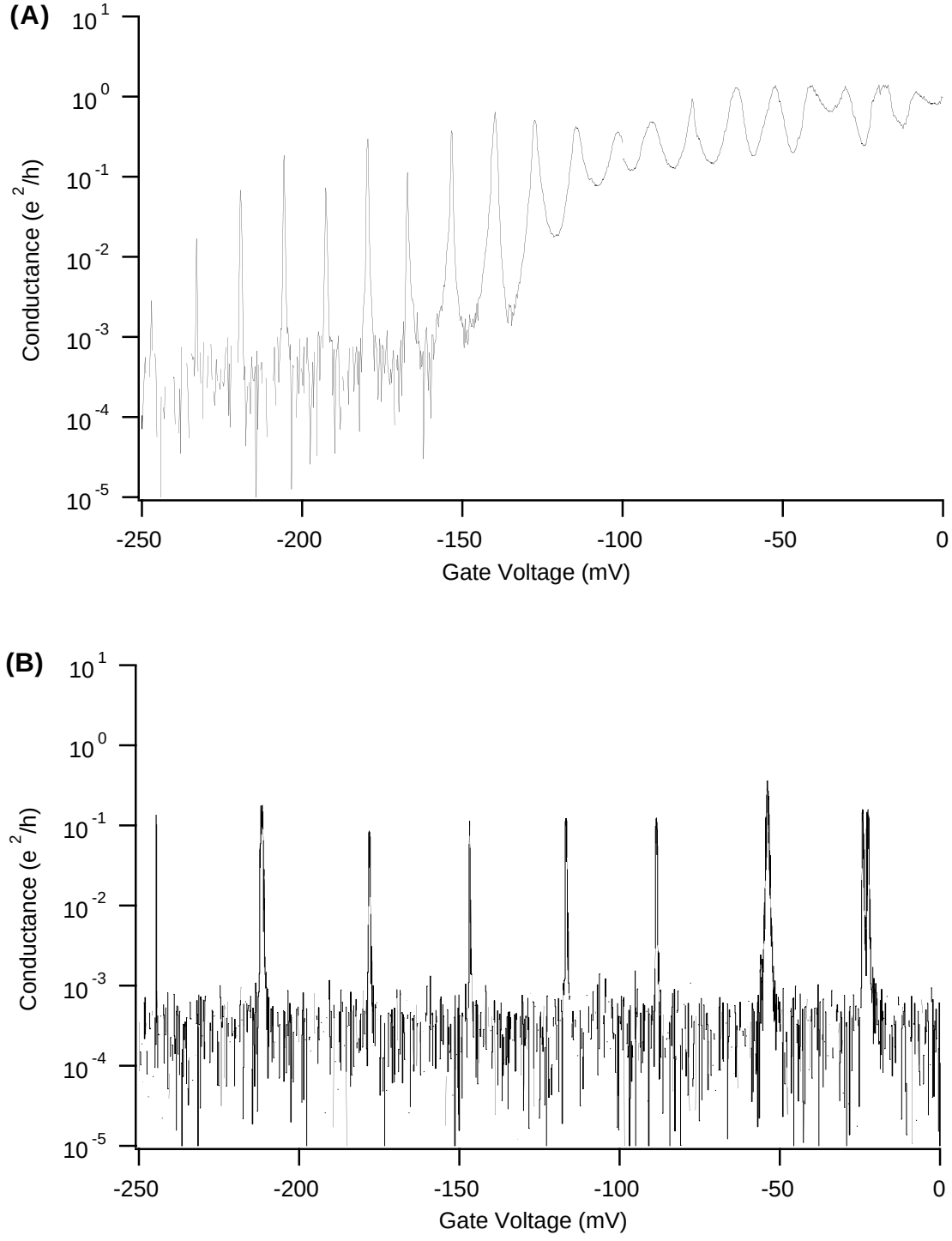

Figure 4.6: (A) The zero bias periodic Coulomb blockade conductance peaks for static QPC voltages. (B) The same zero bias conductance peaks with active modification of QPC voltages to maintain a fixed average conductance.

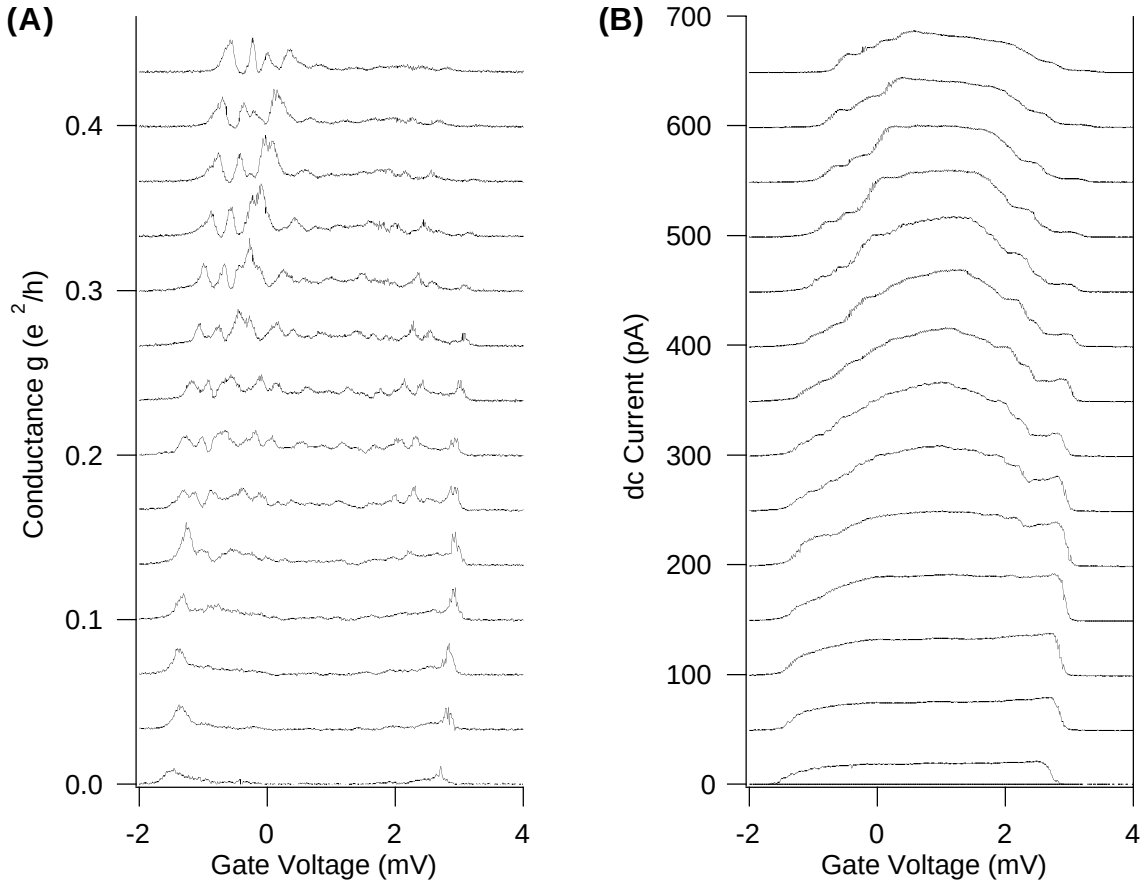

Figure 4.7: (A) Experimental conductance and dc currents (B) for asymetrically tuned QPCs. Top curve is for open source / closed drain QPCs; middle curve is for balanced QPCs; bottom curve is for closed source / open drain QPCs.

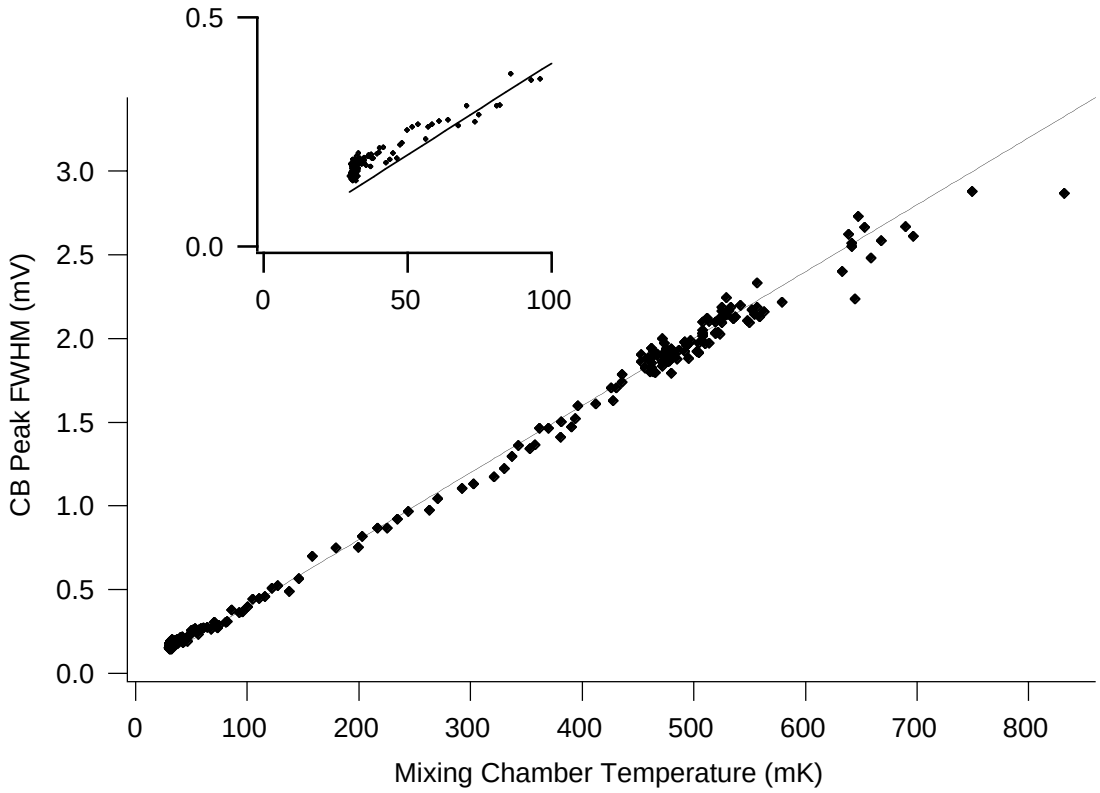

Figure 4.8: Temperature dependence of the Coulomb blockade peak width. (Inset) Slight deviation from the linear relation shows saturation of the 2DEG cooling for mixing chamber temperatures below $\sim$ 50mK.

cooling saturation temperature from $\sim 100mK$ to the reported $\sim 50mK$ [Huibers99]. For maximum spectroscopic resolution of the 0D QD states, all measurements reported here were made at this $50mK$ base temperature.

The majority of the spectral measurements reported use the magnetic field B as a continuous parametric perturbation to the QD tunneling level spectrum. Indeed, it is the unique behavior of each tunneling peak *as a function of* B that identifies a particular 0D quantum state and allows the comparisons and conclusions of this study. The addition of one flux quantum threading the $300nm$ QD occurs at a field of $B \sim 50mT$. Most measurements were conducted in the low magnetic field range of $0 - 300mT$, where the field appears as a small perturbation relative to the kinetic and potential electron energies. At higher magnetic fields above $0.5T$ both the 0D and 2D systems are becoming strongly

perturbed by the Shubnikov-deHaas effect and the quantum Hall effect.

4.5 Device Characterization

The size of the quantum dot and thus both the charging and confinement energies are defined by the lithographic e-beam gate design and by the voltages applied to each of these gates. With an estimated $150nm$ lateral depletion width, the example quantum dot in Figure 4.3 (inset) has an area of $A \sim 0.15\mu m^2$. Using the 2DEG parameters of Table 4.1, the number of electrons confined in the dot is $N \sim 300$ and the average energy spacing of spin-split single-electron levels is $\Delta \sim 24\mu eV$.

Experimentally, the Coulomb charging energy is calculated from the voltage spacing between CB peaks, corrected by the capacitance lever arm of Eqn 3.2. Figure 4.9A shows consecutive zero-bias CB peaks spaced at $\sim 20mV$ and the inset shows a single peak with the fit of Eqn 3.4 to give a $FWHM = 0.43mV$ and a lever arm of $\alpha = 0.035$. The Couloumb charging energy is therefore $E_C \sim 700\mu eV$. The single particle level spacing is measured from the voltage spacing between consecutive resonances in the broadened finite-bias CB peak, with care taken to identify successive resonances that both correspond to the $N \rightarrow N+1$ transition. Figure 4.9B shows the same CB peaks now at finite source-drain bias. The average spacing between excited state resonances is $\sim 1mV$ and using the same lever arm $\Delta \sim 35\mu eV$.

The estimated Fermi energy of $7meV$ divided by the measured single particle (spin-split, see Section 5.4.2) energy $\Delta \sim 35\mu eV$ yields $N \sim 200$, in reasonable agreement with the area/density estimate.

Finally, high magnetic field measurements (presented in Section 6.5) show that the density inside the QD is actually $n_s \sim 6\text{x}10^{10}cm^{-2}$. This revises our electron number estimate downwards to $N \sim 95$, and also indicates that the QD may be defined by electrostatically "softer" walls (ie lower slope $\partial E/\partial x$) that yield a reduced Fermi energy inside the QD [Kumar90, Stopa93].

Estimated areas, electron numbers and measured charging energies and single particle level spacings are given in Table 4.2 for the four different quantum dot devices studied in this work.

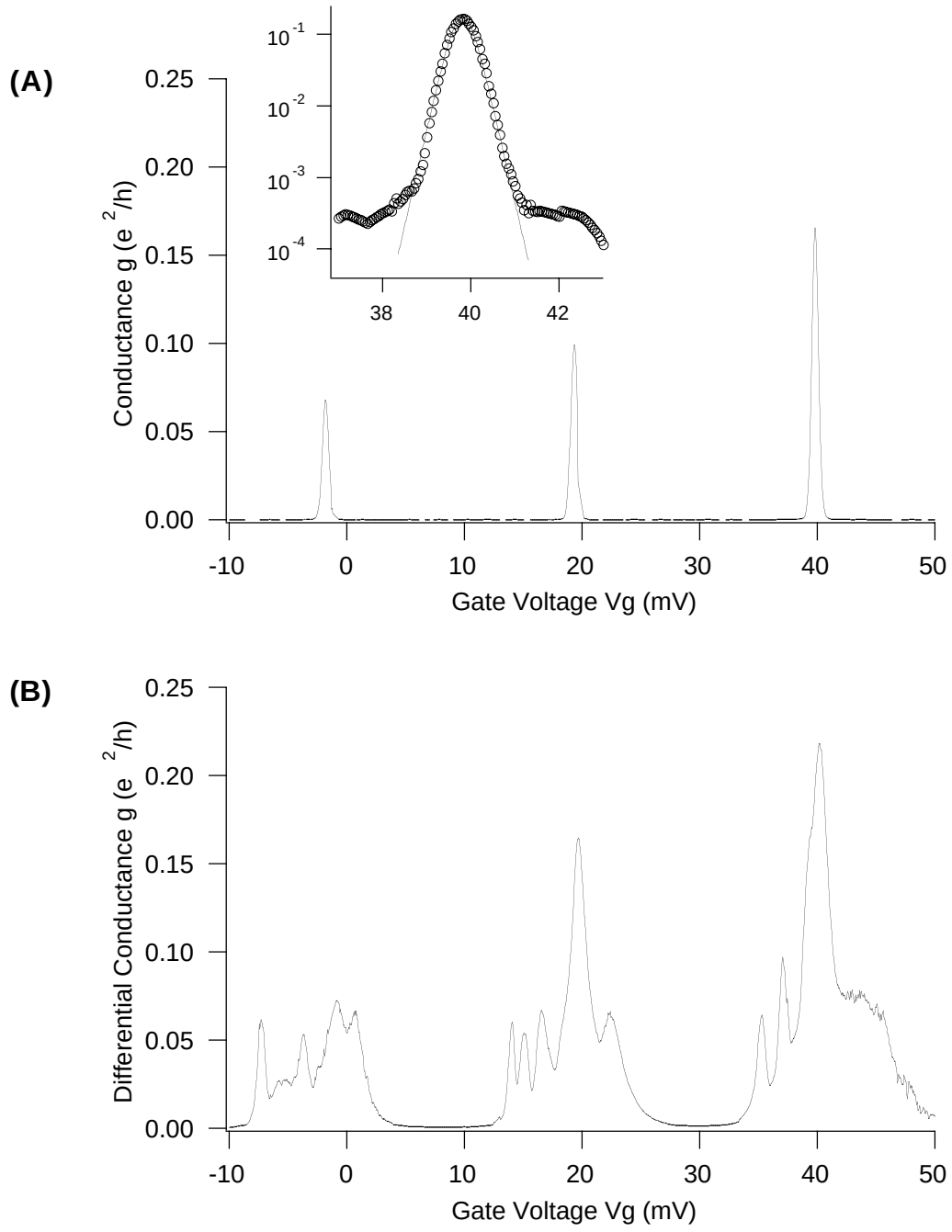

Figure 4.9: (A) Zero bias periodic CB conductance resonances. (Inset) A fit of Eqn 3.4 to one CB resonance. (B) At finite bias each single peak is broadened into a set of resonances.

Device	Area (μm^2)	N	$E_C(\mu eV)$	$\Delta(\mu eV)$	$E_{spin}(\mu eV)$
1	0.19	380	700	35	40
2	0.15	300	700	40	35
3	0.15	300	1000	55	35
4	0.30	600	600	25	not visible

Table 4.2: Estimated parameters of the four quantum dot devices measured. Area is estimated from lithographic design, N is calculated directly from the area A and 2DEG density n_s, E_C, Δ and E_{spin} are measured from the ground and excited state spectra.

Chapter 5

Ground state measurements

5.1 Introduction

Our investigation of the QD energy spectrum is divided into three parts; we first characterize and analyze properties of the ground state transitions in this chapter, then follow with measurement and analysis of the excited states in Chapter 6, and finally compare and correlate the ground states with the excited states in Chapter 7. In all cases we are looking for evidence of behavior predicted by either single-particle or many-body theory. As suggested in the statement of the problem in Chapter 1, this will be achieved by comparison of the measured spectrum for N electrons with the measured spectrum for $N+1$ electrons. The effect on the QD spectrum of adding a single-electron is perhaps the most direct test differentiating single-particle and many-body behavior.

Comparison of the N and $N+1$ spectra requires a method of identifying individual conductance peaks and tracking their changes as electrons are added to the QD. We will see that the parametric dependence of peak height and position on magnetic field can be used to uniquely identify each quantum state of the QD. This idea is the foundation for all the spectral analysis conducted here.

5.2 Ground state "fingerprints'

At infinitesimal source-drain bias and low temperature all tunneling through the QD occurs via transitions between the N and $N+1$ ground states. An electron entering from the source tunnels into the single quantum level that is the $N+1$ ground state. The electron

tunnels out of this state to the drain and the cycle repeats to allow current flow, as long as the gate voltage remains biased at the $N, N+1$ degeneracy point (recall Section 3.4.2). The position and height of the single, sharp CB conductance peak are characteristic of the particular $N+1$ ground state eigenenergy and eigenfunction coupling respectively. Fluctuations in peak position reflect changes in the eigenenergy of this state. Fluctuations in peak amplitude reflect changes in QD coupling to the source and drain leads and hence changes to the wavefunction within the QD.

We use a magnetic field to continuously perturb the confining potential of the QD electrons and thus continuously change their energies and wavefunctions. A magnetic field perturbation to the single-electron Hamiltonian is well understood theoretically, and provides an accessible experimental tool to effect controlled change within the QD system. The fluctuation of each eigenfunction with applied magnetic field is in general unique; particularly in the low field regime and with a chaotic cavity boundary different eigenfunctions will have different parametric magnetic field dependencies. This assumption is less true for symmetric cavity boundaries or high fields where either accidental or magnetic field imposed symmetries cause many states to have similar parametric dependencies. In this work we attempt to confine measurements to both low magnetic fields and QDs with chaotic cavity boundaries.

Figure 5.1A shows a single CB peak measured at low temperature $kT \sim 100mK$ and infinitesimal bias $V_{ac} \sim 5\mu V = 50mK$, as a function of the continuously varied perpendicular magnetic field $B = -200mT \rightarrow +500mT$. A greyscale image representation of the same data is shown in Figure 5.1B. The CB conductance peak is seen to fluctuate apparently randomly in both position on the gate voltage axis and in maximum amplitude on the conductance axis. The gate voltage axis, if rotated 90^o clockwise, becomes an energy axis for the QD spectrum. The conductance amplitude is the QD wavefunction coupling to source and drain. These two fluctuations are symmetric about $B = 0$ and repeatable, confirming that the magnetic field is indeed parametrically changing the $N+1$ quantum ground state energy and wavefunction.

The zero-bias CB peaks occur quasi-periodically in gate voltage. The $N+1, N+2$ degeneracy point will occur at a gate voltage approximately E_C more positive than the $N, N+1$ degeneracy point. We repeat the magnetic field sweep for this and several other adjacent CB conductance peaks. Six peaks labeled $N-3$ to $N+2$ are shown in Figure 5.2, where the peak labeled "N" corresponds to the degeneracy between electron numbers N

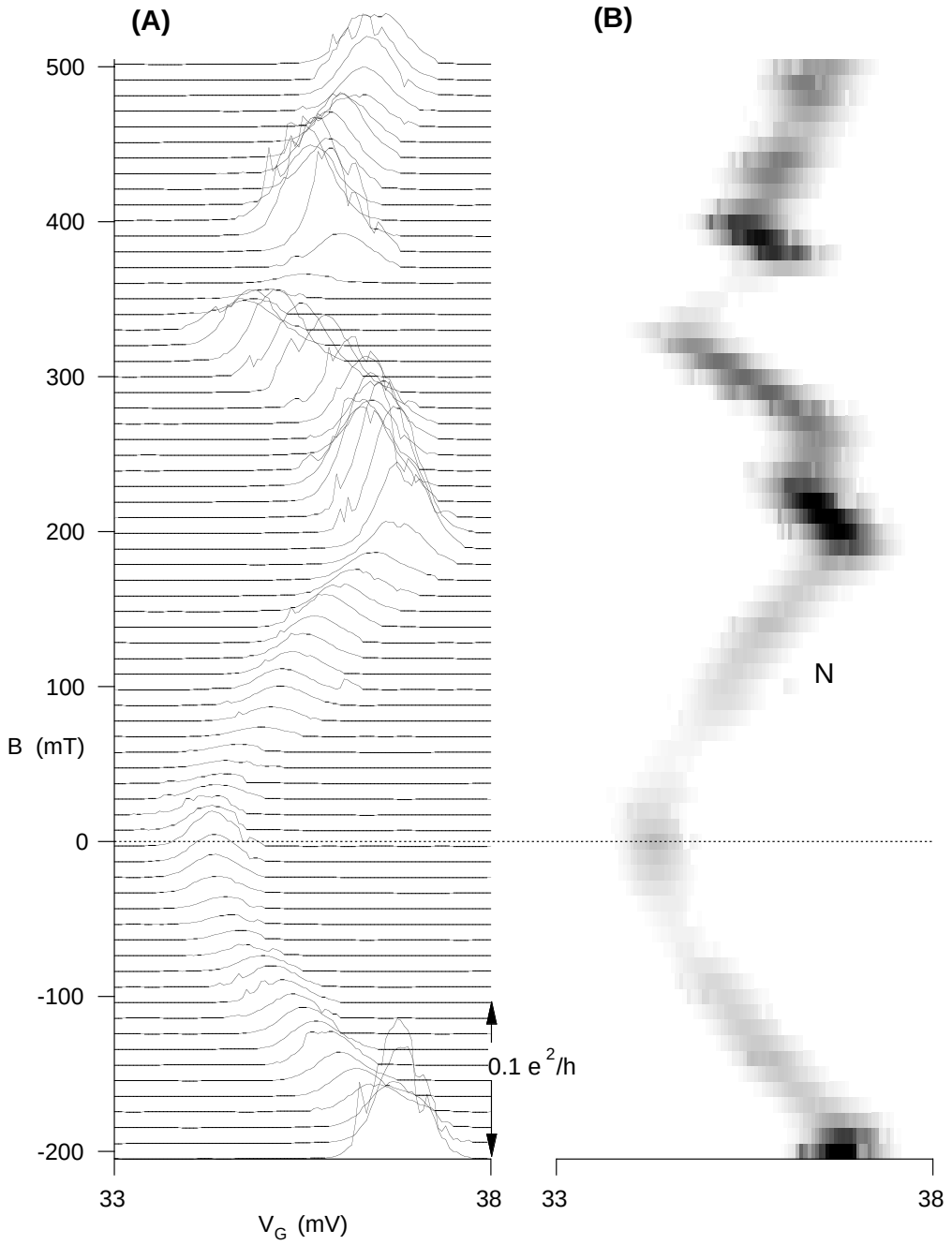

Figure 5.1: (A) Raw data showing parametric evolution of ground state CB resonance with applied magnetic field B. Note that both the peak center position and peak amplitude are fluctuating symmetrically about $B = 0$. (B) Grey scale image of the same data set. Black is high conductance ($0.1\ e^2/h$), white is low conductance.

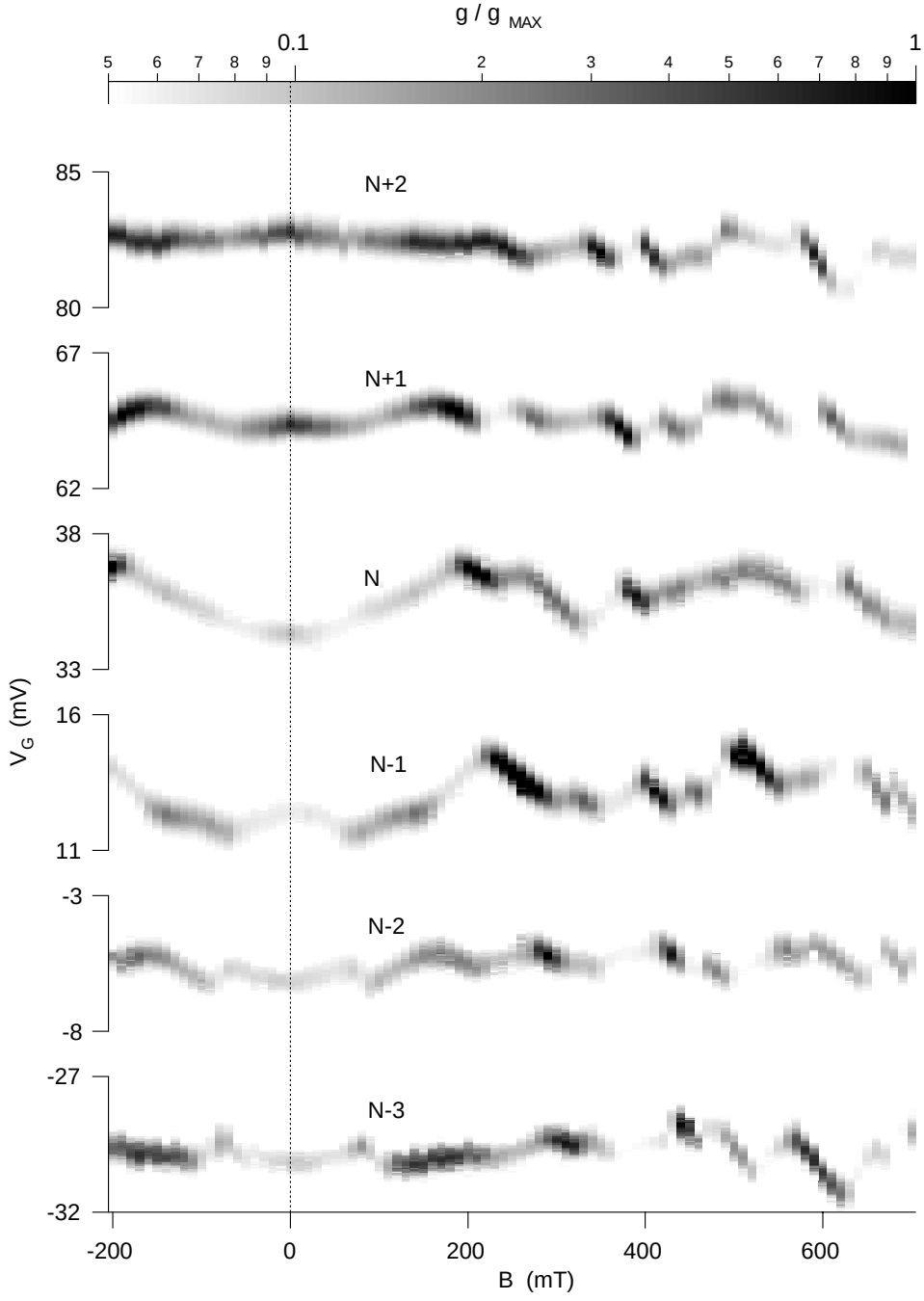

Figure 5.2: Six successive ground state fingerprints for Device 1, where conductance is indicated as a grey scale at the top of the figure. The x axis is now magentic field and the y axis is gate voltage. In this orientation, more positive gate voltages correspond to higher dot energies, thus the y axis is also an energy axis.

and $N-1$. The data of Figure 5.1 is now rotated 90^o clockwise so that the vertical axis corresponds directly to energy. The continuous evolution of each peak energy and amplitude with B field yields a distinct signature or 'fingerprint" for each quantum level. We note that each successive ground state has a different and unique fingerprint of energy and amplitude fluctuations, indicating that each ground state is a different quantum wavefunction. The data of Figure 5.2 is from Device 1.

5.3 Assembled Ground State Spectra

We return to the ground states of Device 1, reproduced in Figure 5.3A. In Figure 5.3B we collapse this group of six levels, originally separated by E_C, by shifting each level in energy (gate voltage) until they best align with adjacent levels [McEuen91;McEuen92]. By doing so we assume a Coulomb interaction independent of B. Such translation of the ground states produces a recognizable spectrum coherent over many levels, in which the fluctuations of peak amplitude and energy are visible as anticrossing of neighboring levels. The specific signature of each anticrossing is that two successive levels appear to trade both conductances and velocities $\partial E/\partial B$ as they pass through their point of closest approach [Takami92]. The assembled spectrum of fluctuating ground states appears to be composed of slowly varying wavefunctions as followed through anticrossings, slightly perturbed into the measured anticrossed level structure. We measure the average single particle level spacing Δ from this assembled spectrum as the average energy separation between ground state center positions. Additionally, note that several wavefunctions evolve smoothly across all six ground states, for example the downward sloping, high amplitude peaks between $B = 200 - 300mT$ and also $B = 350 - 450mT$. Also, although successive ground states are not parallel over any appreciable magnetic field scale, some of the slowly varying wavefunctions as followed through the anticrossings do appear paired. In particular, the downward sloping $B = 200 - 300mT$ paired lines and the downward sloping $B = 350 - 450mT$ lines appear parallel over their visible range. Other slowly varying wavefunctions, for example the concave-down parabola between $B = -100, +100mT$, do not have any visible parallel paired state.

This collapsing of ground states can be repeated for the other sets of measured ground states. In Figure 5.4A we show the 10 separated ground states measured on Device 2; part (B) collapses these levels until they best align with their neighbors. Here again the

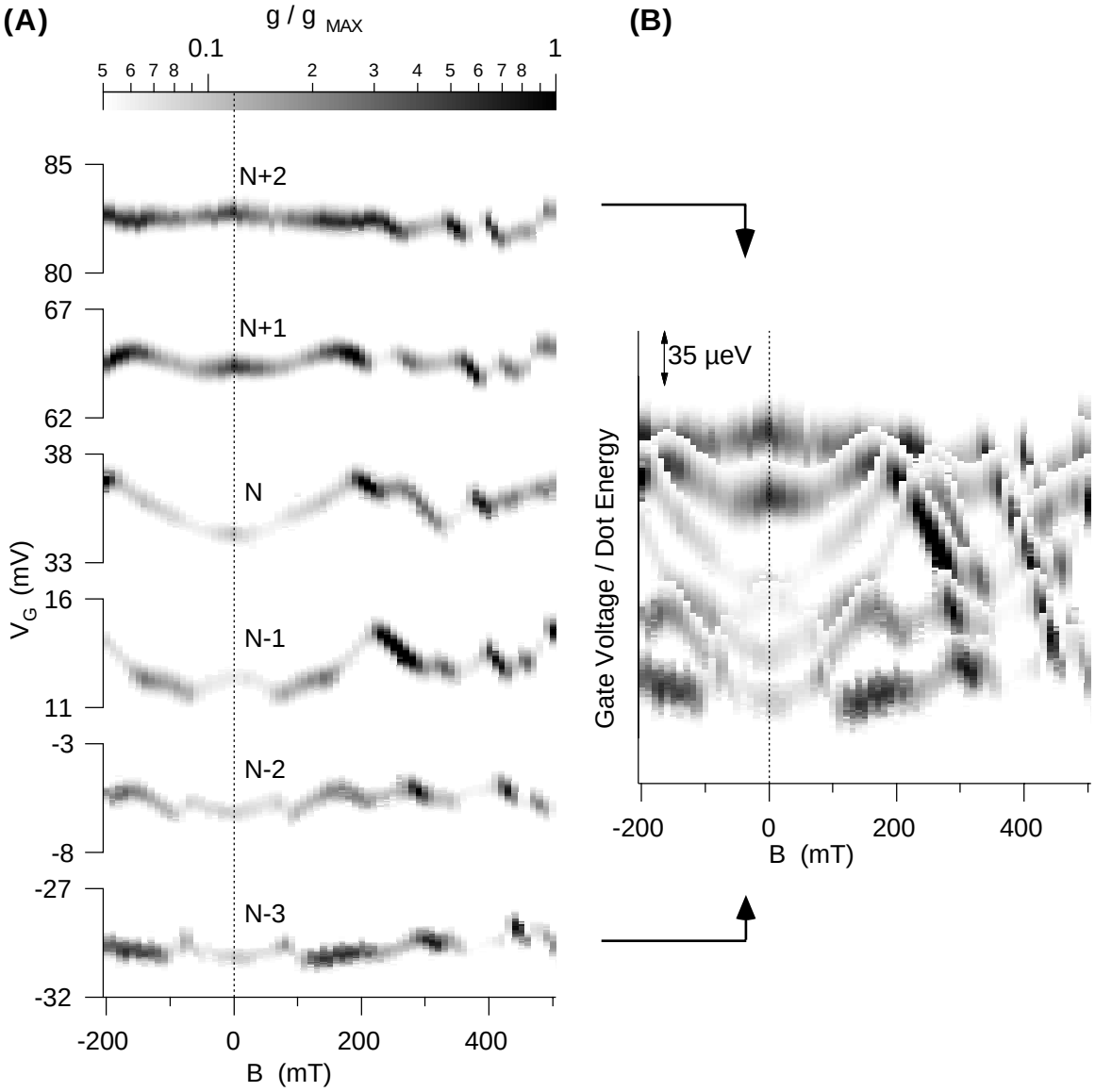

Figure 5.3: (A) The six successive ground states of Device 1. (B) The six ground states are squeezed together vertically like an accordion to produce an "assembled ground state spectrum". The position and amplitude fluctuations of successive states are seen to fit together coherently.

spectrum produced appears to be composed of slowly varying wavefunctions as followed through anticrossings, perturbed into the measured anticrossed spectrum.

Figure 5.5 shows the successive ground states of Device 3 separated and then collapsed together. Figure 5.6 shows data from Device 4.

Finally, the label "anticrossing" should be clarified: in the ground state context we use the description above of two successive ground states appearing to trade both conductances and velocities $\partial E/\partial B$ as they pass through their point of closest approach. The point of closest approach in this case however is still separated by a charging energy E_C. After removing the charging energy spacing and constructing the collapsed ground state spectrum, many of the adjacent states overlap at these anticrossing points. The distinction between an anticrossing and a true crossing is the minimum distance between eigenvalues; in our case thermal smearing of the conductance peaks and discrete B field sampling prevents this distinction being made for those "anticrossings" whose minimum separation is comparable to the thermal CB peak width. We return to this issue in Section 6.2 during analysis of excited state behavior.

We also discuss briefly two features visible in the ground state data but not directly related to our central single-particle/many-body question. The individual ground states of Figure 5.6 in particular show a "weak localization" type suppression of the $B = 0$ conductance and an adiabatic demagnitization/magnetization of the sample temperature as measured by CB peak height and width.

Weak localization is a well characterized effect in open quantum systems, and results from enhanced back scattering by time-reversed trajectory pairs [Beenakker91b; Huibers98]. Application of a magnetic field breaks this time-reversal symmetry and removes the back scattering enhancement, increasing the total conductance of the system. While this phenomenom is understood theoretically in open systems, it has not been addressed in closed quantum systems such as our isolated QDs. The data of Figure 5.6 shows many CB peaks with suppressed amplitudes near $B = 0$. Figure 5.7 shows the average conductance for the ground state data of Device 4, with the observed weak localization dip at $B = 0$. This issue deserves detailed study, but will not be addressed further in this work.

Adiabatic magnetization and demagnetization was first observed in our samples after modifications to the dilution refrigerator wiring allowed sample cooling to $\sim 50mK$. This effect is visible in the data of Figure 5.5, Figure 5.6 and Figure 5.7; note that for small magnetic fields $B < 50mT$ the peak heights and widths show a distinct asymmetry about $B = 0$.

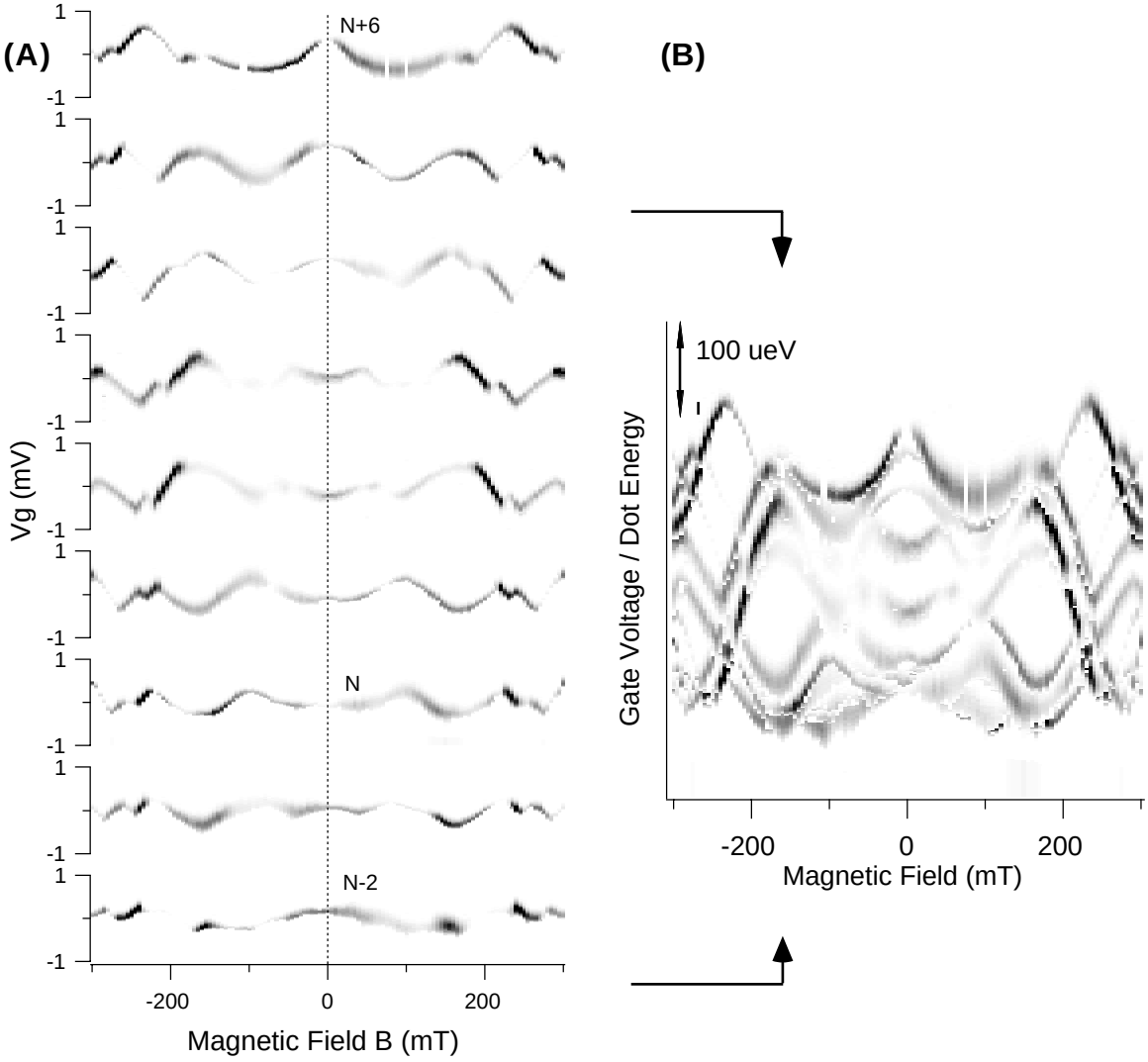

Figure 5.4: (A) The nine successive measured ground states of Device 2. (B) The assembled ground state spectrum. Conductance grey scale is $\sim 0 \rightarrow 0.1e^2/h$.

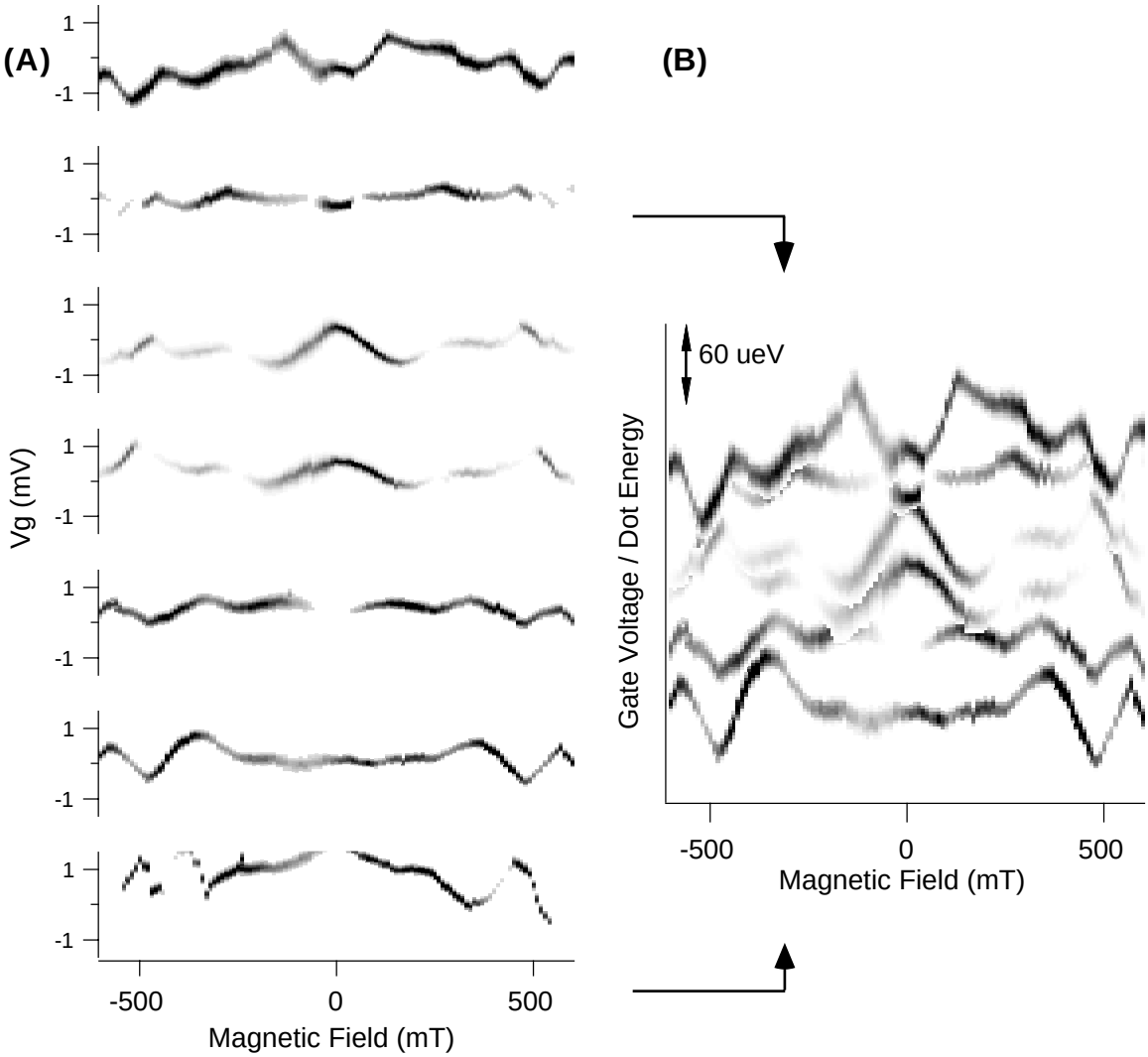

Figure 5.5: (A) The seven successive ground states of Device 3. Note the similarity of the third and fourth traces from the top. (B) The assembled ground state spectrum. Conductance grey scale is $\sim 0 \rightarrow 0.1e^2/h$.

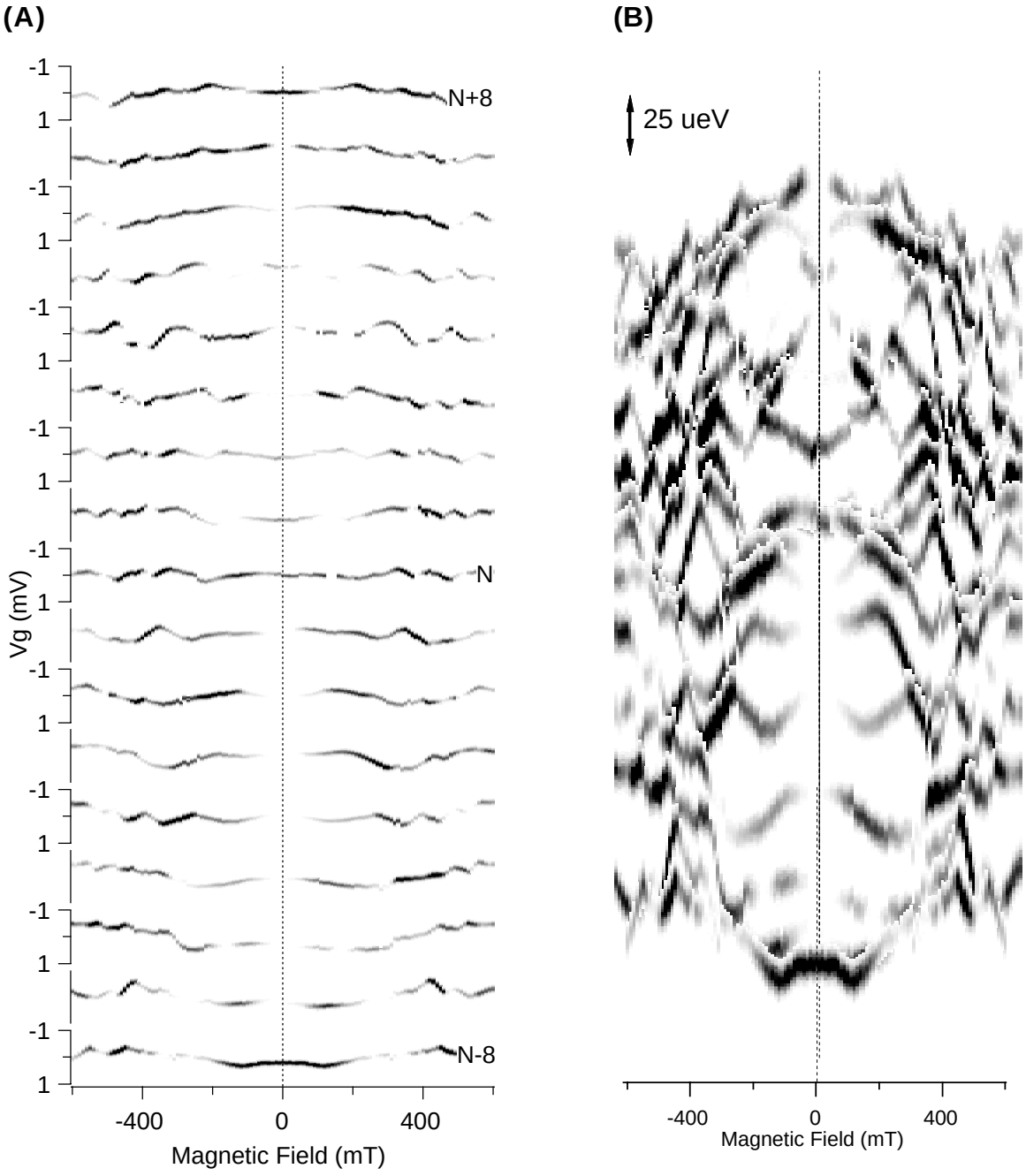

Figure 5.6: (A) The seventeen successive measured ground states of Device 4. (B) The assembled ground state spectrum. Note the poor alignment between many fluctuating features of successive states. Conductance grey scale is $\sim 0 \rightarrow 0.1e^2/h$.

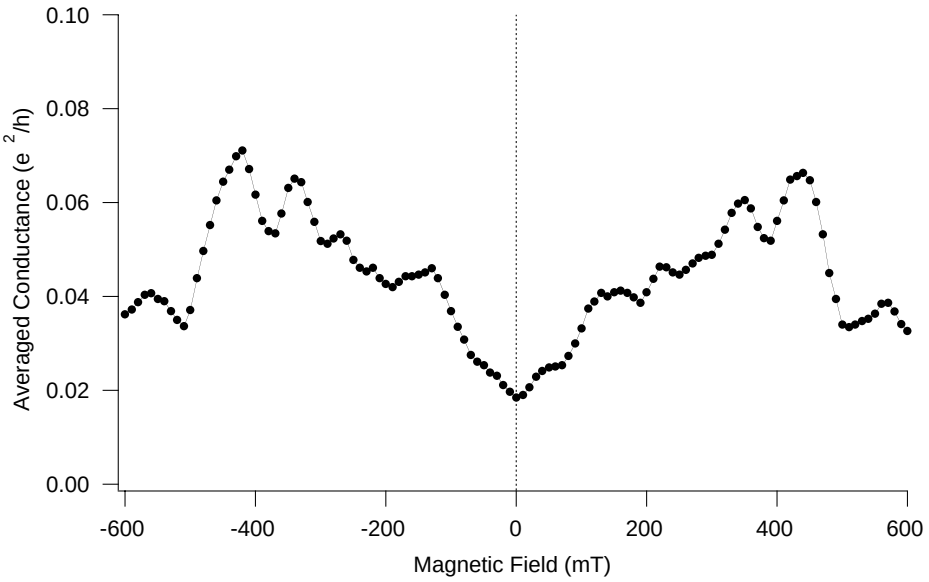

Figure 5.7: Averaged ground state amplitude as a function of field B for the data of Figure 5.6. A dip in average conductance similar is observed at $B = 0$.

This asymmetry can be characterized as a narrowing of the peak width and increase in peak height as the B field is swept towards zero, followed by a rapid broadening of peak width and decrease in peak height as the B field passes through zero and increases in absolute magnitude on the far side of $B = 0$. This is a non-equilibrium effect dependent on initial conditions and magnetic field sweep rate. It is not dependent on initial B field polarity, only on absolute field magnitudes and sweep rates. To interpret this anomalous behavior, recall that the CB peak width is a direct measure of the 2DEG temperature. Fitting the peak width to Eqn 3.4 yields this temperature. Figure 5.8 shows a width/temperature curve averaged over the seven ground state measurements of Figure 5.5. The magnetic field for these measurements was swept at a fixed rate of $10mT$ steps every 2.5 minutes. This type of temperature change controlled by magnetic field is known as adiabatic magnetization, and is typical of Fermionic systems with a discrete but degenerate system of levels at the Fermi energy that can be readily split by an applied magnetic field. The adiabatic demagnetization of paramagnetic salts or nuclei is in fact a valuable low temperature cooling technique. Several possible candidates within our sample exist, including the nickel atoms alloyed into the GaAs/AlGaAs to form ohmic contacts, the silicon donor atoms within the AlGaAs or perhaps the spin-polarizable electrons of the 2DEG itself. This issue also deserves more

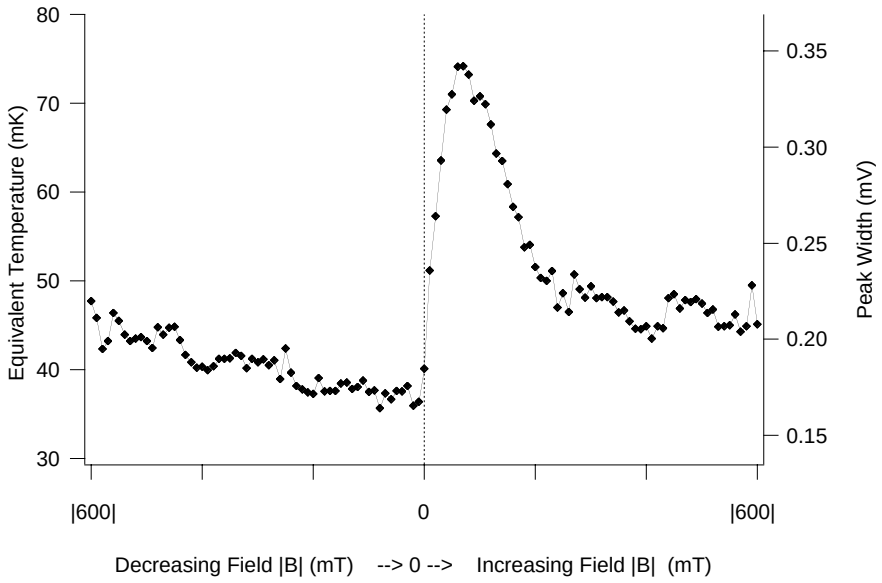

Figure 5.8: Averaged ground state peak width and equivalent 2DEG temperature as a function of magnetic field magnitude and sweep direction for the data of Figure 5.6. Absolute magnetic field amplitude is decreasing from 600mT to 0mT, then increasing from 0mT to 600mT. Adiabatic demagnetization occurs as the field is swept towards zero and the sample cools; adiabatic magnetization is evidenced by the rapid heating as the field passes through zero and is swept to higher absolute magnitude.

study but will not be addressed further in this work.

5.4 Connection to Single-Particle and Many-Body Theory

5.4.1 Single-Particle Behavior

Much of the QD behavior characterized in Section 5.3 can be understood within the single-particle model. Each ground state was shown to have a unique fingerprint of parametric energy and coupling amplitude fluctuations. This fits the picture of a ladder of single-particle states, each a different eigenfunction with a unique B field dependence. Much more significantly, the fluctuations of adjacent states fit together coherently when the spectrum was collapsed together. These fluctuations were then identified as anticrossings between the adjacent states, with exchange of conductance amplitude and level velocities $\partial E/\partial B$ at a well defined point in B. The precision of this anticrossing exchange can be explained directly as the sequential filling of a fixed single-particle spectrum, with the ad hoc addition of a classical charging energy between successive electron number ground states. This same fixed spectrum picture accounts for the smooth evolution of wavefunctions through anticrossings across all six ground states.

5.4.2 Evidence of Many-Body Interactions

Each quantum level of the QD is expected to be spin degenerate. In the single-particle model this would show as a ladder of paired parametric fingerprints, not as the different and unique fingerprints reported in Section 5.3 . Different fingerprints imply directly that the spin 1/2 degeneracy of the electrons has been lifted – spin pairs of eigenstates are somehow separated in energy and not obviously visible in the ground state spectrum. In order to disrupt the trivial pairing of successive states, the spin splitting must be of order or greater than the level spacing Δ. This spin degeneracy can be lifted in three ways, due to a field dependent Zeeman shift, due to a static spin-orbit interaction in the GaAs 2DEG or due to electron-electron interactions within the confined QD. These are discussed in more detail in Section 6.6.2 . Here we note that the splitting appears much larger than the typical Zeeman energy scale, but perhaps comparable to the GaAs/AlGaAs spin-orbit energy scales. We suggest however that as in atomic orbitals, the electron-electron exchange interactions lift the spin degeneracy of the QD levels. Dividing the interaction into direct, exchange and

correlation terms as in Section 2.2, a minimum mechanism for splitting requires either the direct or exchange interactions modify the energy necessary to add a second electron into a singly filled orbital.

The magnitude of the spin splitting can be estimated from the collapsed spectra in Section 5.3 . We return to Figure 5.3B and examine the vertical energy spacing between the paired, downward sloping dark lines between $B = 200 - 300mT$ and also $B = 350 - 450mT$. We interpret these paired lines as spin paired wavefunctions descending parametrically in energy as B increases, and take the vertical energy spacing between them as the magnitude of spin splitting in the QD. From Figure 5.3B, this spin splitting magnitude is roughly equal for the two pairs identified and is approximately $E_{splitting} \sim 40\mu eV$. Recall the level spacing $\Delta \sim 35\mu eV$ for this Device 1. Spin splittings are estimated for each of the QDs measured and listed in Table 4.2.

Finally, we point out that not all ground state anticrossings match up with adjacent levels exactly. In the collapsed spectrum of Figure 5.4B, anticrossings at high $B > 200mT$ are aligned very well. Anticrossings at lower $B < 200mT$ however, often show a misalignment in energy or B field. Improved alignment at low B can be achieved by shifting individual states differently in energy, yet this immediately decreases the quality of the anticrossing matching at high B. Thus despite the surprisingly good alignment obtained for all Devices, the collapsed spectra contain discontinuities that would not be present in a single-particle spectrum. These discontinuities indicate that some changes in both ground state energies and wavefunctions are indeed occuring as electrons are added to the QD; the spectrum is not simply a fixed single-particle ladder of sequentially filled states. We discuss variations between Devices in more detail in Section 6.6.3.

Chapter 6

Excited State Measurements

6.1 Introduction

The measurements of the ground states access the QD spectrum one successive level at a time. When collapsed together they yield a picture of the spectrum assembled from individual levels measured at different electron numbers. In contrast, measurements of the excited states allow simultaneous access to several levels while at the same electron number. The available levels are all within a small energy window centered on the QD Fermi level, with a width determined by the applied source-drain bias.

We continue to look for evidence of single-particle or many-body behavior by comparing the measured spectra for N electrons with the measured spectra for $N+1, N+2, \ldots$ electrons. The excited state measurements are a more powerful method to effect this comparison however, since at each electron number overlapping segments of the QD spectrum can be characterized. The parametric dependence of conductance peak height and energy on magnetic field is again used to identify each quantum state of the QD, except now both the ground states and the excited states are available for this analysis.

We present the experimental data from each Device in Section 6.3, continue in Section 6.4 with a more detailed discussion of spin pairing based on the excited states evidence, briefly describe the appearance of negative differential conductance in Section 6.5 and then return to connect the excited states data to the single-particle and many-body models of the QD spectrum in Section 6.6 .

6.2 Tunnel Spectroscopy of Excited States

The tunnel spectroscopy of excited QD states is significantly more difficult to interpret than the spectroscopy of the ground states. At finite bias multiple QD states are available for transport and the transitions allowed may be between any two ground or excited states of the N and $N+1$ electron systems. The pattern of excited state resonances in the Coulomb diamond measurement can be complex enough to make identification of individual resonances impractical. For this reason, we employ several of the experimental techniques suggested in Section 3.3 and Section 4.3 to simplify the measured excitation spectrum. These are: increased isolation of the QD to help validate the complete relaxation assumption, selection of either postive or negative bias depending on Coulomb diamond angle to give enhanced source resonances, and slight asymmetric tuning of the two QPCs to further enhance the source resonances. The result of these techniques is a measured spectrum very sensitive to electrons tunneling from the source into the unoccupied QD states above the $N+1$ ground state. If the complete relaxation hypothesis holds, then these measured resonances will be transitions from the N ground state to the successive $N+1$ excited states.

Figure 6.1 shows a typical experimental measurement of QD differential conductance as a function of gate voltage V_g and drain-source voltage V_{DS}. At $V_{DS} = 0$ the familiar ground state CB peaks are visible, roughly equally spaced in V_g. At finite bias the sharp, zero bias CB peaks have broadened into multiple peak clusters enclosing the Coulomb diamonds. As described in Section 3.3, for positive V_{DS} the differential conductance peaks forming dark stripes parallel to the negative slope Coulomb diamond edge are successive unoccupied QD levels in resonance with the source Fermi level; exactly the resonances we have tuned the system to maximize. We fix the source-drain bias at a value that is ~ 15 times the single-particle level spacing Δ, but still smaller than the charging energy E_C that would allow two electron tunneling. This is at $V_{DS} = 0.6mV \sim 0.6E_C$.

A single gate voltage trace at this source-drain bias $V_{DS} = 0.57mV$ is shown in Figure 6.1B. The dark stripes of panel A are visible as multiple resonances on the left edge of each broadened CB peak. Each broadened CB peak shows a tall peak with one, two, three or four smaller peaks to its left. Counting from the left edge of each broadened peak, we identify the tall peak as the first, second, third or fourth excited state resonance of the $N+3, N+2, N+1$ or N-electron system respectively. The shift of the distinctive tall peak by one position in each successive excitation spectrum suggests that the particular electron

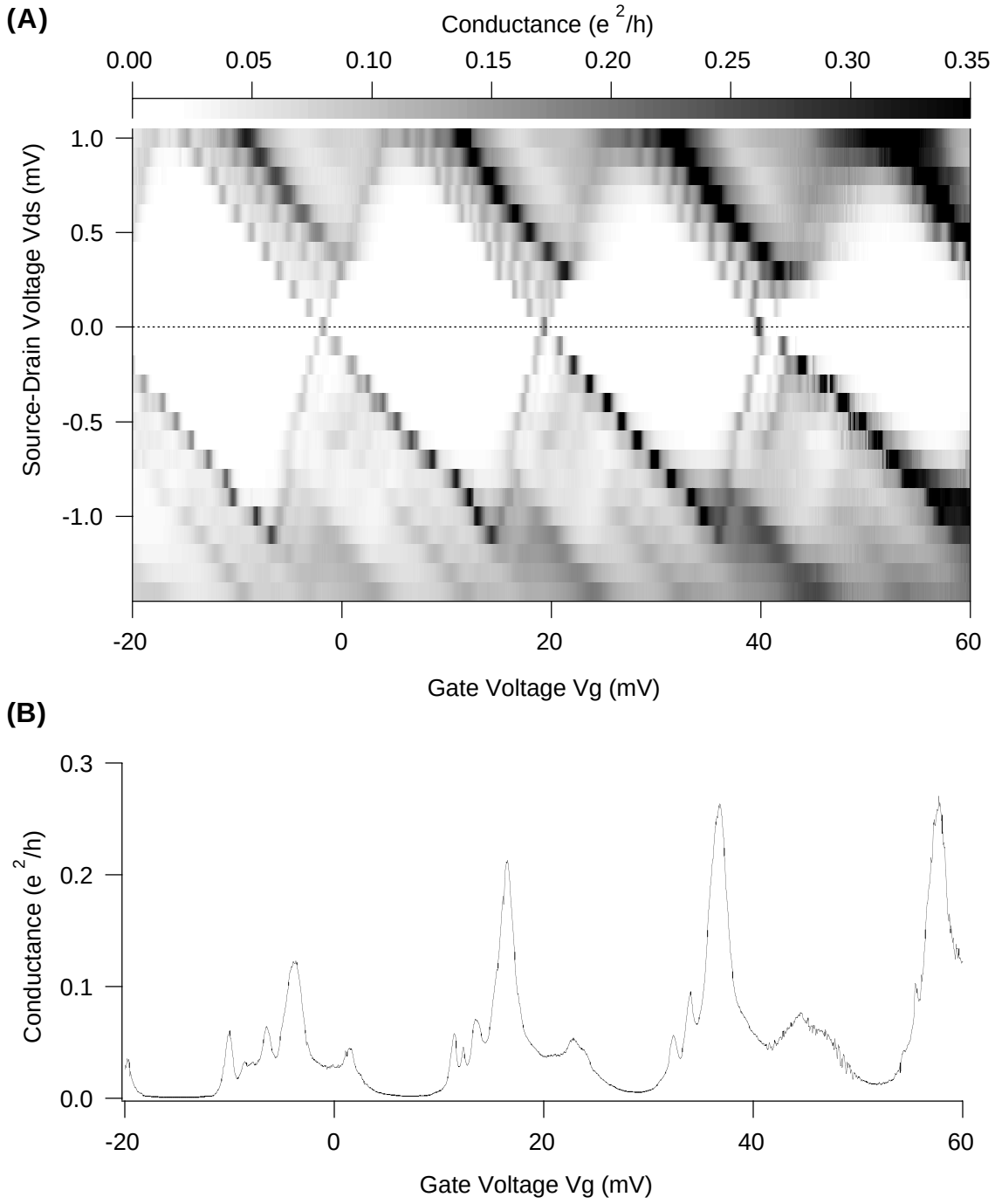

Figure 6.1: (A) Experimental Coulomb diamond measurement. (B) A single trace from (A) at $V_{ds} = 0.6mV$ showing multiple excited state resonances within each broadened CB peak.

wavefunction associated with this tall peak and indeed the visible level structure of the QD are only weakly perturbed as electrons are added one by one.

6.3 Excitation Spectra Correlations

To further characterize the excited state spectrum we follow the parametric evolution of individual resonances with applied magnetic field. This is exactly the same method used for the ground state measurements, except that now we wish to characterize all of the simultaneously visible excited state resonances. At the fixed source-drain bias selected above, we scan the gate voltage repeatedly across the full width of the broadened CB peak while slowly incrementing the magnetic field.

Figure 6.2A shows one finite-bias CB peak measured for magnetic fields $B = -200 \rightarrow +500mT$ and $V_{DS} = 0.3mV$. The $N+1$ ground state is the first peak at either edge of the cluster. Excited $N+1$ states are counted successively inward from the right edge. At different magnetic fields between 3 and 5 excited state resonances are visible. As with the ground states, each tunneling resonance evolves in both position and amplitude yielding the distinct fingerprint of each quantum level. Collectively the pattern of resonance evolution provides a distinct fingerprint for the excitation spectrum of the $N+1$ electron system. This is exactly a fingerprint of the QD tunneling DOS within a small energy window above the QD Fermi level. Panel B displays the same data in a greyscale format. Figure 6.3 displays three consecutive finite bias CB peaks, where the data of Figure 6.2, labeled peak $N+1$, has now been rotated 90^o clockwise to transform the gate voltage axis into a vertical energy scale.

The main result of the entire spectroscopy study is visible in this set of three consecutive excitation measurements of Figure 6.3 – it is the remarkable similarity between the QD spectra for the $N, N+1$ and $N+2$ electron systems. The QD spectrum appears to be essentially unperturbed by the addition of an electron, changing only slightly from N to $N+1$ to $N+2$ electrons. Close inspection shows a direct correlation between the consecutive spectra; the $N+1$ spectra is very similar to the $N+2$ spectra except for the addition of one new resonance at the bottom of the spectrum, forming the new $N+1$ ground state. Similarly, addition of one new resonance to the bottom of the measured $N+1$ spectrum appears to yield the N spectrum. In each case, the other features of the spectrum shift upwards, so that the ground state of $N+1$ becomes the 1st excited state of N, the 1st

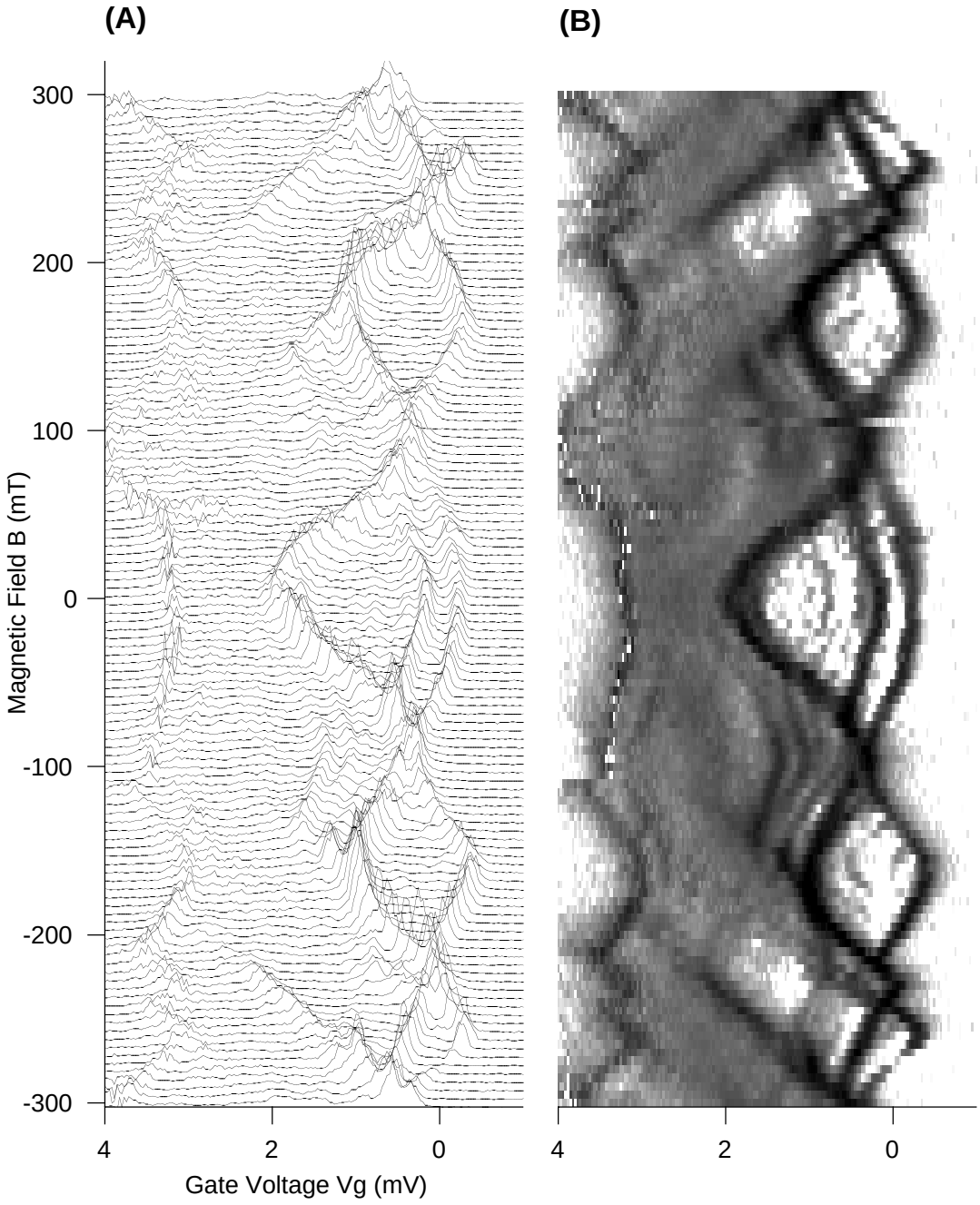

Figure 6.2: (A) Raw conductance data at finite bias, with gate voltage and amplitude fluctuations symmetric about $B = 0$. (B) Greyscale image of the data from (A), forming the excited state "fingerprint."

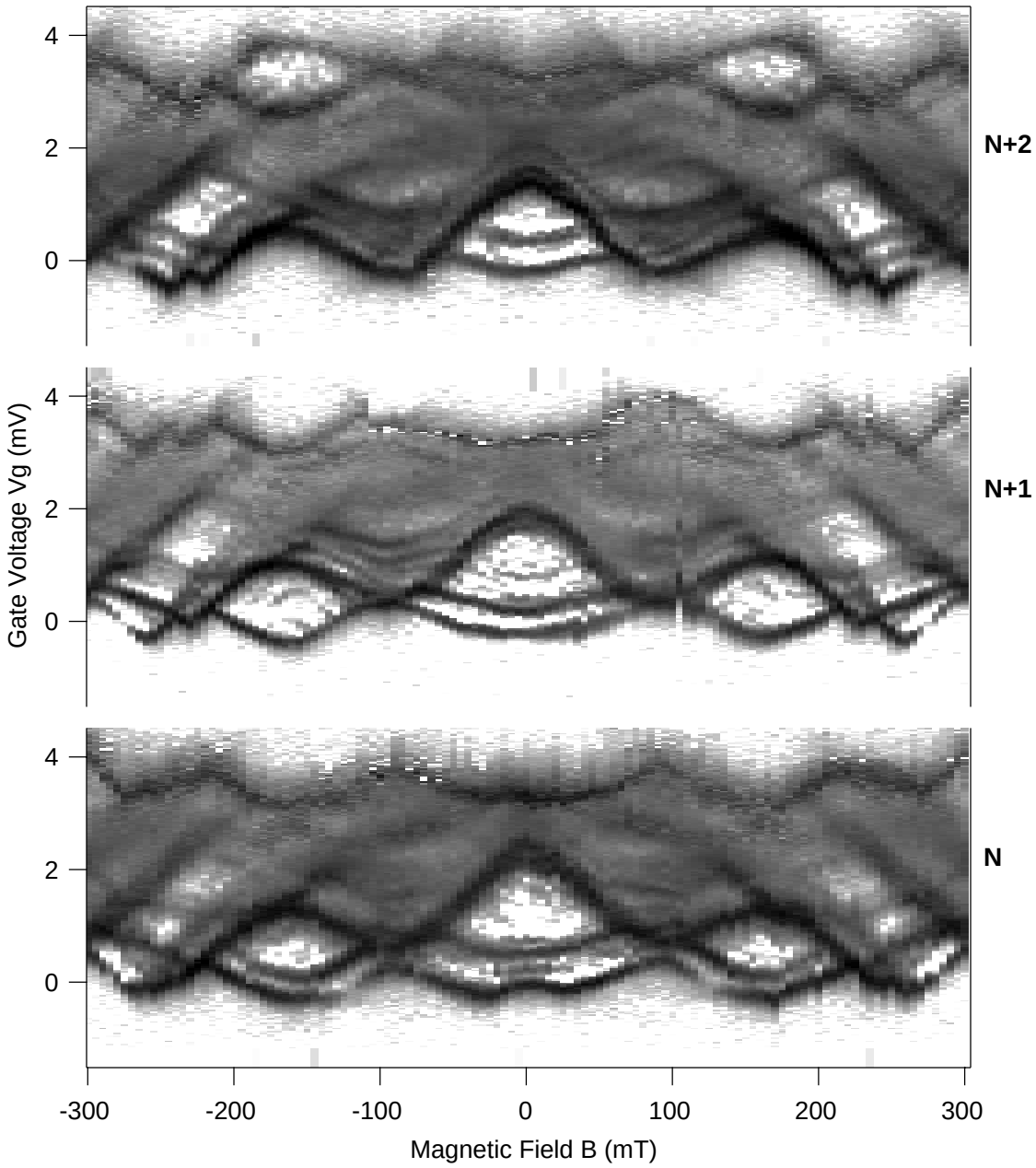

Figure 6.3: Three successive excited state fingerprints from Device 2. Note the remarkable similarity between successive spectra. Also compare to ground states of Figure 5.4

excited resonance of $N+1$ becomes the 2nd excited resonance of the N spectrum etc. This very strong correlation between subsequent spectra, and the shift by one level with each electron subtraction, is the central experimental result of this work.

In Figure 6.4 we present the full data set of nine consecutive excitation spectra from Device 2. The strong correlation between adjacent spectra is present over the entire set, and strong spectral features can be followed over many consecutive spectra. The "A frame" triangular feature centered at $B = 0$ at the bottom of the N electron spectrum is one such feature. In each consecutive spectrum, removing one electron from the QD results in the upward shift of the existing resonance pattern and the addition of a new ground state to the bottom of the spectrum.

These strong correlations are also present in the spectra of the three other Devices measured. Data from Device 1 is shown in Figure 6.5, Device 3 in Figure 6.6 and Device 4 in Figure 6.7. We note in particular that the spectra of Device 4 appear less correlated than the spectra from the other Devices. This issue of sample dependence is discussed in Section 6.6.3.

6.4 Spin Pairing

The splitting in energy of spin-paired quantum levels is a key indicator distinguishing single-particle and many-body behavior. Spin splitting was observed in the ground state measurements of Section 5.2 and discussed in Section 5.4.2 . Here we discuss spin pairing as it appears in the excited states measurements introduced in Section 6.3 .

Figure 6.8 displays the spectra labeled $N+1$ from Figure 6.6 with a line illustration that serves to identify pairs of parametrically evolving levels. Note that these pairs identified are pairs of wavefunctions *as followed through crossings and anticrossings*. We define following a slowly evolving wavefunction through a crossing or anticrossing as following the *diabatically* evolving level [Takami92]. Following the level at constant N past an anticrossing but not through the anticrossing we define as following the *adiabatically* evolving level [Takami92]. The lines are thus diabatically evolving levels, with slowly changing spatial wavefunctions. The ground state measurements are thus adiabatic levels. It is in the diabatic spectrum of levels that the spin pairing appears, as the lines of Figure 6.8 indicate.

The gap in energy between the spin paired levels is an important energy scale, possibly characteristic of the electron-electron interaction strength in the QD. From the typical pair

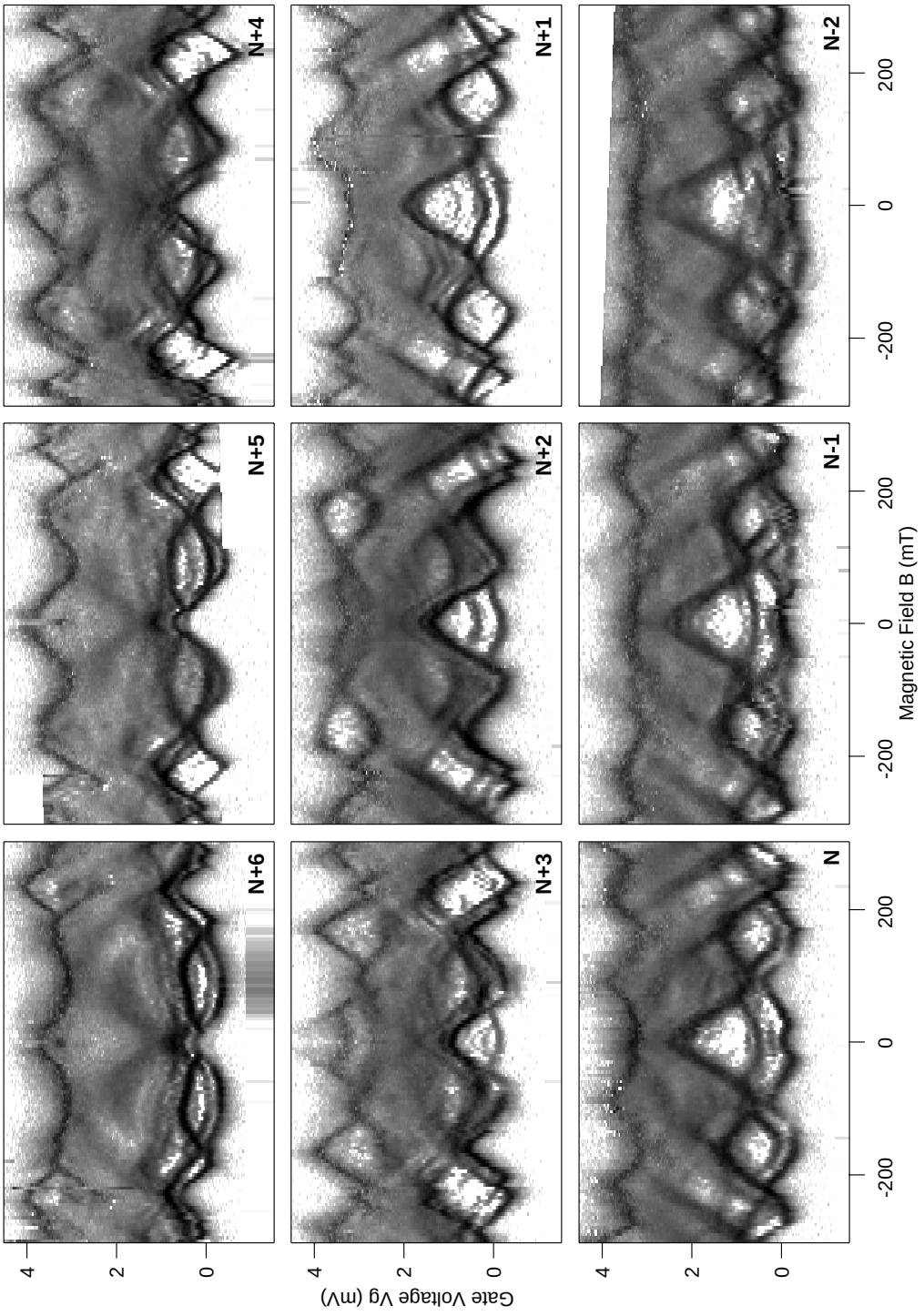

Figure 6.4: The nine successive measured excitation spectra of Device 2. Conductance grey scale is $\sim 0 \rightarrow 0.1e^2/h$.

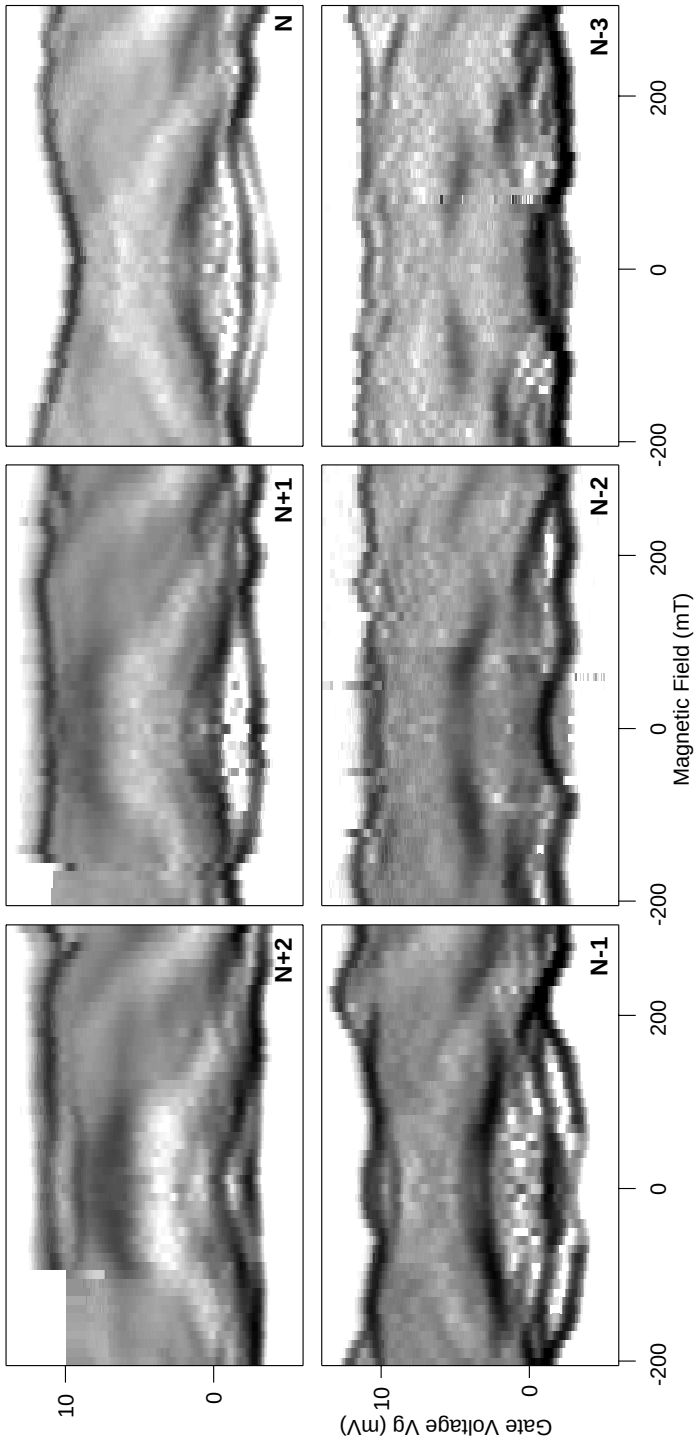

Figure 6.5: The six successive measured excitation spectra of Device 1. Conductance grey scale is $\sim 0 \rightarrow 0.1e^2/h$.

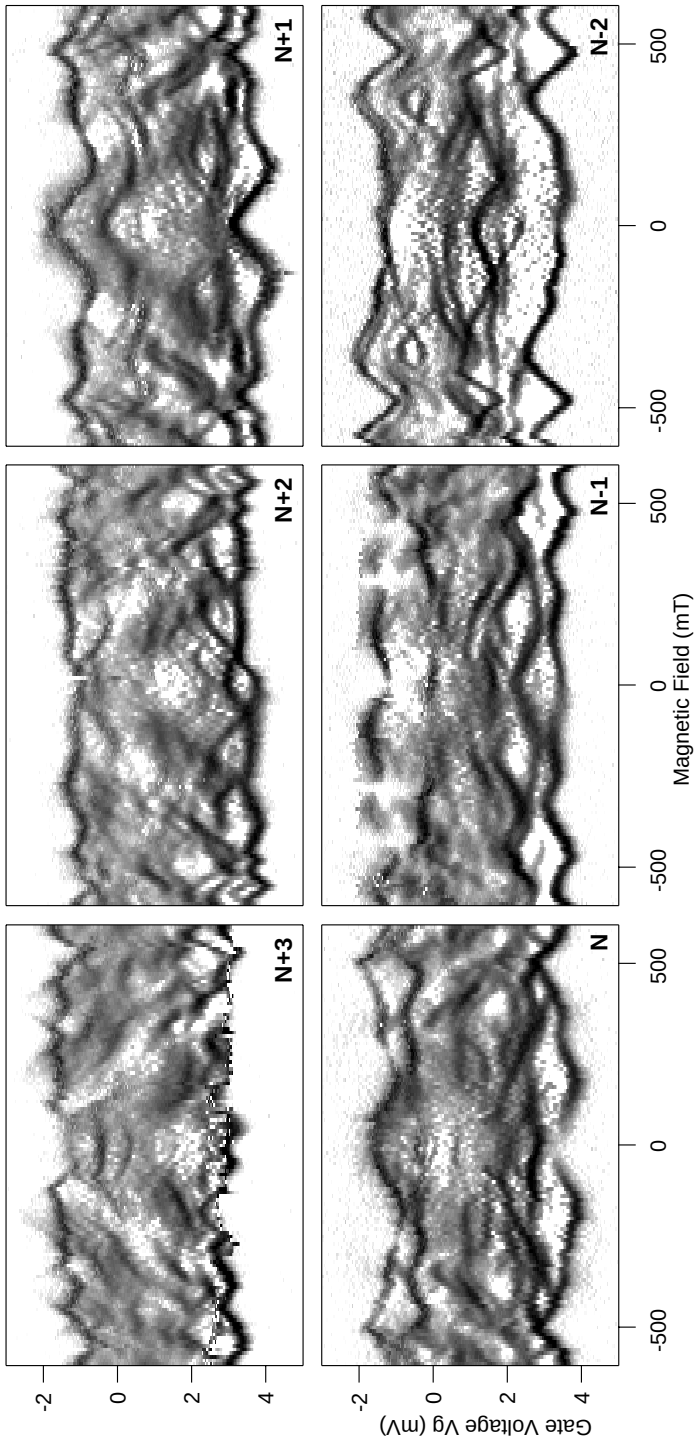

Figure 6.6: The six successive measured excitation spectra of Device 3. Conductance grey scale is $\sim 0 \rightarrow 0.1e^2/h$.

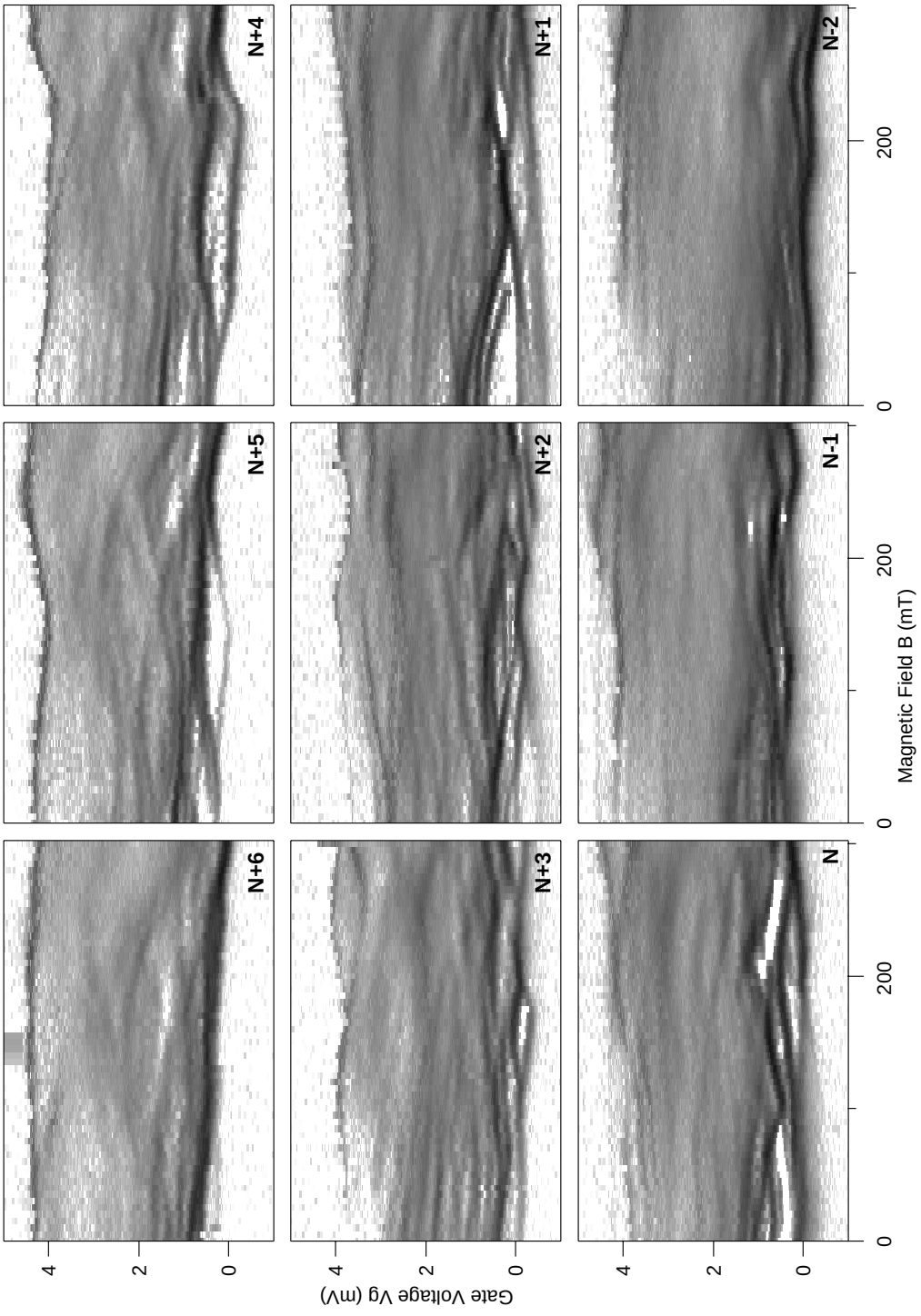

Figure 6.7: The nine successive measured excitation spectra of Device 4. Conductance grey scale is $\sim 0 \rightarrow 0.1e^2/h$.

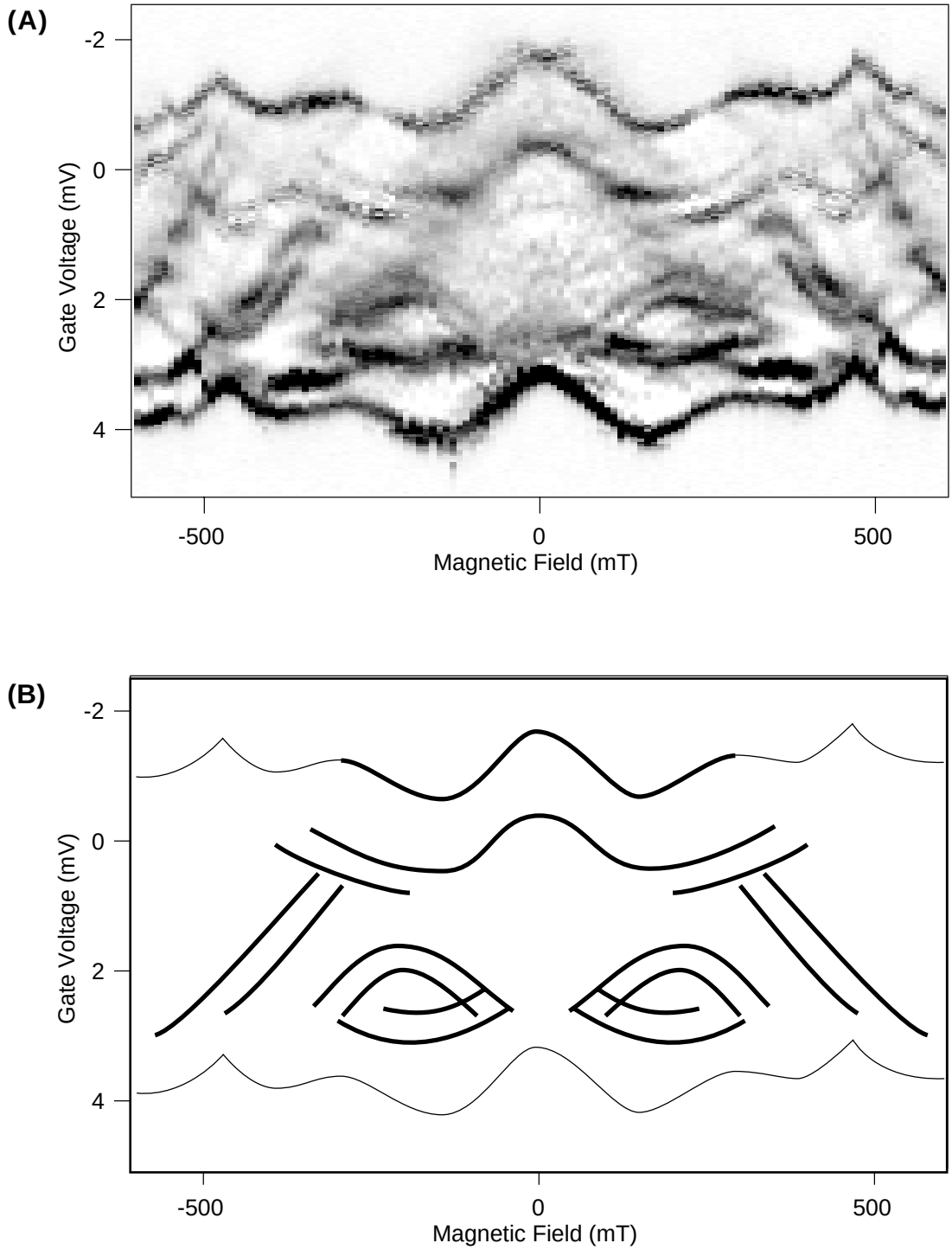

Figure 6.8: (A) Excitation spectrum N+1 from Figure 6.6. (B) Schematic line drawing highlighting visible spin pairs as parallel resonances in the excited state spectrum.

spacing identified in Figure 6.8, we find an spin splitting of $35\mu eV$. This spacing appears independent of magnetic field. For comparison, the average energy spacing Δ between each consecutive ground, 1st, 2nd, 3rd etc resonance is $\Delta \sim 55\mu eV$.

Figure 6.9 shows the same excitation measurement continued to high magnetic field $B \sim 1.5$ Tesla. The spectrum at these higher fields reflects the dominance of the magnetic field in defining the quantum levels; the $B = 0$ spectrum is reorganizing into Landau levels. To accomplish this some of the $B = 0$ quantum states are ascending in energy as they evolve diabatically, others are descending in energy. The result is a spectrum filled with level crossings between the ascending and descending levels. In Figure 6.9 the better resolved descending diabatic levels appear in *paired stripes*, which we identify as spin paired wavefunctions. The energy gap between pairs again appears independent of magnetic field. The dramatic drop in chemical potential at $B \sim 1.3T$ indicates depopulation of the second Landau level. At this high field all electrons occupy the spin up and spin down halves of the lowest Landau level only. From this magnetic field we can extract the 2DEG density inside the QD, and surprisingly find a value of $n_s = 6\text{x}10^{10} cm^{-2}$, approximately one-third the bulk 2DEG value of $n_s = 2\text{x}10^{11} cm^{-2}$.

6.5 Negative Differential Conductance

A final salient feature in much of the experimental data is the appearance of negative differential conductance (NDC) in the Coulomb diamond measurements. Figure 6.10 shows a Coulomb diamond measurement showing both positive and negative differential conductance lines and areas. The NDC typically appears as a line segment in the diamond, very similar to the postive conductance lines. We thus interpret the NDC lines as signatures of individual tunneling DOS peaks, with the new characteristic that when these channels become available for tunneling they cause a *decrease* in the total dc current through the QD.

The diamond measurement of Figure 6.10 was made at $B = 250mT$. The same CB peak is shown evolving in magnetic field in Figure 6.11, at several different source-drain biases. Panel B in particular, at $V_{DS} = -100\mu V$, shows the NDC behaving like any other resolved tunneling level. The conductance signature of the 1st excited state in fact oscillates between a positive and negative differential conductance peak in the field range $B = 200 - 600mT$. Both Figure 6.10 and Figure 6.11 also illustrate that the NDC peaks are most prevalent at

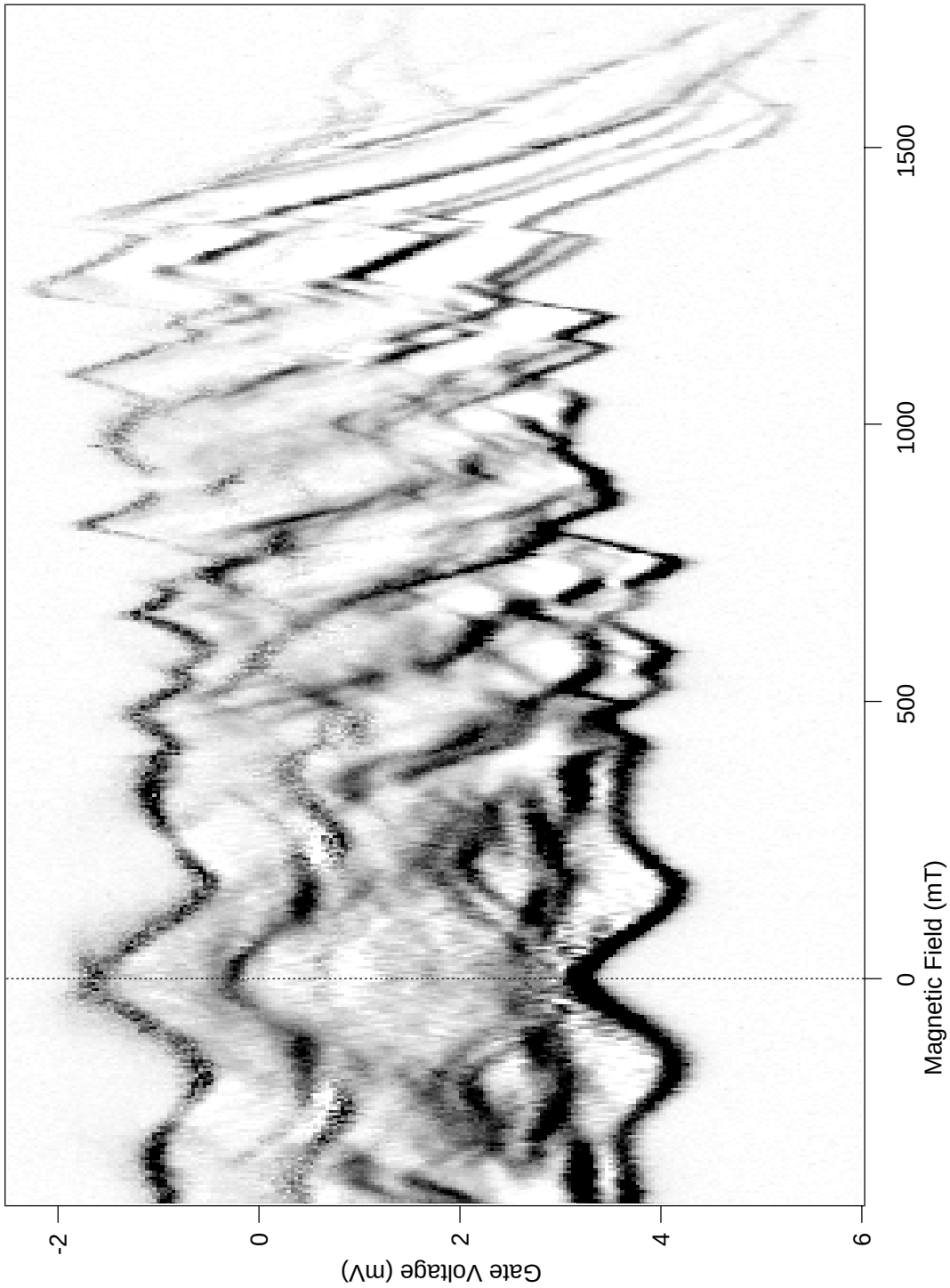

Figure 6.9: The excitation measurement of Figure 6.8 is continued to 1.8T. Levels appear to descend through the spectrum in pairs. Conductance grey scale is $\sim 0 \rightarrow 0.1e^2/h$.

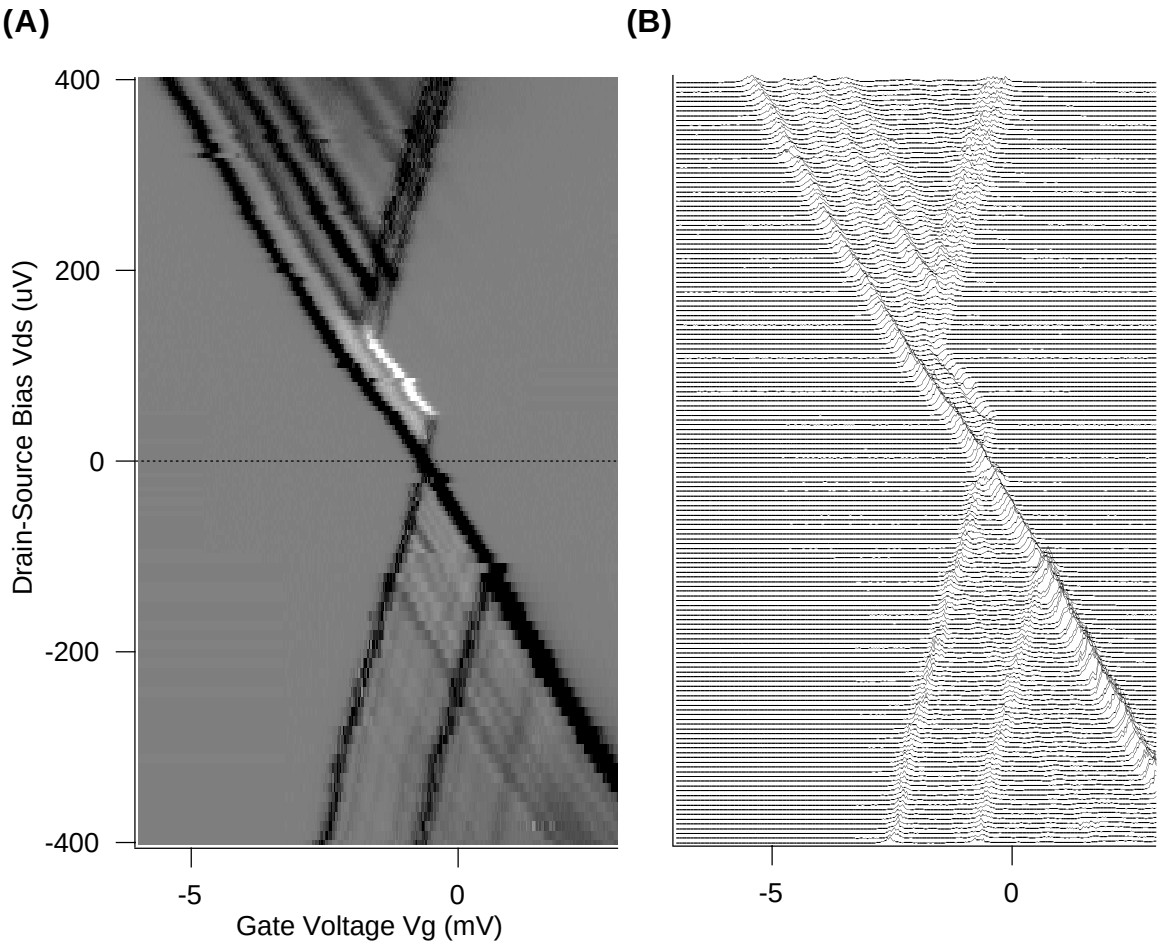

Figure 6.10: (A) A grey scale image of a single Coulomb peak as a function of source-drain bias and gate voltage (Compare to Figure 3.6). Black indicates positive differential conductance, grey zero and white negative differential conductance (NDC). Note the significant NDC that becomes a positive conductance peak after crossing a drain resonance. (B) Raw data for the image (A). Highest conductance peaks at lower right are $\sim 0.2e^2/h$.

low V_{DS} bias, when only a few levels are present in the source-drain transport window.

In the simple transport model of Section 3.3.3, the assumption of fixed level conductances gammaLeft and gammaRight and total relaxation between tunnel events yielded only positive differential conductances when new tunneling channels appeared in the source-drain transport window. The observation of negative differential conductance shows that one or both of these assumptions are incorrect under some circumstances. In particular, we suppose that relaxation between tunnel events is not occuring. Each electron then enters a single-particle level and dwells there some finite time before exiting to the drain or even back to the source. If the dwell time of a newly available level is longer than the average $\tau_{transit} = I_{dc}/e$, then the total dc current will indeed decrease when the new level becomes available. This level will have a NDC signature. A simple realization of this is a new level with good coupling, Γ_L, to the source and very poor coupling, Γ_R, to the drain. Electrons will enter from the source and, as long as no relaxation occurs, dwell within the QD for a considerable time before exiting to the drain.

A more complex and realistic version of this situation occurs when partial relaxation occurs within the QD. An electron then enters from the source, dwells within the QD, then perhaps relaxes to a lower QD level with good coupling gammaRight that allows exit to the drain. Now the precise availability and coupling between levels *within the QD* are determining the transport. Changes in level couplings or level order within the QD induced adiabatically by magnetic field or by increased source-drain bias will potentially change an existing tunneling level from a positive differential conductance signature to a NDC peak, and vice versa. The NDC and conductance changes thus provide a fascinating access to transition couplings between isolated QD levels. We propose this explanation for the observations of Figure 6.10 and Figure 6.11.

6.6 Connection to Single-Particle and Many-Body Theory

6.6.1 Single-particle behavior

The very strong correlation between successive N excitation spectra is a striking demonstration of the dominant single-particle nature of the measured QD spectra. Successive excitation spectra are almost identical, except for the upward energy shift of all levels and the addition of one new level for each electron removed from the QD. This observation is in good agreement with a single-particle description of the QD in which a fixed spectrum

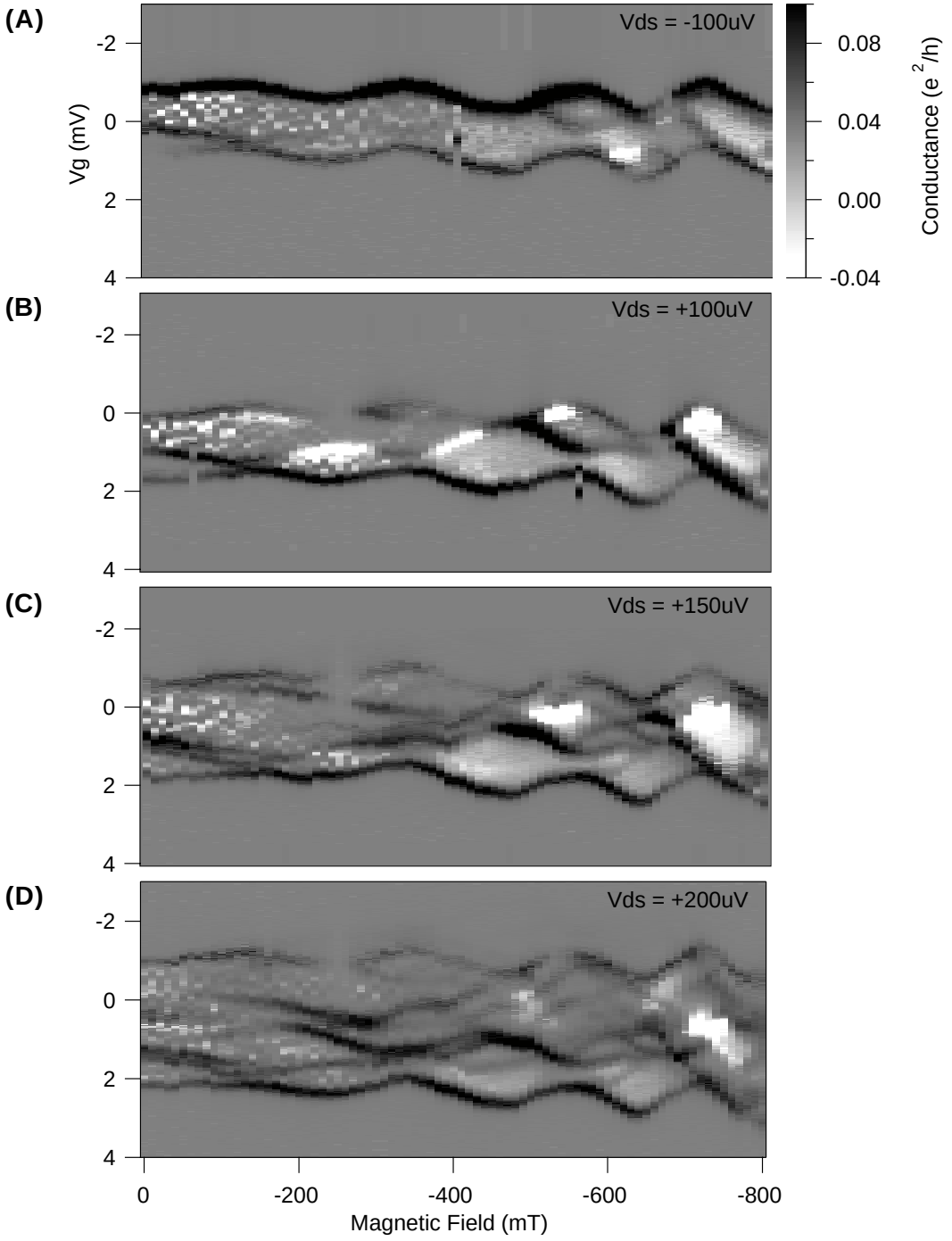

Figure 6.11: Negative differential conductance fluctuations in magnetic field B, for a given CB peak. Note both lines and regions of NDC, and decreasing NDC for higher source-drain bias. (A) At $V_{ds} = -100\mu eV$. (B) At $V_{ds} = +100\mu eV$. (C) At $V_{ds} = +150\mu eV$. (D) At $V_{ds} = +200\mu eV$.

of quantum levels is filled one level at a time. We conclude that in the energy window of $\sim 3-8$ single-particle spacings Δ above the QD Fermi level, the QD spectrum is well described by a single-particle model contrary to possible expectations that electron-electron interactions may strongly perturb the level structure.

6.6.2 Evidence of many-body interactions

Although the dominant spectral features appear to be well described by a single-particle picture, several significant deviations from this simple model exist and indicate that electron-electron interactions must be considered to explain the more detailed spectral observations. The energy splitting of nominally degenerate spin 1/2 quantum levels is potentially one of the strongest indicators of many-body effects within the QD. Here we discuss the possible causes of spin splitting in the context of many-body effects. A second strong indicator of many-body effects is the decrease in excited state resolution at higher energies.

The simplest physical mechanism for spin splitting of electron states is Zeeman splitting due to the external magnetic field. This single-electron effect causes an energy splitting between opposite spin electrons in the same spatial orbital as the electrons either align or antialign with the external magnetic field. In GaAs [Ando82] this energy splitting is

$$E_{Zeeman} = g_L^* \mu_B B = 23.2 \mu eV/Tesla \tag{6.1}$$

where g_L^* is the effective Lande g factor and μ_B is the Bohr magneton. At $100mT$ the expected Zeeman splitting is therefore $2.3\mu eV$, an order of magnitude less than the observed and apparently field independent $35\mu eV$ splitting. The Zeeman effect is therefore not responsible for the observed spin splitting.

A second possible mechanism is the spin-orbit interaction, coupling the intrinsic electron spin to their spatial orbital motion. Again this is essentially a single-particle effect. Partially filled atomic shells can have non-zero orbital and spin angular momentum; the orbital motion of the uncompensated charge produces a local magnetic field coupling to the electron spins. This spin-orbit splitting is independent of external field and in GaAs 2DEGs the strength of the splitting is debated, with estimates of order $E_{so} \sim 50\mu eV$ at a density $n_s \sim 2\text{x}10^{11} cm^{-2}$ [Pfeffer95]. This energy scale and field independence make this a possible candidate to explain the observed QD splittings.

Electron-electron interactions offer a third mechanism for spin splitting of electron levels. Both the direct and exchange terms of the interaction (Eqn 2.6) can cause a splitting of spin degenerate levels in the isolated QD system. The direct term is usually accounted for using the constant charging energy approximation, but a more exact consideration allows the possibility of different charging costs for different level occupancies and spatial wavefunction overlaps including pairs in a single orbital. Splitting due to this direct Coulomb repulsion would however fluctuate significantly as level occupancies vary with magnetic field. Although this appears to happen in Figure 6.8 for one pair around $B = 0$, many pairs in the excitation spectra seem to have a B-independent value of the pairing energy gap. This suggests the exchange interaction may be a more likely cause for the observed splitting.

The exchange electron-electron interaction is well known to cause spin splitting of otherwise degenerate levels in atomic spectra [Bransden83]. As identical Fermions, electrons require a total many-body wavefunction that is antisymmetric under coordinate exchange of any two particles. For two electrons occupying two degenerate single-electron orbitals each with spin 1/2, this condition generates many-body states that form a singlet $S = 0$ and triplet $S = 1$ in total spin $S = s1 + s2$. The singlet is spatially symmetric, the triplet spatially antisymmetric. Antisymmetric spatial states have less spatial overlap between the two electrons, thus less Coulomb repulsion and a lower total state energy. The originally degenerate states have now been split into a lower energy triplet and a higher energy singlet due to the exchange interaction. The amount of energy splitting is often referred to as the exchange splitting or exchange energy, and is observed in the Hund's rule behaviour of spin aligned atomic shell filling and fine structure. This exchange energy was previously discussed in Section 2.2.3 and defined exactly in Eqn 2.8. In the artificial atom of our quantum dot, the two single-electron orbitals are perhaps not degenerate, just neighbours in the single-electron eigenstate ladder. In this case each single-particle spin 1/2 eigenstate may be split into it's two spin components with an exchange energy separation. Experimental studies of few electron QDs have measured exchange induced spin splittings on the order of $100\mu eV$ [Tarucha96]. These results were also supported by exact diagonalization numerical calculations [Eto97a]. Further, if the exchange energy is larger than the single-particle spacing to the next level, then spin-aligned half-filling of successive energy levels will occur. Successive N states will no longer be spin pairs; the spin pairs will be separated by an exchange energy or equivalently by E^{ex}/Δ other eigenstates. Figure 6.8 shows diabatic spin pairs separated by zero, one or two intervening quantum levels. This implies directly that

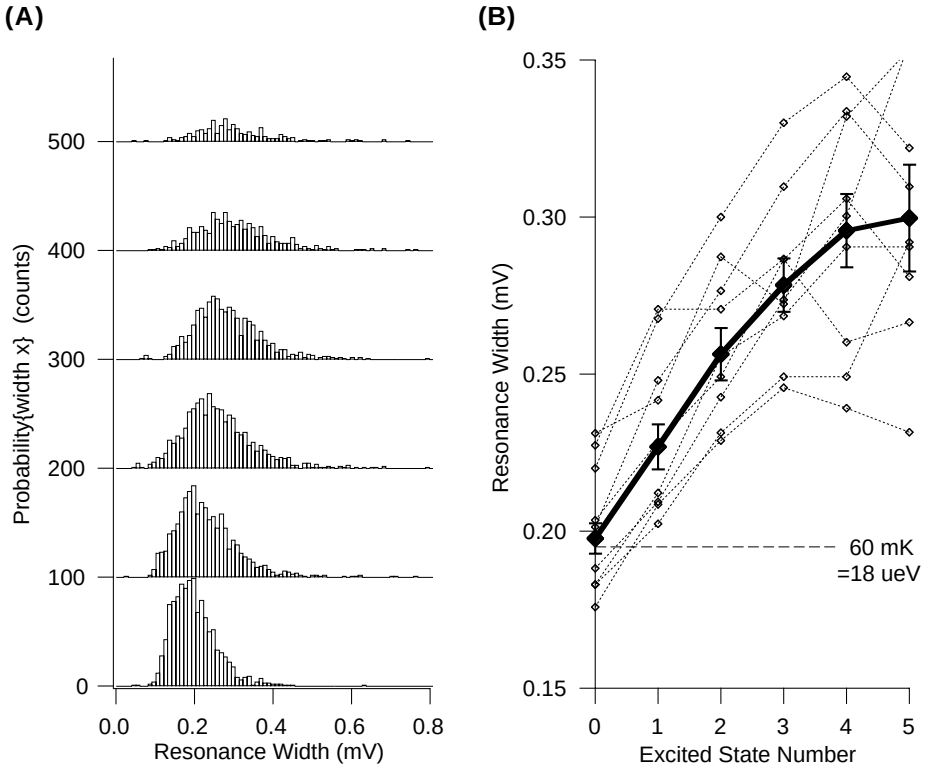

Figure 6.12: (A) Histograms of the ground, 1st, 2nd, 3rd, 4th and 5th excited state resonance widths, compiled for the nine excitation spectra of Figure 6.4. The bottom histogram corresponds to the ground state widths, the top histogram corresponds to the 5th excited state widths. (B) Distribution means for each excitation spectra (dotted) and average for all nine spectra (solid) with errors from the distribution standard deviations of panel A.

the QD is frequently spin polarized, with one or two uncompensated and aligned electron spins. We argue that this spin splitting and resultant spin polarization of the QD is due to the exchange interaction between electrons.

Other strong evidence for many-body effects is also visible in the excited spectra data. The resolvability of excited states appears to decay for higher energies above the QD ground state. Figure 6.12 shows distributions of the measured peak width of the ground, 1st, 2nd, 3rd and higher resonances in the excited state spectrum, averaged over all magnetic fields and all spectra of Device 2 (Figure 6.4). The width of the excited state resonances grows almost linearly with state number or energy above the QD ground state. Two mechanisms could explain this broadening, 1) decreased confinement lifetime due to weaker barrier

confinement within the QD, or 2) decreased excited state lifetime due to energy decay inside the QD by interaction. Weaker barrier confinement should be accompanied by larger couplings and larger resonance amplitudes. This characteristic is not visible in the excitation spectra, in fact the excited resonances generally grow progressively weaker in amplitude at higher energy. Evidence for inelastic decay within the QD has already been discussed in the context of the NDC observations of Section 6.5, and some kind of broadening of excited resonances is expected in any system. At the low temperatures of our experiment, the dominant interactions that can cause this broadening are electron-electron interactions. In a bulk 2D system, using Fermi's Golden Rule to describe possible e-e interactions the excited state widths are expected to increase as $\delta E \sim \varepsilon^2$, where ε is the energy of the excited state above the Fermi surface. We discuss this issue of excited state widths and decay in detail in Chapter 8.

6.6.3 Sample dependence of Spectral Correlations

Figure 6.4, Figure 6.5, Figure 6.6 and Figure 6.7 display sets of successive excitation spectra for the four Devices measured in this study. We have discussed the strong correlations between any given N and $N+1$ excitation spectrum above, but careful inspection of the data from the four different Devices shows that the strength of the correlation between neighboring spectra varies from one Device to the next. In particular, Devices 1 and 2 appear to show the strongest correlations, while both the smaller Device 3 and the larger Device 4 show weaker neighbor correlations. All four Devices were fabricated from the same GaAs/AlGaAs heterstructure substrate. With only four data points, however, it is difficult to ascertain the size dependence of this correlation strength. The question has been addressed quantitatively by Patel et al [Patel98b] who found that the largest of three QD Devices showed evidence of the most "spectral scrambling". It is the data of Figure 6.7 that is most anomalous in this respect; as a larger Device it is expected that it would have shown the strongest correlations between N and $N+1$ spectra. This issue requires further investigation.

Chapter 7

Correlations between Ground & Excited Spectra

7.1 Introduction

The system ground state is usually a well defined entity in both the single-particle and the many-body theoretical descriptions. Density functional methods, for example, have been quite successful at calculating many-body ground states. The excited states are similarly well defined within the single-particle picture. In contrast, many-body theories including mean-field approximations are often unable to uniquely define the system excited states. This difficulty is one of the motivations for our work, but also points to the potential usefulness of comparing the measured ground states and excited states. Correlations between the ground and excited spectra offer a method to quantify the single-particle and many-body characteristics.

Section 7.2 describes an empirical comparison between the ground and excited spectra. Section 7.3 attempts to quantify cross-correlations between the excited spectra and the assembled ground state spectrum.

7.2 Empirical Correlations

The strong correlations between successive excitation spectra supported a single-particle description with a fixed ladder of successively filled levels. In this picture, a level is unaffected by electron addition to the QD; it will be the same wavefunction and have the same

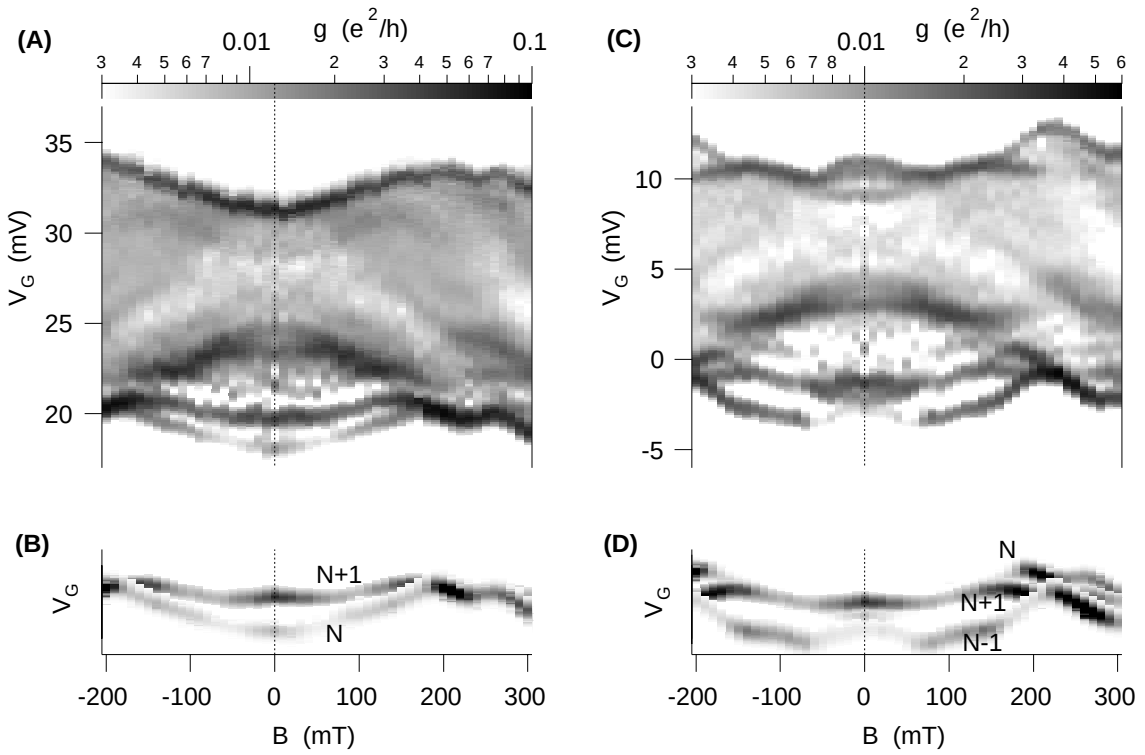

Figure 7.1: Comparison of ground and excited spectra, for Device 1. (A) N electron excitation spectrum (B) N and N+1 ground states (C) N-1 excitation spectrum (D) N-1, N and N+1 ground states.

magnetic field fingerprint whether it is measured as a ground state or an excited state. In particular, the first excited state of N electrons should be identical to the ground state of $N+1$. More generally, the mth excited state of N should match the ground state of $N+m$.

Figure 7.1 tests this proposal by comparing directly the first excited state of N to the ground state of $N+1$. Panel A shows the excitation spectrum for the N electron system. Panel B shows the N and $N+1$ ground states collapsed together in energy in the same way as in Figure 5.3. It can be seen that the magnetoconductance fingerprint of the Nth zero-bias CB peak matches the resonances at both top and bottom of the Nth finite bias CB peak, because all three are identified with the ground state of the N-electron system. More significantly, the $N+1$ zero-bias CB peak (ground state) matches closely the second resonance (first excited state) of the Nth finite bias peak in position, height and relative spacing between the levels, exactly as suggested above.

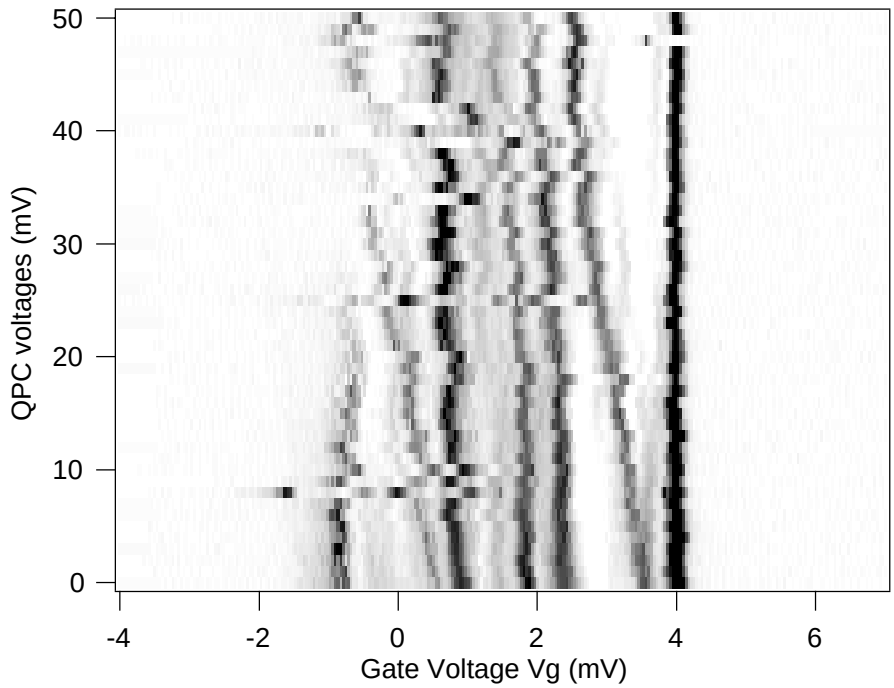

Figure 7.2: The impact of shape distortion on the excitation spectrum. At fixed source-drain bias and constant N, the shape of the QD is continuously perturbed by simultaneous modification of both plunger gate and QPC voltages. Conductance grey scale is $\sim 0 \rightarrow 0.1e^2/h$.

This comparison method also highlights some important departures that arise presumably as a result of electron-electron interactions. The finite bias structure corresponding to the excited states spectrum of the $N-1$ electron system is shown in Figure 7.1C, whereas Figure 7.1D displays the $N-1$, N and $N+1$ zero bias peaks shifted in energy from Figure 5.3 to best match the $N-1$ excited state spectrum. The relative position of the N and $N+1$ levels in panel D differs considerably from that in panel B. The $N+1$ ground state has been shifted from its alignment of Figure 7.1B until it is overlapping and even changing places with the Nth ground state. This apparent $30\mu eV$ shift of the $N+1$ level is comparable to the average level spacing of $35\mu eV$, and indicates that while levels may undergo an overall shift in energy as one electron is added, the level "fingerprint" (position and height fluctuations in B) appears largely unchanged. Smaller, similar shifts in level spacings exist in almost all neighboring excitation spectra.

We are suggesting that these energy fluctuations are caused by the addition of the

new electron, but another simpler explanation must also be considered. Experimentally the addition of another electron to the QD is achieved by making the plunger gate more positive, expanding the size of the confinement region to acommodate one more electron. This change in size and simultaneous change in shape could affect all eigenfunctions of the QD and cause the energy fluctuations observed. The influence of the shape change on the spectrum was investigated by repeated measurements of the excitation spectrum as the QD shape was distorted but the area and total electron number N was held constant. Figure 7.2 shows an excited spectrum measurement of Device 2, where the vertical axis is shape distortion. Many of the levels appear to change only very slowly in both position and amplitude as the QD shape is distorted, but two levels apparently are more strongly affected and evolve fairly quickly in energy. We suggest that these two levels may have a higher spatial probability density near to the plunger gate location. In any case, the full vertical scale of shape distortion in Figure 7.2 is equivalent to the gate voltage change required to add approximately 5 electrons to the QD. The spectral changes induced, although significant on this scale, appear smaller than the actual changes observed between successive N and $N + 1$ spectra in Figure 7.1.

7.3 Quantitative Cross-Correlations

7.3.1 Correlations between adjacent excitation spectra

Nine successive excitation spectra were measured in Device 2, and displayed in Figure 6.4 . Visually adjacent spectra are seen to be strongly correlated, with a shift upward of all levels and the addition of one new ground state level for each electron removed. Here we attempt to objectively determine that energy shift by cross-correlating successive excitation spectra.

Figure 7.3 shows the $N + 1$ and $N + 2$ spectra from Figure 6.4 . The cross-correlation is accomplished by first enhancing conductance peaks and valleys of each excitation fingerprint, then slowly sliding the $N + 2$ fingerprint over the $N + 1$ fingerprint and taking the product of the two images at each slide increment. This is exactly a cross-correlation of the two spectra, as a function of energy. The enhancement consists of smoothing a spectra, then subtracting the smoothed version from the original conductance data. The resultant image has enhanced peaks and valleys about a zero mean value. The cross-correlation is much more effective with this positive/negative zero mean data set.

The auto-correlation of the $N + 1$ spectrum identifies a zero for the energy shift scale,

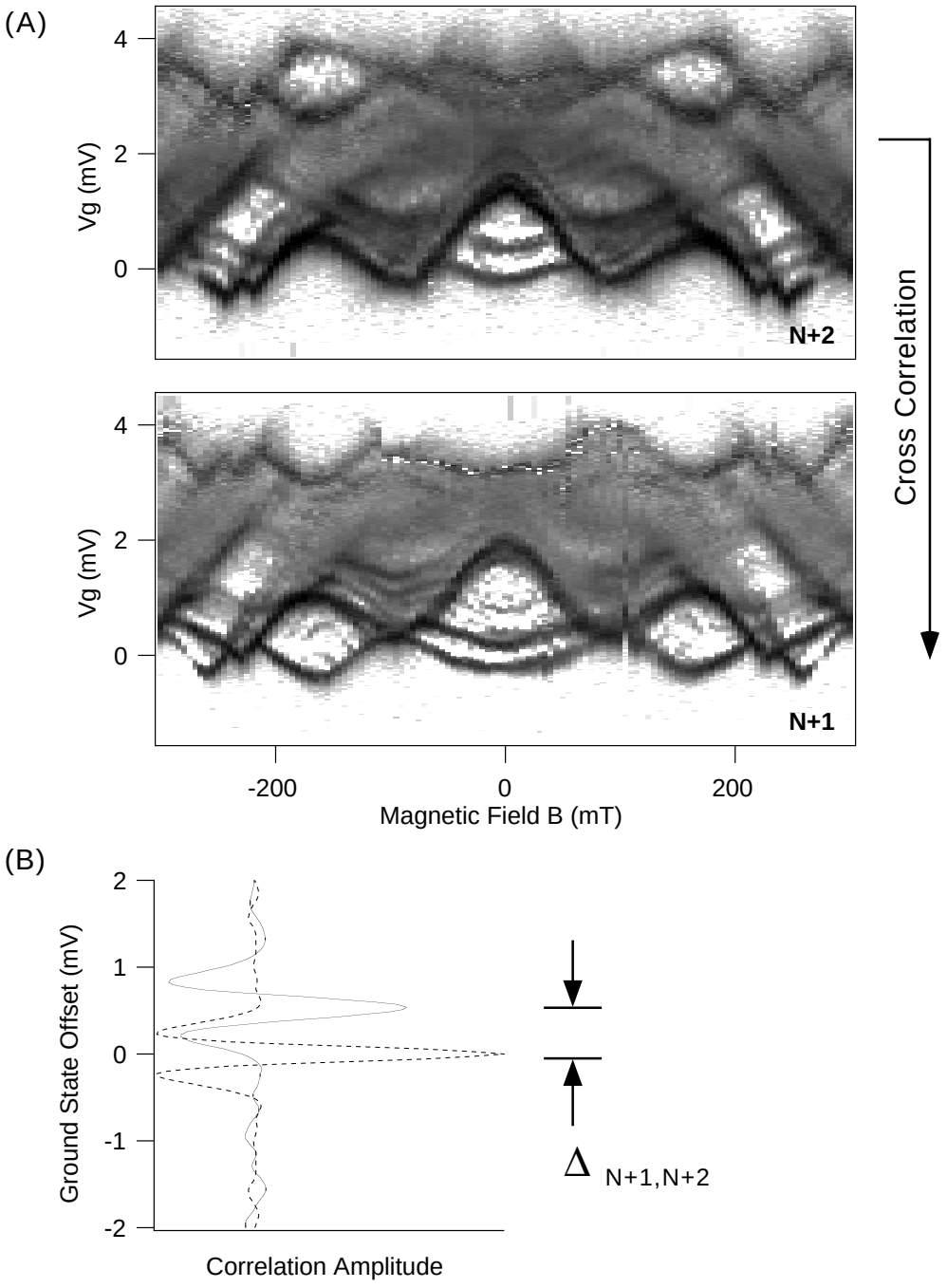

Figure 7.3: Excitation spectra cross-correlations. (A) The N+2 and N+1 excitation spectra of Device 2. Cross-correlation is conducted by sliding the N+2 image vertically over the N+1 image and evaluating the product. (B) Magnitude of the correlation signal as a function of relative displacement, for the N+1 autocorrelation (dotted) and the N+2,N+1 cross-correlation (solid).

at the average position of the $N+1$ ground state resonance. The cross-correlation of the $N+2$ and $N+1$ spectra then shows a large peak displaced from this zero by the single level spacing energy that we have already identified visually. In other words, the $N+2$ spectrum overlays the $N+1$ spectrum and matches it well when it is displaced slightly upwards from the $N+1$ ground state. The spacing between the $N+1$ auto-correlation peak and the $N+1/N+2$ cross-correlation peak is thus an objective measurement of the energy gap between the $N+1$ and $N+2$ levels in the single-particle-like QD spectrum. These two correlation peaks are shown in Figure 7.3B. The height and width of the cross-correlation peak should also contain information on degree and precision of the correlation agreement, however this data appears to be strongly influenced by the exact correlation method and is thus not used. We also note that the highly desirable cross-correlations of individual ground states with excited spectra were similarly not possible to extract despite strong efforts to devise a robust cross-correlation method for this analysis. The cross-correlation of adjacent excitation spectra was in fact the only correlation that proved robust to small changes in numeric method.

The cross-correlation is repeated for all eight pairs of adjacent spectra from Figure 6.4 . The eight level spacings aquired can then be used to assemble the successive ground state fingerprints. In Section 5.3 we achieved this by visual best match only; here we use the objective cross-correlation spacings. Figure 7.4 shows both the previous visually assembled spectrum and the new assembled spectrum using the cross-correlation spacings. There exist only small differences in the spacings, validating to some degree the previous visual assembly method. More significantly, the previous conclusions of Section 5.4 on the motion of slowly changing "diabatic" wavefunctions ascending and descending through the measured ground state spectrum are reinforced by the objectively assembled ground states.

7.3.2 Comparison of ground spectrum & excitation spectrum

We now continue to the final and strongest comparison between the measured ground and excited states. Figure 7.5 overlays the objectively assembled ground states of Figure 7.4A onto the $N-1$ excitation spectra. The agreement between these seven ground state fingerprints and the excitation spectrum appears remarkable – the ground states map directly onto most features of the excitation spectrum. The lowest ground state naturally maps exactly onto the lowest excitation resonance since it corresponds to the $N-1$ ground state. Labeling this as ground state one, the second and third ground states also map very closely

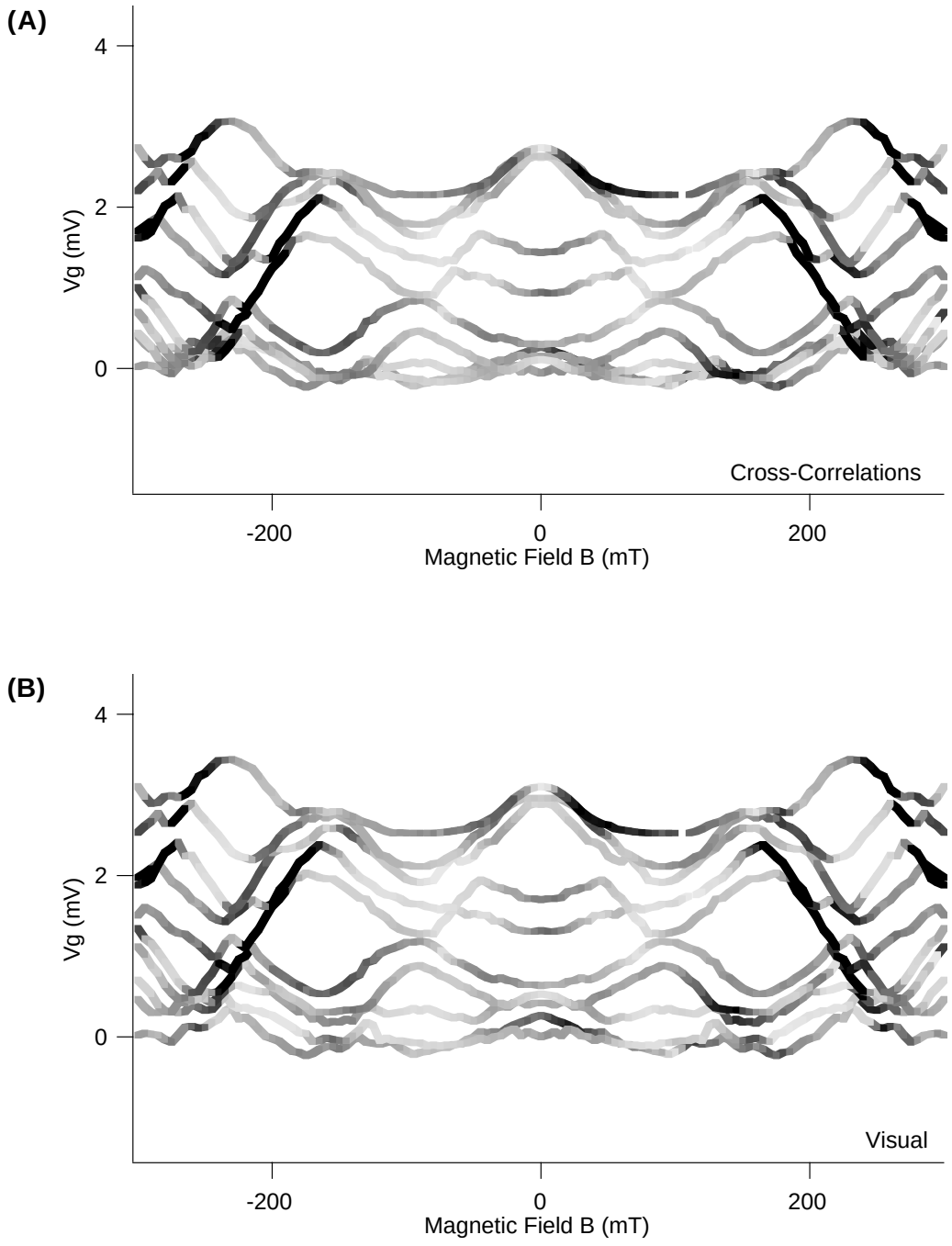

Figure 7.4: (A) Quantitatively assembled ground state spectrum for Device 2, using the relative displacements found from cross-correlation of successive excitation spectra. (B) Visually assembled spectrum from Figure 5.4. Line shading in both panels indicates ground state peak amplitude.

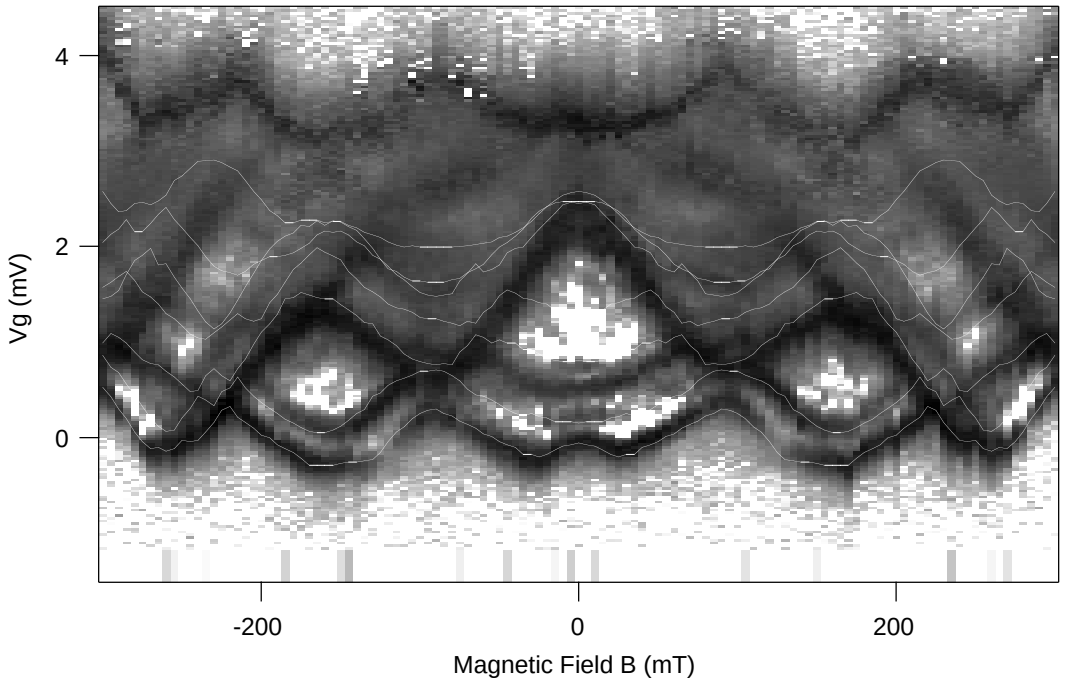

Figure 7.5: The assembled spectrum of Figure 7.4A (white lines) is overlayed on the measured N electron excitation spectrum of Device 2 (grey scale image).

onto the next two resonances of the excitation spectrum, particularly in the field range $75 - 300mT$. The "A frame" feature about $B = 0$ in the excitation spectrum is reproduced by the higher fourth to seventh assembled ground states. The two descending stripes at $100 - 250mT$ and $200 - 300mT$ are visible as kinks in the fingerprints of all states in the assembled ground spectrum. This overlay of these assembled ground spectra onto corresponding excitation spectra can be accomplished for each excitation spectrum with similar results. The observed 1:1 mapping of ground states to corresponding excited states is our strongest evidence of the dominant single-particle QD nature.

We have highlighted the accuracy of this 1:1 mapping of ground states onto excited states above. Closer inspection of Figure 7.5 however uncovers many instances where the mapping is not exact, and perhaps is actually quite poor. In Figure 7.5 and in all other mapping overlays the first, second and third ground states seem to map quite well onto the ground, first and second excited states in the excitation spectrum. This accuracy appears to decay when higher states are compared, as seen with the fourth to seventh ground states in the $100 - 300mT$ field range of Figure 7.5 . In this range resonances in the excitation

spectra are less well resolved, and the ground states reproduce poorly only some of the excitation spectrum features. Many of the ascending ground state segments are not visible in the excitation spectrum, including the second, fourth and sixth ground states between $200mT$ and $250mT$. Near $B = 0$ the second, third and fourth ground states do not seem to map onto any existing excited state resonance and in fact misalign with what appears as the first excited state between $-75mT$ and $+75mT$. The two descending stripes discussed above are visible in both the excitation spectrum and the ground states, but again are misaligned increasingly for the higher ground states.

This misalignment of the descending stripe in the excitation spectrum with the descending diabatic pair of wavefunctions in the ground states can be improved with an ad hoc adjustment of the magnetic field scale. Figure 7.6 shows the same data with improved alignment between the ground and excited states where they correspond to the descending levels. These levels are presumed to be descending in a pair through the spectrum to form one of the lower Landau levels as discussed in Section 6.4 . The improved agreement and modified descent angle was achieved by "squeezing" the magnetic field scale of successively higher ground states by 2% for each electron removed. This modification of the magnetic field scale implies a gradual change to the confining potential of the QD. At these low electron numbers the surface gates defining the QD have large negative votages, extending their depletion region and shrinking the dot area. Pushing more electrons out of the dot may result in an increasingly shallow bowl shaped potential well. In this case, the single-particle level spacing will stop increasing and actually begin to shrink as the potential well becomes a softer and shallower bowl. The magnetic field scale of the fluctuations due to crossings and anticrossings will also shrink. It is this possible change in the QD potential well and B field behavior that may justify the squeezed field scales and improved alignment of Figure 7.6 .

7.3.3 Connection to Single-Particle and Many-Body Theory

The 1:1 mapping between corresponding ground and excited state measurements has provided our strongest evidence of the dominant single-particle-like behavior of the observed QD spectrum. The ground/excited correlations have also reinforced the conclusion that many-body effects do exist and perturb the spectrum in several ways. Most importantly, they have produced the first generalized observations quantifying the boundary between these two descriptions – the excellent 1:1 mapping for low states and the decay in mapping

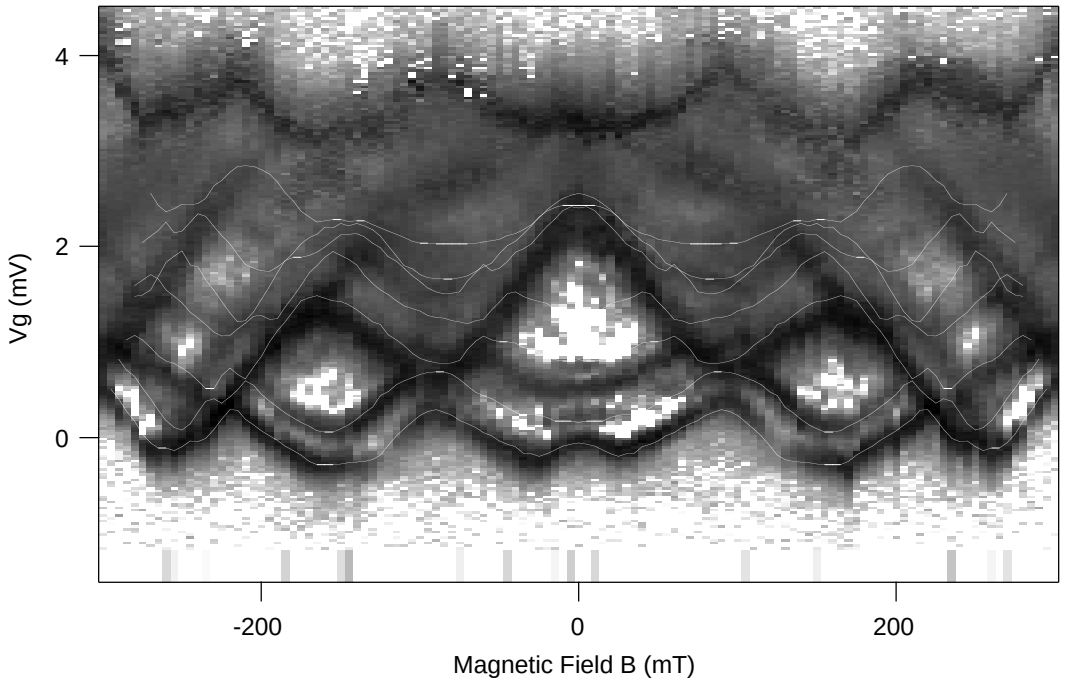

Figure 7.6: Identical to Figure 7.5A except that the 1:1 mapping between ground and excited spectra has been improved by compressing the B scale of higher ground state traces.

accuracy for higher states indicates that the single-particle model has limits to it's applicability. At higher energies above the ground state the single-particle picture does not fit the measured excitation spectrum. At low energies within a few levels of the ground state the single-particle model does explain the measured excitation spectrum. This identification of energy regimes with different behavior is one of our major experimental results, and hopefully may allow a reconciliation between the apparently contradictory single-particle and many-body descriptions.

Chapter 8

A Unified Theoretical Interpretation

8.1 Introduction

We have seen in the experimental data of Section 5 and Section 6 evidence of both single-particle and many-body properties in the quantum dot level spectrum. In Section 7, analysis of correlations between the measured ground and excited spectra indicated a possible boundary between the different regimes in which each of these behaviors exists. We have so far been able to link only parts of many-body theory to individual experimental results, and parts of single-particle theory to others. An arbitrarily complex many-body theory can of course explain all behavior exactly, and of course is also intractable. From the experiment however it is clear that this exact theory must simplify to essentially a single-particle description under certain circumstances. A clear description of those circumstances and the simplifications allowed is our present goal – and if possible a unified understanding that bridges smoothly between the observed interaction-related properties and the observed single-particle properties.

To begin this understanding, it is crucial to recall two experimental constraints limiting the data presented. The first is the energy range studied; all the spectroscopic data collected describes only the handful of levels immediately surrounding the QD Fermi energy E_F. Most of the data in fact probes only those 3-8 excited states directly above E_F. Our conclusions about single-particle and many-body properties thus only apply within

this experimentally accessed energy range. The second experimental constraint is the spectroscopy method used; nonlinear electron tunneling transport from source to dot to drain. As in the optical spectroscopy of atoms, there is good reason to suspect that effective selection rules limit this tunneling DOS measured to a subset of the full many-body spectrum [Pfankuche95;Weinmann95]. Consideration of these two constraints will prove essential to a broader understanding of the experimental results.

In Section 8.2 we review the theory of Fermi liquids which serves as the foundation for the single-particle based understanding of most conduction electron properties of metals. This statistical description of quasiparticle excitations within an infinite sea of interacting electrons should be contrasted with the atomic many-body approach where individual orbitals and particle interactions are calculated (Section 2.2). Section 8.3 then attempts to unite these different approaches to the many-body problem by considering the mesoscopic quantum dot system, a system that is both smaller than an inifite Fermi liquid and larger than a single atom. We attempt to apply this new theoretical framework to understanding the QD experimental data.

8.2 The Electron Gas as a Fermi Liquid

The Landau theory of Fermi liquids describes an infinite system of interacting Fermions in the $kT < E_F$ quantum regime. The energy distribution of the particles in this quantum limit obeys Fermi-Dirac statistics. Each particle in the system interacts with every other particle, thus excitations of the system from the ground state to an excited state are intrinsically a collective phenomena. Instead of a single-electron transitioning independently to a higher energy state in a metal, we must consider the electron and it's interaction with every other electron. Together this elementary excitation is labelled a "quasiparticle" in the Landau theory and remarkably, they can successfully be treated as individual particles with slightly modified properties. This treatment is accurate in the low temperature regime, when only a few elementary excitations exist, they are long lived and they interact weakly with one another. Another way of phrasing the low temperature requirement is to constrain the quasiparticles to energies very near the Fermi surface. Their lifetime is directly dependent on this energy difference, since the quasiparticles are not exact eigenstates they must decay and the decay time gives an uncertainty in their energy. The decay rate can be estimated

using Fermi's Golden Rule as [Pines89]

$$\gamma(\varepsilon) \sim \frac{\varepsilon^2}{E_F} \tag{8.1}$$

where ε is the quasiparticle energy above the fermi surface. This decay process is via interaction and scattering with the other quasiparticles; a single excited electron scatters off an electron below the Fermi level to create a second excited electron and a new hole. After one scattering there are then three quasiparticles, after another scattering five, then seven etc. For quasiparticle energies $|\varepsilon| \ll E_F$ the quasiparticle lifetime is long according to Eqn 8.1, the states are well defined in energy and we are able to treat them as independent entities. Many average properties of the conduction electrons in a metal are then described accurately through the statistical response of these quasiparticles to an applied perturbation.

8.3 Interacting Electrons in the Mesoscopic QD

8.3.1 Interactions in a Mesoscopic System

The quantum dot is a mesoscopic size system, a small metal island in between an atom and a bulk metal in size and properties. The Fermi liquid theory describes excited state properties of electrons within an infinite and homogenous positive background. Atomic theory describes discrete electron orbitals, and transitions between them within the spherically symmetric nuclear potential. We wish to merge these two approaches to understand the experimental QD tunneling transitions observed.

The quasiparticle excitations of the Fermi liquid are single-particle like excitations in the continuous and increasing DOS above the Fermi level. Their decay by electron-electron interaction is controlled by both the density of final states to scatter into and the interaction matrix element between the initial and final states. In the continuous DOS of a bulk electron gas this leads to the quadratic Golden Rule behaviour above. Assuming a finite diffusive system, similar application of the Golden Rule approach yields [Sivan94b]

$$\gamma(\varepsilon) \approx \Delta(\frac{\varepsilon}{g\Delta})^2 \tag{8.2}$$

The dimensionless system conductance g is defined as $g = E_{TH}/\Delta$, where the Thouless energy E_{TH} is the inverse time of diffusion through the system. In general this rate (Eqn 8.2)

is much larger than the infinite system rate (Eqn 8.1). However if we approximate E_{TH} as the time to cross our ballistic QD, then $E_{TH} \approx \sqrt{N}\Delta$, where N is the number of electrons in the QD and Eqn 8.2 reduces in this approximation to Eqn 8.1. Both formulas predict a quadratically increasing width for the QD tunneling resonances higher in energy above the Fermi level. The exact many-body spectrum of the finite QD system is however atomic like – discrete near the Fermi level, then increasing in density and eventually quasicontinuous at high energies above E_F (recall Section 2.2.2) . The Fermi liquid quasiparticle theory must be modified to account for the discrete QD spectrum near the Fermi level by considering this limited number of final states available for electron-electron scattering. The general result (Eqn 8.2) is expected to overestimate the rate of scattering and thus also overestimate the energy width of the quasiparticle states.

The extension of the quasiparticle description to the finite Fermi system has recently been proposed by Altshuler et al [Altshuler97]. The small number of discrete low energy excited states in the finite QD system is predicted to have a dramatic effect on the quasiparticle spectrum. Low energy electron excitations have at most a handful of other still lower energy states to scatter with. In the ideal isolated system when no other decay mechanisms are considered, these excited quasiparticles may have an extremely long lifetime and a very narrow linewidth. Altshuler et al predict that the lowest excitations may have no scattering path available, and are in fact almost eigenstates with a very long lifetime not described by the Golden Rule. This has been labeled sub-Golden Rule decay. Their complete theoretical description of this problems maps the scattering path enumeration in Fock space onto the Anderson localization problem, and predicts quantitatively different energy regimes of quasiparticle lifetime behavior. Quasiparticle states lower than the energy

$$E^* \approx \sqrt[4]{N}\Delta \tag{8.3}$$

have access to a limited number of many-body states, and in this regime of limited decay they display a sub-Golden Rule linewidth. Quasiparticle states above E^* have access to a sufficiently dense spectrum of many-body states and therefore decay according to the Golden Rule of Eqn 8.2, with a lorentzian energy lineshape. For even higher energies above the Thouless energy

$$E_{TH} \approx \sqrt{N}\Delta \tag{8.4}$$

this lorentzian width becomes greater than the single particle level spacing and thus the

spectrum become continuous. Most significnatly, for energies less than the lowest cutoff

$$E^{**} \approx \frac{\sqrt[4]{N}\Delta}{\log N} \tag{8.5}$$

a localization transition occurs, the sub-Golden Rule decay rate is predicted to vanish and the linewidth then shrinks to a δ-function.

We are interested in more than the linewidth of the quasiparticle states; we also want to know what properties including which wavefunction couplings of the quasiparticle spectrum are probed by the single-electron tunneling measurements. A very useful historical perspective is found in the neutron scattering experiments of nuclear physics [Bohr69; Burcham79]. In these experiments the spectrum of the many-body strongly interacting nucleus is probed by low energy neutron scattering. The measured resonances show fine structure with an energy scale 10^6 times smaller than the expected nuclear single particle level spacing. An additional envelope modulation of these resonance amplitudes occurs on the single particle energy scale. These results have been successfully interpreted within a "compound nucleus" model, in which the interaction of the incident neutron with the nucleus is described as an N-body wavefunction of the nucleus interacting with the single-particle wavefunction of the neutron for the duration of the neutron's passage through the nucleus. Gross structure due to resonant single particle tunneling is expected at the single particle energies of the mean field nuclear potential. Fine structure however is described by the interaction of the single particle with the many-body vibrational and rotational nuclear states (Figure 8.1A). The component of the incident single particle basis wavefunction in the exact many-body wavefunction determines the amplitude of that fine structure resonance. Strong interaction occurs between the single particle state and those exact many-body states closest in energy, weak interaction occurs for those many-body states further in energy. The measured transmission spectrum can thus be understood as an envelope function of broadened single-particle resonances with remarkable fine structure due to discrete many-body eigenstates.

We now return to the Altshuler et al quasiparticle spectrum for the finite Fermi system and consider the single-electron tunneling in a framework analagous to the compound nucleus picture. The mathematical description of a single-electron entering the N-electron QD is calculated by projecting a single particle state onto the basis of exact many-body eigenfunctions. At a given many-body eigenenergy E the ability of an electron to enter the QD is proportional to the overlap of the $N+1$ many-body wavefunction with a single

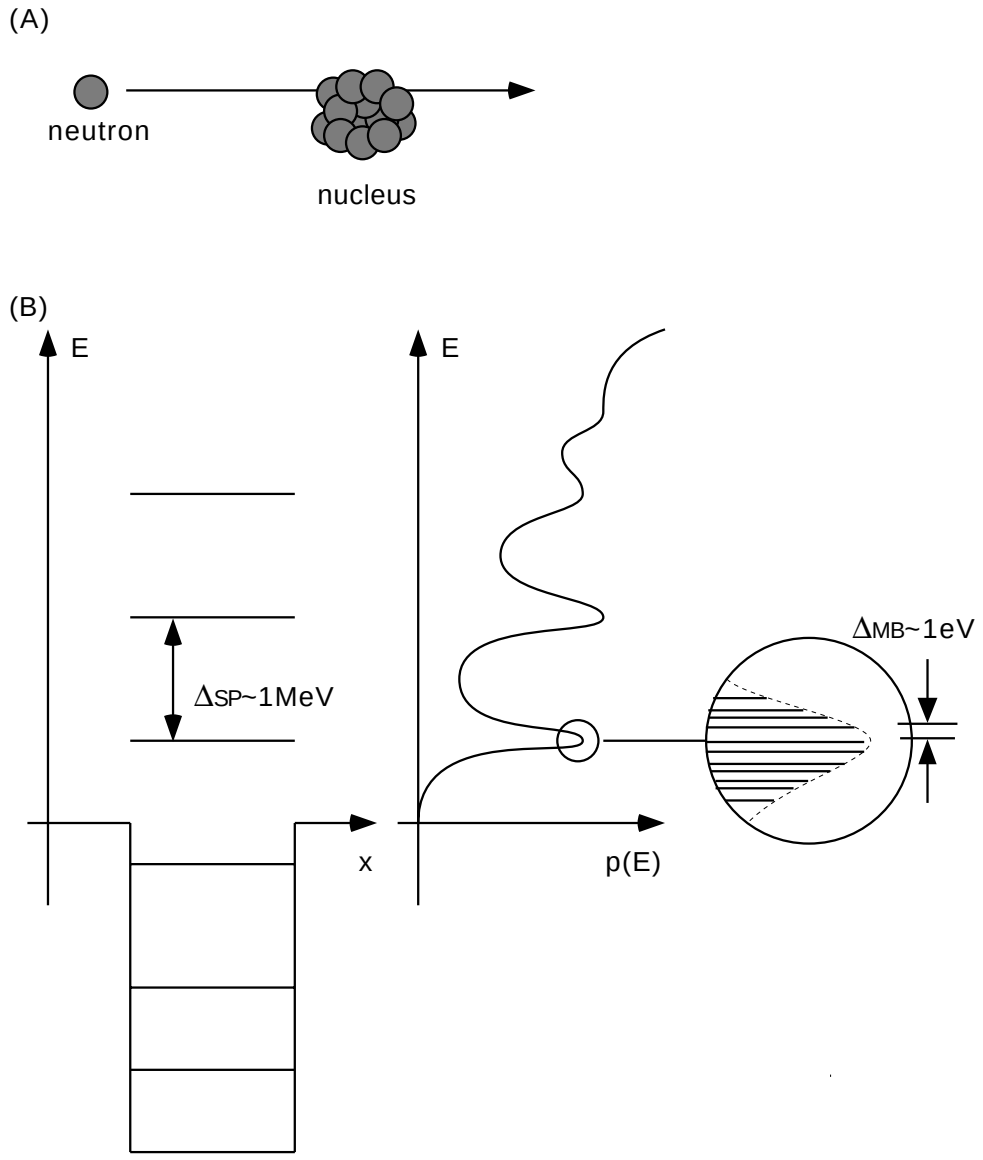

Figure 8.1: Nuclear neutron scattering resonances. (A) A neutron is injected through the nucleus with a low enough velocity to allow significant interaction. (B) The single particle spectrum expected of the deep nuclear potential is illustrated at left; the observed spectrum show modulation at these energies but also has much finer structure attributed to many-body nuclear states.

particle wavefunction representing the injected electron. Only a small fraction of all the many-body states are predicted to describe this effectively single-particle excitation, and those that do are clustered around the energy corresponding to the exact single-particle state. As in the compound nucleus result, expected tunneling resonances form a dense but discrete spectrum with a small many-body level spacing, amplitude modulated by a much larger envelope corresponding to the single-particle spacing. The width of each peak in the envelope function is determined by the quasiparticle linewidth regimes outlined in Eqn 8.2 to Eqn 8.5. At higher energies this envelope peak width broadens and the modulation of the tunneling current disappears. This is illustrated schematically in Figure 8.1B.

A significant difference between the nuclear neutron scattering and the QD electron tunneling is the excitation energy range accessed. Neutron scattering experiments probe very high excitation energies only, due to the very deep nuclear potential well. QD electron tunneling spectroscopy however probes the excitation spectrum starting at the very first excited state and working upwards. Further information on the character of the measured excitation resonances is provided at low energies. The resonances close to E_F correspond to many-body states that overlap with only one or a few single-particle states. These many-body states are therefore well described by a Slater determinant of exact single-particle states, as in the Hartree-Fock approximation (Eqn 2.9). This near-exact mapping of excited resonances to Hartree-Fock states is predicted valid for $\varepsilon < E^{**}$ [Altshuler97]. Above E^{**} the single particle states are well connected to a larger number of many particle states that are poorly approximated by the single Slater determinant of a Hartree-Fock state.

8.3.2 Connection to Experimental Results

The predictions of this extended Fermi liquid theory can now be compared to the experimental results of Chapters 5, 6 and 7. Chapters 5 and 6 showed strong agreement between the measured ground and excited spectra and the single-particle model of a fixed level spectrum successively filled by additional electrons. The main deviations from this picture were splitting of the electron spin degeneracy and decreasing level resolution for higher excited states. Section 7 confirmed that although the single particle description was accurate for the first one or two excited states, higher excited states fit this model less and less well.

Two major predictions have emerged from the Altshuler et al. modified Fermi liquid theory of Section 8.3.1 . The first is the high overlap between Hartree-Fock orbitals and the exact many-body excited resonances with energy $E < E^{**}$. Hartree-Fock is an approximate

treatment of the electron-electron interaction in which both the direct and exchange interaction terms are considered within a mean field approach (see Section 2.2.3). The spectrum of HF orbitals changes slowly with electron addition, simply because HF is a mean field solution and at our larger electron numbers $N = 50 - 200$ the fractional change in the average potential is small. HF yields a single-particle-like spectrum, only with eigenvalues and eigenfunctions that correspond to the screened mean field potential. Within HF, an added $N + 1$ electron should therefore fill the previous first excited state of the N electron system, except for a small change in eigenenergy and eigenfunction due to the resulting mean field change. For the case of complete relaxation between tunnel events, the excited state spectra consists of sharp single resonances separated on average by the bare single particle spacing. Note that the HF spectrum also includes possible spin splitting due to the exchange interaction term [Eto97a] and possible eigenenergy fluctuations due to the direct interaction [Agam97].

Comparison with experimental data strongly supports this Hartree-Fock interpretation of the lowest excited states. The lowest few measured excited states map in a 1:1 manner onto the measured ground states (see Figure 7.5). Mismatch between the mapped ground and excited can be corrected with a 2% change to the magnetic field scale per electron, in qualitative agreement with a slow $\sim 1/N$ change in the HF mean field per electron (see Figure 7.6). The spin splitting visible in both the assembled ground state spectra (Section 5.3) and the measured excitation spectra (Section 6.4) is expected in the HF spectrum due to the exchange interaction. Eigenenergy fluctuations as observed in the empirical ground/excited correlations (Section 7.2) are also expected in HF due to changing single-particle level occupancies [Agam97]. We further note that this 1:1 mapping expected within HF becomes less accurate for higher energy excited states, in agreement with the E^{**} cutoff energy and limited validity of the HF description for these excited states. For the QD of Figure 7.6 for which we estimated $N \sim 100$, $E^{**} \sim 2\Delta$ and the Altshuler et al theory predicts an accurate HF mapping only for the first two excited states, similar to the accuracy decay observed.

The second major prediction of the modified Fermi liquid description is the energy dependence of the tunneling resonance width. This resonance width is expected to increase at higher energy as more electron-electron relaxation paths become available, and in fact is predicted to increase quadratically for energies above E^* (Eqn 8.1 and Eqn 8.2). Figure 6.12 shows clearly that the excited level widths increase continuously above E_F, but this increase

appears linear in energy instead of quadratic. Again, for $N \sim 100$ we have a predicted transition at $E^* \sim 3\Delta$ to the quadratic Golden Rule behavior. The first five excited states were resolvable and included in the data of Figure 6.12. The highest 4th and 5th states should be at or above the E^* Golden Rule transition energy, but show no sign of a quadratic width increase. Neither does the first nor second state show a fixed width as predicted if a localization transition existed. The linear dependence of the resonance width is however a significant result that strongly supports the sub-Golden Rule decay theory [Altshuler97] and appears to contradict predicted Golden Rule behavior [Sivan94b;Mejia-Monasterio98].

8.3.3 Implications for other theoretical work

The data support a Hartree-Fock interpretation of the ground state spectrum and the lower excited state resonances. Higher excited states diverge from this simple behavior in qualitative agreement with the increasing electron-electron interaction influence outlined in the finite system Fermi liquid theory.

The experimental data supporting a Hartree-Fock treatment of the ground and low energy excited state spectrum has significant consequences. Both Hartree-Fock and density functional theory have been employed in calculations of QD properties, but rarely justified experimentally. Our experimental results offer significant and general support for the further use of both methods to explore and explain electron transport through larger disordered quantum dots. In particular, the results support the previous use of HF and DFT to explain non-relaxed tunneling resonances [Agam97], Coulomb blockade peak spacing fluctuations due to scarred wavefunctions [Stopa97] and QD spin polarization and spin splitting [Stopa97; Hirose98]. The results also indicate that electron-electron interaction significantly affects the measured tunneling spectrum and within this low energy range both the direct and exchange terms are necessary to get agreement between theory and experiment.

Section 8.3.2 has described how the level broadening data illustrates a sub-Golden Rule decay, but does not show evidence of a localization transition. These finite size system effects are a fascinating new manifestation of solid-state electron-electron interactions and have recently attracted a great deal of theoretical attention. Theoretical efforts have argued for and against the existance of the Fock space localization transition [Sivan94b; Altshuler97; Silvestro97; Mejia-Monasterio98]. The system ergodicity and character of the level statistics as a function of energy and interaction strength has also been extensively studied, with different

treatments suggesting different transition energies and transition interaction strengths between the ergodic system with Wigner-Dyson spacing statistics and the non-ergodic system with poissonian statistics [Berkovits96; Jacquod97; Berkovits98; Mirlin97; Pascaud98; Silvestro98]. This very active theoretical work continues, and suggests an exciting but difficult future experimental contribution may be characterization of excited state spacing statistics as a function of energy above the QD Fermi level.

8.3.4 Building the QD spectrum

Using this experimental support for the HF treatment of the spectrum, we return to our initial question of how to describe the fundamental features of the measured level spectrum. Here we outline a simple qualitative understanding of how the the quantum dot spectrum is constructed and how tunneling measurements access this spectrum. We begin with a single-particle spectrum and illustrate the basic modifications accounted for by a Hartree-Fock treatment, and then show how this results in the observed ground and excited state spectra. We ignore the effect of level broadening discussed above.

The quantum dot spectrum can perhaps be thought of as a construction arrived at through the following steps (Figure 8.2):

1. Start with a single particle spectrum for a symmetric system close in shape to the actual QD. This spectrum will show smooth dependences for the eigenfunctions on magnetic field B, with many true crossings between differently evolving wavefunctions.

2. The exchange interaction causes splitting of the originally spin degenerate eigenvalues. The splitting magnitude is dependent on the strength of the exchange interaction and the total spin polarization of the dot.

3. The perturbation of the potential into a non-symmetric shape and the addition of disorder causes anticrossings to appear between wavefunctions of the same spin only, at most or all same spin wavefunction crossing points.

4. This constructed Hartree-Fock spectrum changes slowly as each electron is added to the QD.

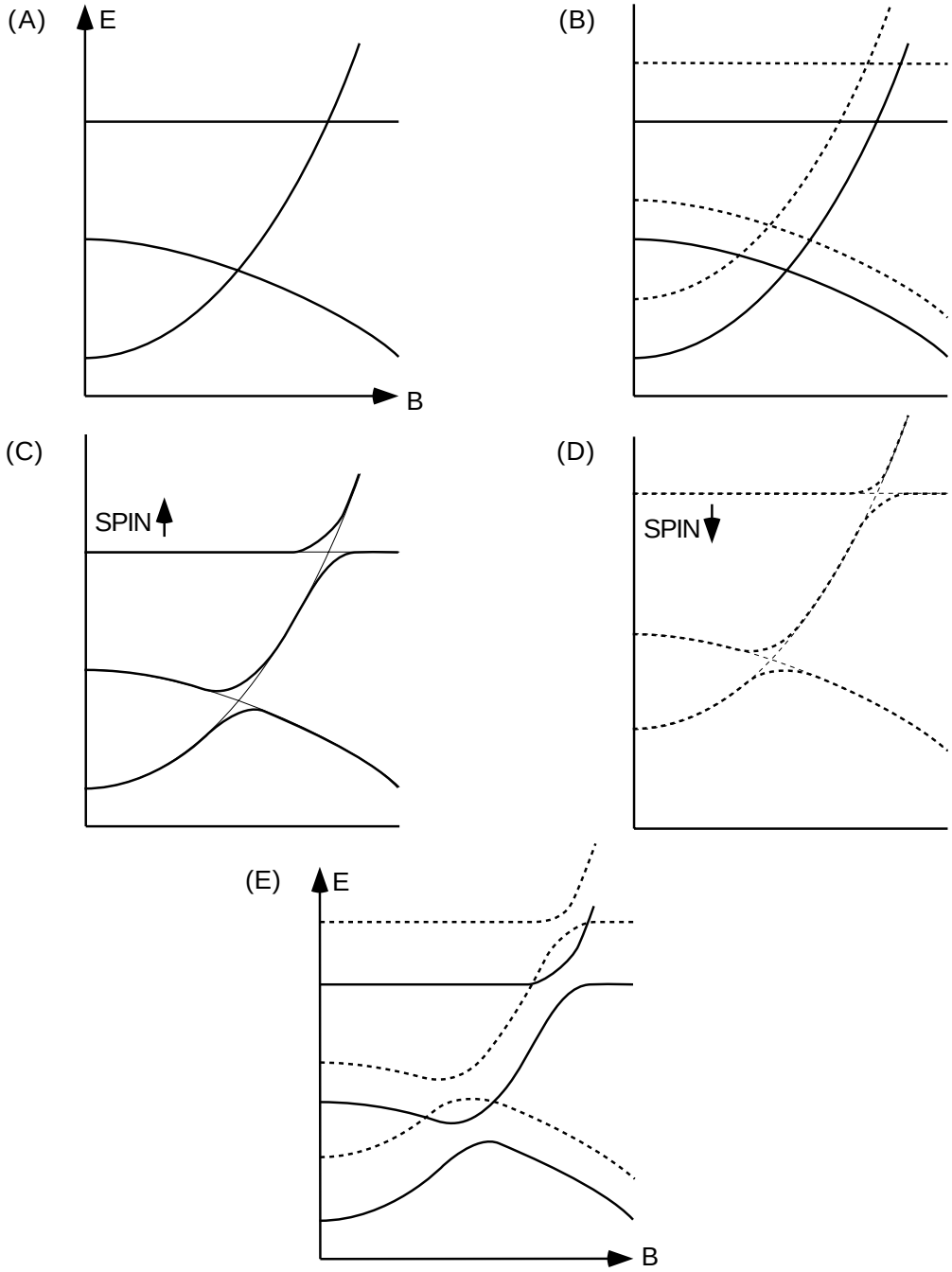

Figure 8.2: Building the QD spectrum. (A) The single-particle spectrum for a given spatially symmetric confining potential (B) Spin splitting of this spectrum due to the exchange interaction (C) The spin-up levels, with anticrossings added due to removal of the confining potential spatial symmetry (D) The spin-down levels with similar anti-crossings added (E) The re-assembled spectrum.

Measurement of the spectrum is via tunneling through the zero bias ground states or the finite bias excited states. The experimentally observed spectra can be derived from the composite spectrum of Figure 8.2E.

Ground States: For the ground state spectrum, the fixed N constraint and the direct coulomb term causes an expansion of the level spectrum with an average gap corresponding to the Coulomb charging energy inserted between each eigenfunction, now traced over all fields B at fixed N. (Figure 8.3B)

Excited States: For the excited state spectrum, approximately V_{DS}/Δ excited states are available for tunneling. If the device is tuned to emphasize the $N+1$ excited states in resonance with the source, then it is the V_{DS}/Δ states above the QD Fermi level that appear in the finite bias measurement (Figure 8.3C). Additionally, the HF states are increasingly broadened by the electron-electron interaction for energies above the $N+1$ electron QD Fermi level, however this broadening is not depicted.

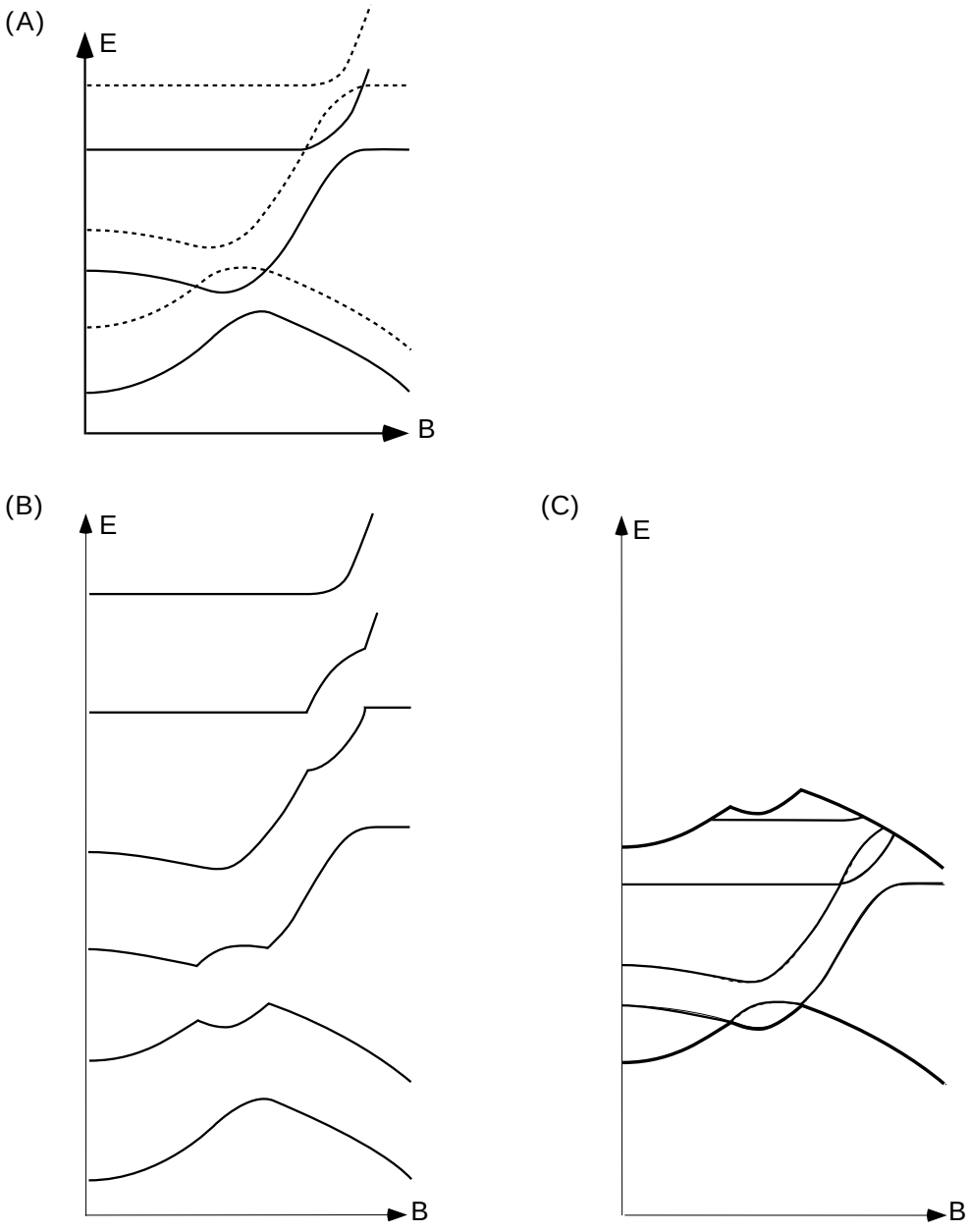

Figure 8.3: Measuring the QD spectrum. (A) The composite spectrum of Figure 8.2E (B) Ground state measurements at successive N introduce a capacitive charging energy spacing between each measured ground state trace. Note that same spin anti-crossings are smooth; opposite spin anti-crossings are sharp. (C) Excitation spectra measurements show a band limited at top and bottom by the ground state trace. All accessible states within the band appear as resonances without the capacitive charging spacing. In particular, opposite spin levels should show as real crossings instead of anti-crossings.

Chapter 9

Conclusions

We have attempted to investigate how many-body electron-electron interactions affect the ground and excited state level spectra of a generic, isolated, Fermionic system. This investigation has been pursued via a detailed experimental study of the ground and excited state spectra of disordered, multi-electron quantum dots for successive electron occupancy numbers $N, N+1 \ldots N+8$. Electron tunneling spectroscopy was used to sample the quantum dot density of states as a function of electron number N, perpendicular magnetic field B and source-drain bias V_{DS} [Stewart97].

The basic features of the measured quantum dot spectra are surprisingly consistent with a single-particle model in which a fixed spectrum of levels is filled one electron at a time. Deviations from this dominant single-particle behavior exist however, indicating that many-body effects are influencing the quantum dot spectrum.

Single-particle behavior includes:

- alignment of $N, N+1$ anticrossing features in the collapsed ground state spectra of Chapter 5.

- very strong correlation between successive $N, N+1$ excitation spectra except for the shift of one level, in Chapter 6.

- direct 1:1 mapping of assembled ground spectrum onto the measured excitation spectrum, in Chapter 7.

Many-body behavior includes:

- lifting of spin degeneracy in both the ground and excited spectra of Chapter 5 and Chapter 6.
- energy fluctuations in the assembled ground state spectrum when compared to the excitation spectra, Figure 7.1.
- decay in the 1:1 mapping accuracy for higher excited states, Figure 7.5.
- increase in the resonance width for higher excited states, Figure 6.12.
- gradually changing B field scale for magnetoconductance fluctuations as electrons are added to the QD, Figure 7.6.

We have tried to resolve the apparently contradictory result of simultaneous single-particle and many-body behavior by connecting the experimental data to recent theory describing quasiparticle decay in finite Fermionic systems. This theoretical work, outlined in Chapter 8, predicts that close to the Fermi energy of the QD, exact many-body wave-functions overlap almost completely with approximate Hartree-Fock orbitals. At higher energies this correspondence vanishes and the tunneling resonances are predicted to grow in width and lose their single-particle character.

We argue that much of the experimental data strongly supports this interpretation of single-particle and many-body effects in the measured QD spectra.

Other data requires further investigation however, including the quantitative evaluation of correlations between N and $N+1$ excitation spectra, the quantitative evaluation of ground spectrum to excited spectra mapping accuracy, the total spin polarization of the quantum dot and the dependence of the spectral correlations on the system size N and disorder. Theoretically the correlations between successive excitation spectra have not been addressed at all, the QD spin polarization has been approached only using density functional theory and the difficult issue of dependence on size N and disorder has not yet been attempted.

We hope that this work has contributed to a better understanding of many-body interaction effects in finite Fermionic systems, and will help stimulate future experimental and theoretical efforts in these areas.

Bibliography

[Agam et al 97]	Phys. Rev. Lett. 78 (10) 1956, (1997)
[Alhassid et al 95]	Phys. Rev. Lett. 76 (10) 1711 (1996)
[Alshuler et al 95]	in Mesoscopic Quantum Physics, A.A. Akkermans et al Eds. (Elsevier, Amsterdam 1995)
[Altshuler et al 97]	Phys. Rev. Lett. 78 (14) 2803, (1997).
[Ando et al 82]	Rev. Mod. Phys. 54, 437 (1982)
[Andrei, Ed. 97]	"Two-Dimensional Electron Systems," Kluwer Academic Publishers, The Netherlands (1997)
[Ashoori et al 94]	Surface Science 305, 558 (1994)
[Bastard et al 91]	in Solid State Physics, Ehrenreich et al Eds. (Academic Press Inc, San Diego, (1991)
[Beenakker 97]	Rev. Mod. Phys. 69, 731 (1997)
[Beenakker 91a]	Phys. Rev. B 44 (4) 1646, (1991)
[Beenakker et al 91b]	in Solid State Physics, Ehrenreich et al Eds. (Academic Press Inc, San Diego, (1991)
[Berkovits et al 98]	Phys. Rev. Lett. 80 (3) 568 (1998)
[Berkovits et al 97]	Phys. Rev. B 55 (8) 5297, (1997)
[Berkovits et al 96]	J. Phys.: Condens. Matter 8, 389 (1996)
[Blanter et al 97]	Phys. Rev. Lett. 78 (12) 2449 (1997)
[Bohr et al 69]	"Nuclear Structure," W.A. Benjamin Inc, New York (1969).

[Bransden et al 83] "Physics of atoms and molecules," Longman Scientific and Technical, England (1983)

[Bruus et al 95] Phys. Rev. Lett. 53 (15), 9968 (1995)

[Burcham 79] "Elements of nuclear physics," Longman Scientific, England (1979)

[Cobden et al 98] Phys. Rev. Lett. 81 (3), 681 (1998)

[Cohen et al 99] cond-mat/9902342

[Cronenwett et al 97] Phys. Rev. Lett. 79, 2312 (1997)

[Eto 97a] Jpn. J. Appl. Phys. 36 3924, (1997)

[Eto 97b] J. Phys. Soc. Jpn. 66 (8) 2244, (1997)

[Folk et al 96] Phys. Rev. Lett. 76 (10), 1699 (1996)

[Foxman et al 93a] Phys. Rev. B Rapid 47 (15), 10020 (1993)

[Foxman 93b] Ph.D. dissertation, Massachusetts Institute of Technology (1993).

[Grimes et al 79] Phys. Rev. Lett. 42 (12), 795 (1979)

[Gutzwiller 90] "Chaos in Classical and Quantum Mechanics," Springer-Verlag, New York, (1990).

[Hirose et al 98] cond-mat/9808193

[Hohenberg et al 64] Phys. Rev. 136, B864 (1964)

[Huibers 99] Ph.D. dissertation, Stanford University (1999)

[Huibers et al 98] Phys. Rev. Lett. 81, 1917 (1988)

[Jacquod et al 97] cond-mat/9706040

[Jalabert et al 92] Phys. Rev. Lett. 68 3468, (1992)

[Jauregui et al 96] Phys. Rev. B Rapid 53 (4) R1713, (1996)

[Johnson 95] J. Phys.: Condense. Matter 7, 965 (1995)

[Johnson et al 92] J. Phys.: Condens. Matter 4, L623 (1992)

[Johnson et al 92] Phys. Rev. Lett. 69 (10), 1592 (1992)

[Joubert Ed. 98] "Density functionals: theory and applications," Springer-Verlag New York, (1998).

[Klein et al 96] Phys. Rev. B Rapid 53 (8), R4221 (1996)

[Kohn et al 65] Phys. Rev. 140A, 1133 (1965)

[Koulakov et al 97]	Phys. Rev. B 55 (15) 9223, (1997)
[Koulakov et al 98]	Phys. Rev. B 57 (4) 2352, (1998)
[Kouwenhoven et al 97]	in Proceedings of the Advanced Study Institute on Mesoscopic Electron Transport, L.L. Sohn et al., Eds. (Kluwer, Dordrecht, Netherlands 1997)
[Kouwenhoven et al 97]	Science 278, 1788 (1997)
[Kulik et al 75]	Sov. Phys. JETP 41, 308 (1975)
[Kumar et al 90]	Phys. Rev. B 42 (8), 5166 (1990)
[Mahan 90]	"Many-Particle Physics," Plenum Press, New York (1990).
[Marcus et al 97]	Chaos, Solitons and Fractals 8, 1261 (1997)
[Maurer et al 98]	cond-mat/9810283
[McEuen et al 91]	Phys. Rev. Lett. 66 (14), 1926 (1991)
[McEuen et al 92]	Phys. Rev. B Rapid 45 (19), 11419 (1992)
[McEuen et al 93]	Physica B 189, 70 (1993)
[Mehta 91]	"Random Matrices," Academic Press, Boston (1991).
[Meirav et al 95]	Semicond. Sci. Technol. 10, 255 (1995)
[Mejia-Monasterio et al 98]	cond-mat/9811031
[Mirlin et al 97]	cond-mat/9702120
[Oaknin et al 94]	Phys. Rev. B 49 (8), 5718 (1994)
[Palacios et al 94]	Phys. Rev. B Rapid 50 (8), 5760 (1994)
[Pascaud et al 98]	Ann. Phys. 7, 406 (1998)
[Patel et al 98a]	Phys. Rev. Lett. 80 (20), 4522 (1998)
[Patel et al 98b]	Physical Review Letters 81 (26), 5900 (1998).
[Patel et al 97]	Superlatt. and Microstruct. 21, 43 (1997)
[Pfaff et al 94]	Z. Phys. B 96, 201 (1994)
[Pfannkuche et al 93a]	Phys. Rev. B 47 (4), 2244 (1993)
[Pfannkuche et al 93b]	Physica B 189, 6 (1993)
[Pfannkuche et al 95]	Phys. Rev. Lett. 74 (7), 1194 (1995)
[Pfeffer et al 95]	Phys. Rev. B Rapid 52 (20), R14332 (1995)
[Pines et al 89]	"The theory of quantum fluids," Addison-Wesley Inc USA, (1989).

[Ralph et al 95]	Phys. Rev. Lett. 74 (16), 3241 (1995)
[Ralph et al 96]	Physica B 218, 258 (1996)
[Ralph et al 97]	Phys. Rev. Lett. 78 (21), 4087 (1997)
[Schmidt et al 95]	Phys. Rev. B Rapid 51 (8), 5570 (1995)
[Schmidt et al 96]	Solid-State Electronics 40, 15 (1996)
[Silvestro 97]	Phys. Rev. Lett. 79 (20), 3994 (1997)
[Silvestro 98]	PRE 58 (5), 5629 (1998)
[Simmel et al 95]	Phys. Rev. E 51 (6) 5435, (1995)
[Sivan et al 94a]	Europhys. Lett. 25 (8), 605 (1994)
[Sivan et al 94b]	Europhys. Lett. 28 (2), 115 (1994)
[Sivan et al 96]	Phys. Rev. Lett. 77 (6), 1123 (1996)
[Steffens et al 97]	cond-mat/9711077
[Stewart et al 97]	Science 278, 1784 (1997)
[Stopa 93]	Phys. Rev. B 48 (24), 18340 (1993)
[Stopa 96]	Phys. Rev. B 54 (19), 13767 (1996)
[Stopa 97]	cond-mat/9709119
[Takami 92]	Phys. Rev. Lett. 68 (23) 3371, (1992)
[Tamura et al 97]	Phys. Rev. Lett. 79 (7), 1345 (1997)
[Tanaka et al 96]	Phys. Rev. B 53 (7), 3901 (1996)
[Tarucha et al 96]	Phys. Rev. Lett. 77 (17), 3613 (1996)
[Ulloa et al 94]	Superlatt. and Microstruct. 15 (3), 269 (1994)
[Vallejos et al 98]	cond-mat/9802124
[van der Vaart et al 93]	Physica B 189, 99 (1993)
[Weinmann et al 95]	Phys. Rev. Lett. 74 (6) 984, (1995)
[Weis et al 93]	Phys. Rev. Lett. 71 (24), 4019 (1993)
[Weis et al 94a]	Semicond. Sci. Technol. 9, 1890 (1994)
[Weis et al 94b]	Surface Science 305, 664 (1994)
[Wilkinson 89]	J. Phys. A: Math. Gen. 22, 2795 (1989)
[Zakrzewski et al 91]	Phys. Rev. Lett. 67 (20) 2749, (1991)

Appendix A

ac + dc circuit diagram

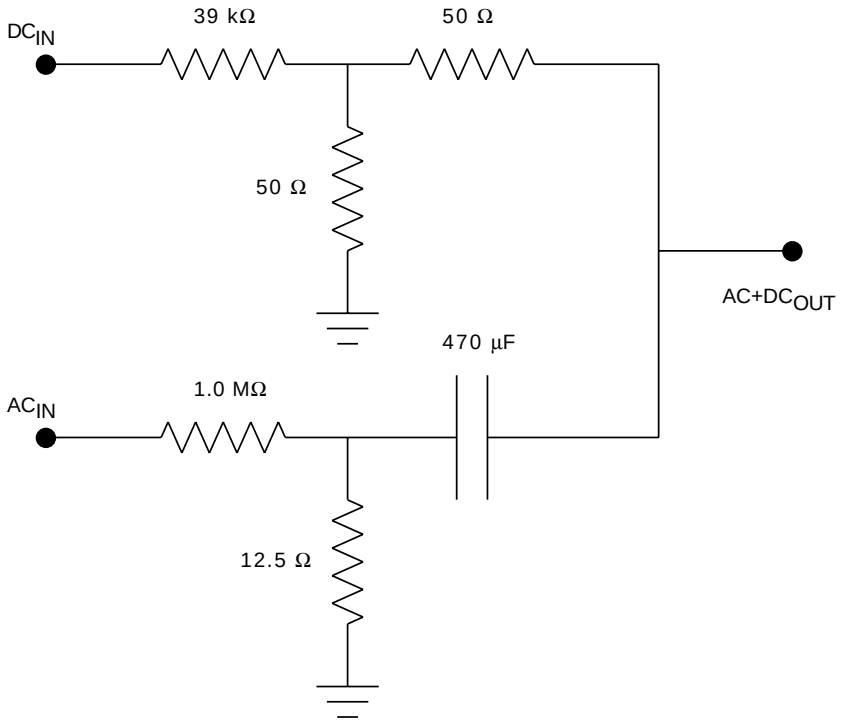

Figure A.1: The circuit constructed to *passively* add the small ac lock-in excitation signal to the large dc source-drain bias. Optimized for 13 Hz, at which frequency the dc voltage divider has a ratio 1000:1 and the ac divider has a ratio $10^5 : 1$.

Appendix B

Computer code for Coulomb diamond simulation

Included below is the programming code that was used to calculate the Coulomb diamond traces and plots of Figure 3.6. It is run using the IGOR Pro [©Wavemetrics Inc] software package.

```
#pragma rtGlobals=1 // Use modern global access method.

// Simulate Coulomb Blockade
// Originally written: David Sprinzak 03/97
// Modified: Duncan Stewart 04/98, 09/98, 02/99

// This program simulates Coulomb blockade with finite drain source voltage
// For given parameters (Vg,Vds,T etc.) the program calculates the current that
// goes through the quantum dot. The program calculates the probability per
// unit time for an electron to go into the dot (Nin) and the probability per
// unit time for an electron to go out from the dot(Nout). The current is calculated
// from these quantities by I=1/(1/Nout+1/Nin).
// The current is in arbitrary units.
// The differential conductance is calculated by subtracting the current at two adjacent
// values of the drain source voltage.
// Waves Elevel and MagGamma contain the information on eigenenergies
// and wavefunction couplings -- user can modify at leisure.
```

```
// Function GammaL(i)
// energy level DOS distribution for coupling to left reservoir
Function GammaL(i)
   variable i

   wave w=magGamma
   // assume square distribution
   return    w[i][0]

End

// Function GammaR(i)
// energy level DOS distribution for coupling to right reservoir
Function GammaR(i)
   variable i

   wave w=magGamma
   // assume square distribution
   return    w[i][1]

End

// Function fermi(E,T)
// fermi distribution at the leads
Function fermi(E,T)
   variable E, T

   return 1/(1+exp(E/T))

end


// Function CurrentIn(N,Vg,Vds,Elevel,Beta, T,GammaW,Ec,direction)
// Calculates Nin by integrating over DOS of the unoccupied energy levels in the dot
// and the available fermi distribution in the input lead
Function CurrentIn(N,Vg,Vds,Elevel,Beta, T,GammaW,Ec,direction)
   variable N, Vg, Vds, Beta, T, GammaW, Ec,direction
   wave Elevel

   variable EDiff=0
   variable Nmax=numpnts(Elevel)
```

```
   variable Nin=0
   variable i=Nmax

   do
      // Outer loop goes over all energy levels in the dot, from Nmax to highest occupied
      if (direction==0)
         // from left to right
         // first term below includes less transmission of lower levels through barrier
         EDiff = Elevel[i]-Vg-Beta*Vds+Vds+Ec
         Nin += ( GammaL(i)*(1+0.0*((abs(EDiff))^0.5*sign(Ediff))) )
                        * fermi((Elevel[i]-Vg-Beta*Vds+Vds+Ec),T)
      else
         // from right to left NB the right fermi level is zero ref and not shifted Vds
         EDiff = Elevel[i]-Vg-Beta*Vds+Ec
         Nin += ( GammaR(i)*(1+0.0*((abs(EDiff))^0.5*sign(Ediff))) )
                       * fermi((Elevel[i]-Vg-Beta*Vds+Ec),T)
      endif

      i -= 1
   while( i>=N )

   return Nin

End

// Function CurrentOut(N,Vg,Vds,Elevel,Beta, T,GammaW,Ec,direction)
// Calculates Nout by integrating over DOS of the occupied energy levels in the dot
// and the available empty fermi distribution in the output lead
Function CurrentOut(N,Vg,Vds,Elevel,Beta, T,GammaW,Ec,direction)
   variable N, Vg, Vds, Beta, T, GammaW, Ec,direction
   wave Elevel

   variable EDiff=0
   variable Nout=0
   variable i=0

   do
      // Outer loop goes over all energy levels in the dot, from 1 to highest occupied = N
      if (direction==0)
         // from left to right NB the right fermi level is zero ref and not shifted Vds
         // first term below is GammaR modified for height above rt barrier
```

```
         EDiff = Elevel[i]-Vg-Beta*Vds+Ec
         Nout += ( GammaR(i)*(1+0.1*((abs(EDiff))*sign(Ediff))) )
                         * ( 1-fermi((Elevel[i]-Vg-Beta*Vds+Ec),T) )
      else
         // from right to left
         EDiff = Elevel[i]-Vg-Beta*Vds+Vds+Ec
         Nout += ( GammaL(i)*(1+0.1*((abs(EDiff))*sign(Ediff))) )
                         * ( 1-fermi((Elevel[i]-Vg-Beta*Vds+Vds+Ec),T) )
      endif

      i += 1
   while( i<=N )

   return Nout

End

Macro CurrentQd(VdsMax,VdsPts,VgMin,VgMax,VgPts,suffix, newDisplay)
   variable VdsMax=200, VdsPts=41, VgMin=0, VgMax=300, VgPts=300
   string suffix
   variable newDisplay = 0

   Silent 1; PauseUpdate

   variable delta = 20
   variable T = 1
   variable Ec = 250
   variable Beta = 0.3

   variable N=15,GammaWr=1,GammaWl=1
   variable VdsShift = (2*VdsMax)/(1e6*VdsPts)
   variable time1=ticks, time2

   string dcCurrent = "dcI_VgVds"+suffix
   string dcCurrentshiftedp = "dcI_VgVdsp"+suffix
   string dcCurrentshiftedm = "dcI_VgVdsm"+suffix
   string conductance ="g_VgVds"+suffix

   Make/N=30/D/O Elevel
   SetScale/P x 1,1,"", Elevel
   Elevel = -Ec/2+(x-N)*delta
```

```
   Duplicate/O Elevel magGamma
   magGamma=1

   Make/N=(VgPts,VdsPts)/D/O $dcCurrent,$dcCurrentshiftedp,$dcCurrentshiftedm,$conductance
   SetScale/I x VgMin,VgMax,"", $dcCurrent,$dcCurrentshiftedp,$dcCurrentshiftedm,$conductance
   SetScale/I y -Vdsmax,Vdsmax,"", $dcCurrent, $conductance
   SetScale/I y (-Vdsmax+VdsShift),(Vdsmax+VdsShift),"", $dcCurrentshiftedp
   SetScale/I y (-Vdsmax-VdsShift),(Vdsmax-VdsShift),"", $dcCurrentshiftedm

   $dcCurrent =1/(1/CurrentOut(N,x,y,Elevel,Beta, T,GammaWr,Ec,1)
                  +1/CurrentIn(N,x,y,Elevel,Beta, T,GammaWl,Ec,1)  )
                     - 1/(1/CurrentOut(N,x,y,Elevel,Beta, T,GammaWr,Ec,0)
                  +1/CurrentIn(N,x,y,Elevel,Beta, T,GammaWl,Ec,0))
   $dcCurrentshiftedp =1/(1/CurrentOut(N,x,y,Elevel,Beta, T,GammaWr,Ec,1)
                   +1/CurrentIn(N,x,y,Elevel,Beta, T,GammaWl,Ec,1))
                      - 1/(1/CurrentOut(N,x,y,Elevel,Beta, T,GammaWr,Ec,0)
                   +1/CurrentIn(N,x,y,Elevel,Beta, T,GammaWl,Ec,0))
// $dcCurrentshiftedm =1/(1/CurrentOut(N,x,y,Elevel,Beta, T,GammaWr,Ec,1)
                   +1/CurrentIn(N,x,y,Elevel,Beta, T,GammaWl,Ec,1))
                      - 1/(1/CurrentOut(N,x,y,Elevel,Beta, T,GammaWr,Ec,0)
                   +1/CurrentIn(N,x,y,Elevel,Beta, T,GammaWl,Ec,0))

   $conductance[][] =$dcCurrentshiftedp [p][q] - $dcCurrent [p][q]
   $conductance[][] /= (2*VdsShift)

   if( newDisplay == 1 )
      Display;AppendImage $dcCurrent
       Label bottom "Vg (arb. units)";Label left "Vds (arb. units)"

      Display;AppendImage $conductance
      Label bottom "Vg (arb. units)";Label left "Vds (arb. units)"
   endif

   KillWaves $dcCurrentshifted
   time2 = ticks
   print "Calculation time (mins) ",(time2-time1)/(60.15*60)

end
```

Appendix C

Experimental tricks

C.1 Sample switching noise

A dramatic reduction of the typical high and low frequency switching noise was essential to the success of the measurements reported here. Five variables appeared to have an impact on this device switching noise.

1. **2DEG heterostructure** The observed noise behavior was unquestionably a strong function of the 2DEG heterostructure processed. No trend in heterostructure design was discovered that correlated with low noise except for 2DEG depth – deeper 2DEGs usually had lower switching noise.

2. **Slow cool** A slow, approximately linear cooling process from 300K to 4K over $\sim$ 24 hrs appeared to reduce the noise present in a given sample. This variable was poorly tested due to the time commitment required to test it rigorously, however on at least two occasions the same device showed more low frequency noise after a rapid cool.

3. **Positive gate bias during cool** Again, this variable has been tested poorly. However, during portions of this work the same device was cooled and tested with zero positive bias, +0.4V positive bias, +0.6V positive bias and +0.4V positive bias. Both 0.4V cools showed the lowest noise. The 0.6V cool showed higher noise although this may have been due to electrostatic discharge that occurred on that particular cool. The zero bias cools routinely showed higher noise.

4. **Cold time** High frequency noise ($>$ 1 Hz) in good devices disappeared within 2-3

days of reaching 50mK. Low frequency noise disappeared more gradually, typically over the first 1-2 weeks of the <1K run. If high frequency noise persisted longer than 4 days it rarely disappeared during that run, and if too high in amplitude the device was usually pulled.

5. **Gate activity** For good working devices with acceptable high and low frequency noise, adjustment of gate voltages typically induced low frequency noise. Much of the data in this work was taken with the minimum sweep ranges and gate adjustments possible, in order to reduce low frequency noise. Gate voltages were not swept to zero after each sweep, but rather left at their endpoints. Gate voltages were always swept rather than set to their new start points.

C.2 Optimization of Coulomb diamond resonances

High quality excited state data required careful optimization of the device configuration. The direction of current flow, the source-drain voltages used, and the symmetry or asymmetry in QPC resistances dramatically affected resolution of the excited states. More detailed discussion of these effects is provided in Section 3.5. In particular, Figure 3.6, Figure 3.7, Figure 3.8 and the discussion of p. 35-37 should be understood in detail. In what follows we present a short checklist to guide experimental optimization of the excited state resonances resolution.

1. The probable goal is to maximize resolution of the unoccupied state resonances at the expense of the occupied state resonances (Figure 3.7). Choose to focus on either the unoccupied resonances with the source or drain based on whichever side of zero bias the Coulomb diamond edge is *less* vertical. Conductance is effectively a vertical derivative of the dc current diamond; choose the diamond edge that yields a large derivative by being more perpendicular to the vertical line of differentiation.

2. Fix the source-drain bias at a value that is large enough to include $\sim 10\ \Delta$. This will typically be $\sim E_C/2$.

3. Now optimize the asymmetry of the QPCs. Measure *both* the dc current and the ac conductance of the broadened CB peak. The goal is to generate a series of traces similar to Figure 3.8 and Figure 4.7. The middle traces should be for well balanced,

or symmetric QPCs. If active wall control is being used the symmetric QPC values should lie directly on the diagonal line linking to two chosen QPC voltage pairs. Deviate to both sides of the diagonal by opening QPC1 1% and closing QPC2 1%, then opening QPC1 2% and closing QPC2 2% etc.... Continue until the dc current assumes a triangular shape and the ac conductance is dominated by a sharp peak at one side. Then repeat for the opposite condition, closing QPC1 and opening QPC2.

4. Assemble the traces as in Figure 4.7 and choose the QPC asymmetry that yields the highest resolution of the unoccupied states resonances.

C.3 Evaluation of RF noise in source and drain leads

Another very useful measurement of the Coulomb diamond near zero bias yields an easy and excellent quantitative measure of RF noise in the source and drain leads. Plot the dc current in a 2D Coulomb diamond scan centered on zero bias, and zoomed in to encompass a source-drain voltage scale of only + 5mV to -5mV or less. At $V_{DS} = 0$ there should be no dc current, *but there will be*. This dc current is just rectification of the RF oscillation of the source or drain leads by the asymmetric diamond angle $\beta \neq 63^o$. The amount of dc current provides a quantitative measure of this noise. This useful and simple procedure is described in detail in [Huibers99].